

THERMAL COUPLING AND LENSING IN ARRAYS OF
VERTICAL CAVITY SURFACE EMITTING LASERS

Kathryn J. Greenberg

Submitted to the faculty of Mount Holyoke College
in partial fulfillment of the requirements for the degree of
Bachelor of Arts with Honor

Janice Hudgings, Mount Holyoke College
Thesis Advisor

May 4, 2009

ABSTRACT

The operating temperature of optoelectronic devices is the factor that most limits their performance and efficiency. In this thesis, we present research that focuses on investigating thermal behavior of operating vertical cavity surface emitting lasers (VCSELs) and VCSEL arrays. A variety of thermal effects are known to influence the performance of VCSELs and therefore, the goal of this research is to better understand how temperature affects the operation of these devices.

Previously, a variety of techniques have been used to measure the temperature of VCSELs. These techniques tend to be bulk measurements that lack sufficient spatial and thermal resolution, cannot be used on light emitting surfaces, and/or are not able to simultaneously measure the temperature at very different length scales across a VCSEL or VCSEL array. Instead, we use thermoreflectance microscopy to obtain two dimensional, high spatial (250nm) and temperature (10 mK) resolution images of the surface temperature of VCSELs.

The first part of this research focuses on comparing the surface temperatures of three different types of single VCSELs. We find that the surface temperature of the smaller aperture oxide confined single mode VCSEL is greater than that for the other two multi-mode VCSELs investigated. To validate our thermoreflectance microscopy technique, we compare our thermoreflectance results, in the case of the oxide confined single mode VCSEL, to those obtained

by the standard techniques of monitoring a shift in the lasing wavelength and emitted electroluminescence wavelength.

The second part of the research presented in this thesis investigates the thermal coupling between neighboring lasers in closely packed VCSEL arrays. Using thermoreflectance microscopy, we are able to not only measure the thermal coupling between neighboring lasers but also to simultaneously image thermal lensing in the lasing VCSEL and thermal gradients across adjacent laser apertures. In addition, these thermal coupling results are compared to those measured using the lasing wavelength shift technique. From these measurements, we calculate the radial thermal conductivity of the VCSEL array and attribute the variations in measured temperatures from the two techniques to an impedance between the surface and cavity of the VCSEL. Finally, time resolved temperature measurements are performed to determine the thermal diffusivity for the VCSEL array; this measurement is contrasted with prior results for bulk and thin-film materials.

Overall, this research provides a better understanding of the temperature distribution in VCSELs using thermoreflectance microscopy. In the case of single VCSELs, we find that the smaller aperture VCSEL leads to a greater change in temperature with operating power. In addition, we determine that the average cavity temperature of a VCSEL is higher than both the top mirror temperature and the surface temperature. Lastly in VCSEL arrays, we observe significant thermal coupling between VCSELs in the array, determine a thermal conductivity of 0.41 W/(cm K), and measure a thermal diffusivity of $1.47 \times 10^{-5} \text{ m}^2\text{s}^{-1}$.

ACKNOWLEDGEMENTS

Firstly, I would like to thank my advisor Professor Janice Hudgings for giving me this amazing opportunity to work in her research lab since my first year at Mount Holyoke College. Without her support, guidance, and encouragement throughout the past four years none of this research would have been possible. I arrived at Mount Holyoke hoping to get involved in research but could have only dreamed to be working on such a fascinating project. Now looking back, I really can not thank Janice enough. I have learned an incredible amount working in the lab, and I know that my undergraduate education would have been incomplete without the opportunities that she gave me.

I would also like to thank Joe Summers for the incredible amount of time that he spent helping me in the laboratory. I really appreciate everything that he has done for me and would not have learned nearly as much in the past two years if it wasn't for him. His comments and willingness to answer my questions throughout every step of my project were extremely valuable. In addition, I would like to thank Maryam Farzaneh for all of the time that she spent helping me in the laboratory when I first began this project. Without her supervision, I would not have gotten nearly as far as I did on my project during my first couple of years in the lab.

The acknowledgement would not be complete without thanking some of the other people that made this work possible. Thank you to Len McEachern and Thomas Liimatainen for all of their help with the construction of my setups,

assistance when problems with the computers arose, and willingness to lend a hand in whatever way that they could. Thank you as well to all of my co-lab members, both past and present (Liz, Hexuan, Sweta, and Susu), for their encouragement throughout my research experience and all of the amazing times that we had in the lab. I would like to give my sincere appreciation to my committee members, Professor Tav Hawkins and Professor Margaret Robinson, whose willingness to be a part of my senior thesis really means a lot to me.

Lastly, I would like to thank my family (Mom, Dad, and Jack) for their never ending love, support, and encouragement to follow my dreams throughout my life. Without them none of this would have been possible, and I therefore would like to dedicate this thesis to them.

TABLE OF CONTENTS:

1. INTRODUCTION.....	11
1.1 Overview	11
1.2 Prior Work on VCSEL Thermal Performance	12
1.3 Prior Work on VCSEL Array Thermal Performance.....	14
1.4 Techniques for Measuring Temperature in VCSELS.....	16
1.5 Overview of My Work.....	19
2. VCSEL FUNDAMENTALS.....	20
2.1 Basic Semiconductor Laser Structure	20
2.1.1 Fabry Perot Cavity.....	20
2.1.2 Gain in a Semiconductor Laser	24
2.2 Vertical Cavity Surface Emitting Lasers (VCSELS).....	33
2.2.1 Overview of VCSEL Structure.....	33
2.2.2 Lasing Frequency/ Longitudinal Modes.....	38
2.2.3 Transverse Modes.....	40
2.2.4 Distributed Bragg Reflector Mirrors	43
2.2.5 Gain Medium.....	49
2.2.6 Standard Operating Characteristics of VCSELS.....	50
3. EXPERIMENTAL METHODS	56
3.1 Introduction	56
3.2 Wavelength Shift Technique.....	56
3.2.1 Single VCSELS.....	57
3.2.2 VCSEL Arrays.....	58
3.3 Thermoreflectance Microscopy.....	60
3.4 Thermoreflectance Calibration Coefficient.....	66

3.4.1	Single VCSELs.....	67
3.4.2	VCSEL Arrays.....	70
4.	RESULTS: HIGH RESOLUTION THERMAL IMAGING OF A SINGLE VCSEL.....	74
4.1	Introduction.....	74
4.2	VCSEL Characteristics.....	75
4.3	Wavelength Shift Measurement: Lasing Wavelength Shift.....	77
4.3.1	Wavelength Shift with Temperature.....	77
4.3.2	Wavelength Shift with Current.....	79
4.3.3	Temperature versus Current.....	81
4.4	Wavelength Shift Measurement: Emitted Electroluminescence.....	83
4.5	Thermoreflectance Microscopy.....	87
5.	RESULTS: VCSEL ARRAY.....	95
5.1	Introduction.....	95
5.2	VCSEL Array Characteristics.....	97
5.3	Temperature Distribution Across Individual VCSEL Apertures.....	99
5.4	Thermal Coupling.....	104
5.4.1	Thermoreflectance Microscopy.....	104
5.4.2	Wavelength Shift and Thermoreflectance Microscopy Comparison.....	106
5.4.3	Thermal Impedance and Lateral Thermal Conductivity.....	108
5.5	Thermal Diffusivity.....	111
6.	CONCLUSIONS.....	120
	REFERENCES.....	124

TABLE OF FIGURES:

Figure 2.1.1: Standing waves in a Fabry Perot cavity.....	21
Figure 2.1.2: Output power versus frequency in VCSELs (R =100%).....	23
Figure 2.1.3: Output power versus frequency in VCSELs (R<100%)	24
Figure 2.1.4: Energy level diagram for (a) single atom (b) crystals.....	25
Figure 2.1.5: Energy level diagram.....	26
Figure 2.1.6: Energy level diagram for (a) conductors (b) insulators (c) semiconductors.....	28
Figure 2.1.7: Spontaneous emission.....	29
Figure 2.1.8: Stimulated emission.....	29
Figure 2.1.9: Stimulated absorption.....	30
Figure 2.1.10: Gain spectrum for a laser.....	31
Figure 2.1.11: Electron and hole distribution in gain medium.....	32
Figure 2.1.12: Electron hole recombination in gain medium.....	33
Figure 2.2.1: Typical VCSEL structure.....	34
Figure 2.2.2: Overlay of longitudinal mode frequencies and gain spectrum.....	39
Figure 2.2.3: Lasing spectrum of a single mode oxide confined VCSEL.....	40
Figure 2.2.4: Standing waves in laser cavity resulting in transverse modes.....	41
Figure 2.2.5: (a) Hermite Gaussian functions (b) Output beam shapes.....	42
Figure 2.2.6: Lasing spectrum of VCSEL with multiple transverse modes.....	43
Figure 2.2.7: Phase shift resulting from a wave incident on a mirror when (a) $n_1 > n_2$ ($\varphi = 0$) (b) $n_1 < n_2$ ($\varphi = \pi$).....	45
Figure 2.2.8: DBR mirror with reflection at each interface.....	46
Figure 2.2.9: Example reflectivity spectrum for DBR mirrors in a VCSEL.....	48
Figure 2.2.10: Quantum well and energy band structure in active region.....	49
Figure 2.2.11: LI and IV curve for a VCSEL.....	51
Figure 2.2.12: Lasing spectrum for VCSEL biased above threshold.....	52
Figure 2.2.13: Lasing spectra for single mode oxide confined VCSEL.....	53
Figure 2.2.14: Lasing spectra for multimode oxide confined VCSEL.....	54
Figure 3.2.1: Single VCSEL wavelength shift experimental setup.....	57

Figure 3.2.2: VCSEL array wavelength shift experimental setup.....	59
Figure 3.3.1: Thermoreflectance experimental setup.....	62
Figure 3.3.2: Reflectivity vs. time for one pixel of VCSEL thermoreflectance image.....	64
Figure 3.3.3: Four images calculated by integrating under reflectivity curve.....	65
Figure 3.4.1: (a) Thermoreflectance calibration coefficient experimental setup (b) Placement of thermocouple on VCSEL surface.....	67
Figure 3.4.2: (a) $\Delta R/R$ thermoreflectance image (b) Change in temperature (ΔT) measured using micro-thermocouple.....	69
Figure 3.4.3: Image of VCSEL array.....	70
Figure 3.4.4: Image of VCSEL array showing where ΔT and $\Delta R/R$ calculated..	71
Figure 4.2.1: LI and IV curves for (a) oxide confined single mode VCSEL (b) oxide confined multi-mode VCSEL and (c) proton implanted multi-mode VCSEL.....	77
Figure 4.3.1: Lasing wavelength vs. temperature for three types of VCSELs.....	78
Figure 4.3.2: Shift in oxide confined SM VCSEL lasing spectrum with increasing current.....	80
Figure 4.3.3: Lasing wavelength vs. current for three types of VCSELs.....	81
Figure 4.3.4: Change in temperature vs. change in dissipated power measured using shift in lasing wavelength for three types of VCSELs.....	82
Figure 4.4.1: Schematic of top mirror reflectivity spectrum.....	84
Figure 4.4.2: Change in temperature versus change in dissipated power using emitted electroluminescence wavelength shift technique.....	85
Figure 4.4.3: Comparison of lasing wavelength shift and emitted electroluminescence wavelength shift temperature measurement techniques.....	86
Figure 4.5.1: Thermoreflectance images for oxide confined SM VCSEL.....	88
Figure 4.5.2: Thermoreflectance images for oxide confined MM VCSEL.....	89
Figure 4.5.3: Thermoreflectance images for proton implanted MM VCSEL.....	90
Figure 4.5.4: ΔT vs. ΔP for the three types of VCSELs measured using lasing wavelength shift.....	91
Figure 4.5.5: ΔT vs. ΔP in oxide confined SM VCSEL using three types of	

temperature measurement techniques.....	93
Figure 5.2.1: Picture of 1D Sandia VCSEL array.....	97
Figure 5.2.2: Emission spectra for a VCSEL in the Sandia array.....	98
Figure 5.2.3: LI and IV curves for a typical VCSEL in the array.....	99
Figure 5.3.1: DC and thermoreflectance image of $\Delta R/R$ for VCSEL array.....	100
Figure 5.3.2: Temperature profile across cross section of VCSEL apertures.....	101
Figure 5.3.3: Thermoreflectance images of a single VCSEL in array at various changes in electrical powers.....	102
Figure 5.3.4: Curvature in thermal profiles with increasing change in electrical bias powers measured using thermoreflectance.....	103
Figure 5.3.5: Comparison of beam shape and thermoreflectance image for single VCSEL in the array.....	104
Figure 5.4.1: Temperature profile across cross section of VCSEL apertures.....	105
Figure 5.4.2: Thermal coupling in VCSEL array measured using wavelength shift and thermoreflectance microscopy techniques.....	107
Figure 5.4.3: Radial heat spreading from modulated VCSEL.....	108
Figure 5.4.4: Thermal impedance vs. VCSEL spacing for VCSEL array.....	110
Figure 5.5.1: Experimental setup for time gated experiment.....	112
Figure 5.5.2: Schematic of how the time gated experiment works.....	113
Figure 5.5.3: (a) Current vs. time for modulated VCSEL (b) lasing spectra corresponding to the pulses in (a).....	114
Figure 5.5.4: Wavelength shift vs. phase of the pulse for modulated VCSEL.....	115
Figure 5.5.5: Phase shift between change of wavelength for modulated VCSEL and neighboring VCSEL.....	116
Figure 5.5.6: Plot of phase shift at a range of frequencies.....	118

1. INTRODUCTION

1.1 Overview

Vertical cavity surface emitting lasers (VCSELs) are semiconductor devices that over the past few decades have become widely used commercially. Applications of VCSELs include Gigabit Ethernet and optical interconnects, as well as implementation into everyday consumer devices such as optical mice for computers [1,2]. VCSEL arrays, in which multiple VCSELs are operated side-by-side on a single chip, are also used for a variety of applications such as high speed parallel data transmission and optical pumps for other types of lasers [3,4].

One of the distinguishing characteristics of VCSELs that separate them from other types of lasers is the orientation of the cavity and output beam of the laser. The specific structure of VCSELs will be discussed in more detail in Chapter 2. In traditional edge emitting lasers, light is emitted from the side of a cleaved semiconductor wafer and has a high beam divergence. In VCSELs, however, the light is emitted from either the top or bottom surface of the wafer. The vertical design of VCSELs allows for the testing of lasers to be done immediately following fabrication and before the dicing and packaging stages of production. The ease of mass production and on-chip testing of VCSELs makes them an inexpensive option for many applications. Some of the other advantages of VCSELs are their circularly symmetric beam shape, low beam divergence, and single longitudinal mode output beam [5]. Circular beam shape and low beam

divergence allow for easier coupling of the laser light into optical fiber, which is necessary for many applications in today's society.

While there are numerous advantages of VCSELs, several types of thermal effects limit the performance and lifetime of these lasers. Excessive heating limits output powers to typically 1-2mW and can result in unstable polarization and variations in the threshold current. Temperature variations across the surface of the laser can lead to thermal lensing and self-focusing, which can change the output beam shape [5,6]. In addition, coupling of thermal effects with optical and electrical behaviors can cause gain suppression and transverse mode hopping [7-9].

1.2 Prior Work on VCSEL Thermal Performance

Over the past few decades, a significant amount of research has been done to design and fabricate efficient VCSELs for network and communications systems, with improved thermal management for higher operating efficiencies and output powers. Improved designs of VCSELs come from the understanding of various factors that affect the operation of the laser. One important factor, the spatial temperature variation across the cavity and aperture of the device, leads to a number of thermal effects mentioned above, including thermal lensing and self-focusing.

Previously, several research groups have studied the effect of temperature on several VCSEL operation characteristics, in hopes of improving the thermal

properties of these devices. One group in particular, M. Osinski and W. Nakwaski at the University of New Mexico, conducted numerous wavelength shift experiments investigating how temperature affects the lasing properties of VCSELs, including the longitudinal mode spectra, transverse mode structure, threshold current, and output power of the laser. It was observed that temperature has a large effect on some of the operating characteristics, including a significant shift in the lasing wavelength ($\sim 12\text{nm}$), variations in the threshold current of several milliamps ($\sim 7\text{mA}$), and a decreased output power of a few milli-watts ($\sim 7\text{mW}$) for a 250K change in temperature of the VCSEL. In addition, using an analytical model, they found that active-region heating results in a non-uniform temperature distribution, known as thermal lensing [10].

Up until this point, several research groups had predicted a temperature distribution laterally across an operating laser but did not have a technique with high enough resolution to measure it. M. Dabbicco et al, however used one of the first non-contact techniques, shift in the emitted electroluminescence spectrum, to experimentally measure a significant temperature distribution across the top mirror of a laser [5]. This temperature variation, as noted before, leads to thermal lensing in the laser. While a shift in the electroluminescence spectrum can be used to measure the temperature distribution across the aperture of a VCSEL, it provides very low resolution.

More recently, a previous thesis student in Professor Janice Hudgings' laboratory used a high resolution surface measurement technique, thermorefectance microscopy, to study laser phenomena such as thermal lensing

in two different types of VCSELs, oxide confined and proton implanted. Using the data collected from thermoreflectance microscopy, the focal length of the thermal lens was calculated for various bias currents to the laser [11]. From this research a more detailed understanding of the temperature distribution across the surface of a VCSEL was obtained, as well as better insight into thermal effects, especially thermal lensing, present in vertical cavity surface emitting lasers.

1.3 Prior Work on VCSEL Array Thermal Performance

Furthermore, individual VCSELs have been arranged in two dimensional arrays [4]. In the case of these VCSEL arrays, it is not only important to understand the thermal effects in the individual lasers but also how the heat from one laser can impact the operating conditions of nearby VCSELs. This thermal crosstalk between lasers in the array is important because the heat generated by one VCSEL in the array can affect the lasing wavelength and output power of numerous other neighboring VCSELs in the array. The VCSEL array work presented in Chapter 5 focuses on using two temperature techniques, lasing wavelength shift and thermoreflectance microscopy, to investigate the thermal coupling between individual lasers in the array. In addition, various material parameters of the array including thermal diffusivity and thermal impedance have been experimentally determined.

Previously, much research has been done to try to understand the effect of thermal coupling in VCSEL arrays. Specifically, several research groups have

looked at the effect that spacing of individual VCSELs in the array has on thermal coupling. One group in particular, T. Wipiejewski et al., measured the thermal crosstalk between densely spaced 4 x 4 VCSEL arrays [12]. Using the wavelength shift technique to measure the thermal coupling, they found that the temperature of one VCSEL would increase by 1.5K with power dissipation of an adjacent VCSEL equal to 10mW. Thermal coupling between further away VCSELs in the array was also reported. In addition, both transverse and lateral values for the thermal conductivity of the array were experimentally determined and used to calculate the effective thermal resistance of the device. They found that the thermal resistance of VCSELs in the 2D array was approximately 50% greater than that of single VCSELs, leading to an increase in the temperature of the array [12].

In addition, Y. Uchiyama et al. investigated the thermal coupling between individual VCSELs spaced as closely as 20 μ m [13]. Similar to previous research, they measured the shift in the lasing wavelength due to heating of a 110 element VCSEL array and found significant thermal coupling between several neighboring VCSELs. This research concluded that thermal coupling is a significant problem in VCSEL arrays and that careful design is needed to limit the severity of these thermal effects [13].

1.4 Techniques for Measuring Temperature in VCSELs

Measuring the temperature distribution in semiconductor lasers is challenging due to the small dimensions (μm - mm) of these devices. Hence, a variety of techniques have been developed to address this challenge. Traditionally, the change in temperature is determined from the resulting shift in the lasing wavelength due to the change in the refractive index with temperature. However, because wavelength shift measures the average cavity temperature [6], it provides a single data point per VCSEL, and does not pick up spatial variation in the temperature profile across the VCSEL surface.

Alternatively, one can measure the shift in the emission wavelength of the electroluminescence. Unlike the lasing wavelength shift technique, the emitted electroluminescence peak provides the temperature of the top mirror in the VCSEL structure [6]. Several research groups have used this technique of monitoring a shift in the emitted electroluminescence peak of the VCSEL to obtain better spatial resolution; they have shown that a radial temperature distribution exists in VCSELs. While this technique, when used to examine various areas of the aperture, provides significantly better spatial resolution ($\sim 1\mu\text{m}$) than monitoring a shift in the lasing wavelength, it still does not provide sufficient resolution for smaller aperture VCSELs [5,6].

An additional technique, scanning thermal microscopy, was used by a group at the University of California at Berkeley to measure both the longitudinal and radial variation in temperature of a VCSEL [2]. By polishing a single VCSEL in half vertically, they were able to measure the temperature of the

various layers along the entire length of the laser cavity. Scanning thermal microscopy (SThM) has spatial resolution of $\sim 10\text{nm}$ and thermal resolution $\sim 1\text{mK}$. In this technique, a small thermocouple is moved across the polished surface of the VCSEL to measure the temperature of the various layers of the laser in both the longitudinal and radial directions [2]. This technique, however, can not be used on light emitting surfaces, such as the VCSEL aperture, and therefore is not a viable option for this research.

In our lab, we have developed a high resolution thermal imaging technique called thermoreflectance microscopy, which will be explained in more detail in Chapter 3. This technique measures the change in surface reflectivity of the device in order to determine its change in temperature. Thermoreflectance microscopy allows for high spatial (250nm) and thermal (10mK) resolution measurements of VCSELs and VCSEL arrays. Unlike previous temperature measurement techniques, thermoreflectance microscopy allows us to perform high resolution, non-contact, radial surface temperature measurements of light emitting surfaces, such as a VCSEL aperture. In the case of VCSEL arrays, thermoreflectance microscopy allows us to simultaneously measure the temperature across an array of lasers. The high spatial resolution of this technique also allows us to observe thermal lensing in the operating VCSEL and temperature gradients across the apertures of adjacent VCSELs in the array.

Overall, a variety of temperature measurements, shown in Table 1, have been developed to measure the temperature of VCSELs but only

thermoreflectance microscopy provides high enough spatial and thermal resolution while still being able to be used on light emitting surfaces.

Technique	Spatial Resolution	Thermal Resolution	Advantages	Disadvantages
Lasing Wavelength Shift [3,5,10]	None (bulk)	~100mK	Light emission necessary	No spatial resolution and low thermal resolution
Emitted Electroluminescence Wavelength Shift [6,10]	~1 μ m	~100mK	Light emission necessary	Low spatial and thermal resolution
Scanning Probe Thermography [2]	~10nm	~1mK	High spatial and thermal resolution	Cannot be used on light emitting surfaces and measures surface temperature only
Thermoreflectance Microscopy [11, 14]	~250nm	~10mK	Spatial resolution sufficient to resolve narrow aperture VCSEL; good thermal resolution; can be used on lasing VCSEL	Measures surface temperature only

Table 1.1: Comparison of temperature measurement techniques.

1.5 Overview of My Work

In this research, we use thermoreflectance microscopy to measure the thermal characteristics of single VCSELs (Chapter 4) and VCSEL arrays (Chapter 5). Chapter 4 discusses thermal effects in single VCSELs, compares the temperature distribution in three different types of VCSELs, and contrasts the temperatures measured using thermoreflectance, lasing wavelength shift, and emitted electroluminescence wavelength shift. Chapter 5 describes the research performed on VCSEL arrays, which consists of measuring the thermal coupling between individual lasers in the array using both thermoreflectance microscopy and shifts in the lasing wavelength, experimentally determining the thermal impedance and thermal conductivity of the VCSEL array, and conducting a time gating experiment to measure the thermal diffusivity of the VCSEL array.

2. VCSEL FUNDAMENTALS

Lasers are devices that are used for a variety of applications from communications to consumer electronics, medicine, and manufacturing. While many types of lasers exist, they all have the same basic structure consisting of two reflective mirrors spaced by some distance L , together called a Fabry Perot cavity, along with an optical gain region inside the cavity. This will be discussed in more detail in Section 2.1. The amplification of photons by stimulated emission takes place in the gain region, while the mirrors reflect the photons through the cavity numerous times to provide multiple opportunities for amplification. In addition, other processes such as spontaneous emission and absorption also take place in the gain medium. The basic features common to all semiconductor lasers will be discussed in Section 2.1, while the details specific to vertical cavity surface emitting lasers (VCSELs) will be discussed in Section 2.2.

2.1 Basic Semiconductor Laser Structure

2.1.1 Fabry Perot Cavity:

A Fabry Perot cavity, also known as a Fabry Perot etalon, consists of two highly reflective, parallel mirrors separated by a distance L , as shown in Figure

2.1.1. In addition, Figure 2.1.1 illustrates the multiple standing waves that form inside of the laser cavity; these are referred to as the lasers longitudinal modes.

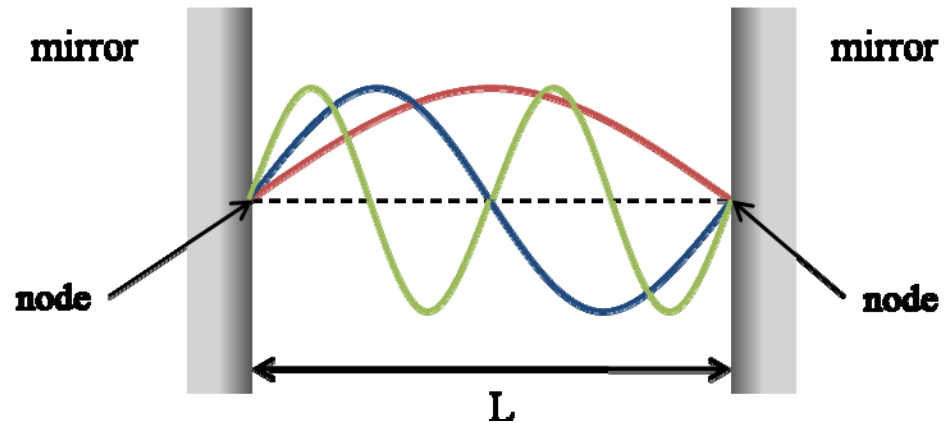


Figure 2.1.1: Standing waves in a Fabry Perot cavity.

If L is the distance between the two mirrors in the cavity, the standing wave frequencies can be calculated. A standing wave with amplitude A and wavelength λ is given by:

$$F(x) = -A \sin\left(\frac{2\pi}{\lambda} x\right) \quad (2.1)$$

Since the standing waves in the Fabry Perot cavity have nodes at both the mirrors:

$$F(x = 0) = F(x = L) = 0 \quad (2.2)$$

$$\frac{2\pi}{\lambda} = \frac{m\pi}{L}, m = 1, 2, 3, \dots \quad (2.3)$$

Hence, the wavelengths of the standing waves are:

$$\lambda_m = \frac{2L}{m} \quad (2.4)$$

The speed of light v , traveling through any given medium with refractive index n , is slower than the speed of light in a vacuum c_0 :

$$v = \frac{c_0}{n} \quad (2.5)$$

Combining equations 2.4 and 2.5, the frequency f_m of each standing wave, or longitudinal mode in the cavity, is:

$$f_m = \frac{v}{\lambda_m} = \frac{mc_0}{2Ln} \quad (2.6)$$

The frequency separation (Δf) of these longitudinal modes in the laser is given by:

$$\Delta f = f_m - f_{m-1} = \frac{c_0}{2Ln} \quad (2.7)$$

A theoretical plot of power versus frequency in a laser cavity with no loss, uniform gain, and perfectly reflecting mirrors is shown in Figure 2.1.2. In a lossless resonating cavity, standing waves exist only at discrete frequencies, one for each longitudinal mode of the laser.

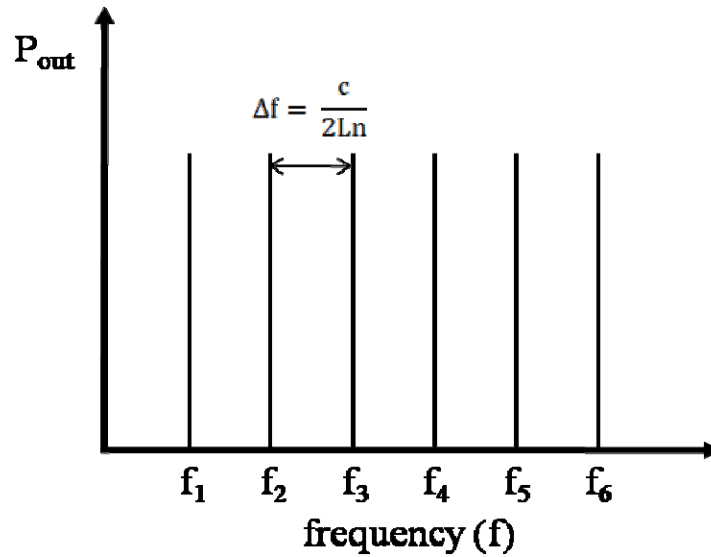


Figure 2.1.2: Output power versus frequency for an idealized Fabry Perot etalon (Perfectly reflecting mirrors ($R = 100\%$), no loss, and uniform gain).

Lasers, however, are not made with 100% reflecting mirrors since light needs to be emitted from the structure. In a Fabry Perot cavity with lossy or low reflectivity mirrors, the resonant cavity can support waves at a broader range of standing wave frequencies. At frequencies far away from the resonance, the attenuation resulting from destructive interference will greatly reduce the output power. Close to the resonant frequencies, the output power will be high due to the constructive interference of the waves in the cavity. Therefore, in the case of lossy mirrors, instead of each mode having a single frequency output, individual modes will have a slightly broadened peak as illustrated in Figure 2.1.3.

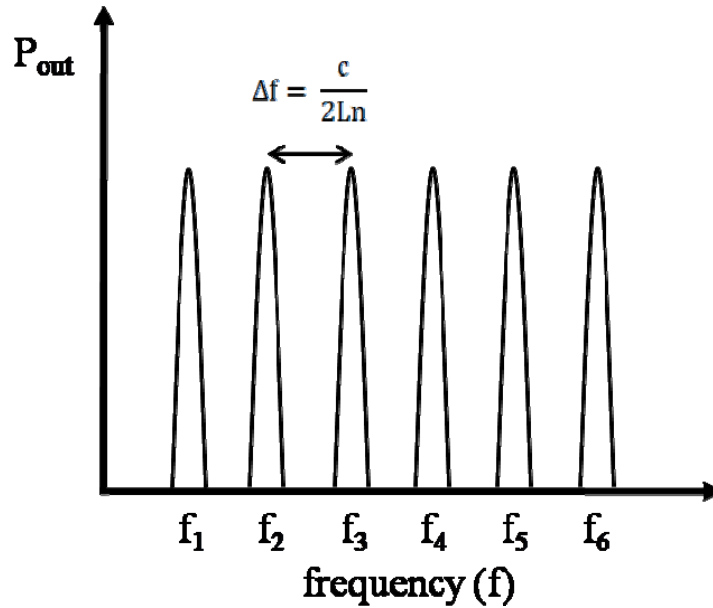


Figure 2.1.3: Output power versus frequency in VCSELs (R<100%).

Overall, only discrete frequencies of light f_m , corresponding to the longitudinal modes of the cavity, are resonant within the Fabry Perot cavity of a laser. In order for the photons at these select frequencies to be emitted from the laser, the longitudinal modes must also lie inside the gain spectrum, which will be discussed in the next section.

2.1.2 Gain in a Semiconductor Laser:

Atoms are the building blocks of all materials. We know from quantum mechanics that the energy of an electron in an atom is quantized, with E_0 being the lowest possible energy state, the ground state as shown in Figure 2.1.4a. Higher energy levels in the atom, $E_1, E_2,$ etc., can be reached only if the energy

level is initially unoccupied and the electron gains the energy required to make the jump from one discrete energy level to another.

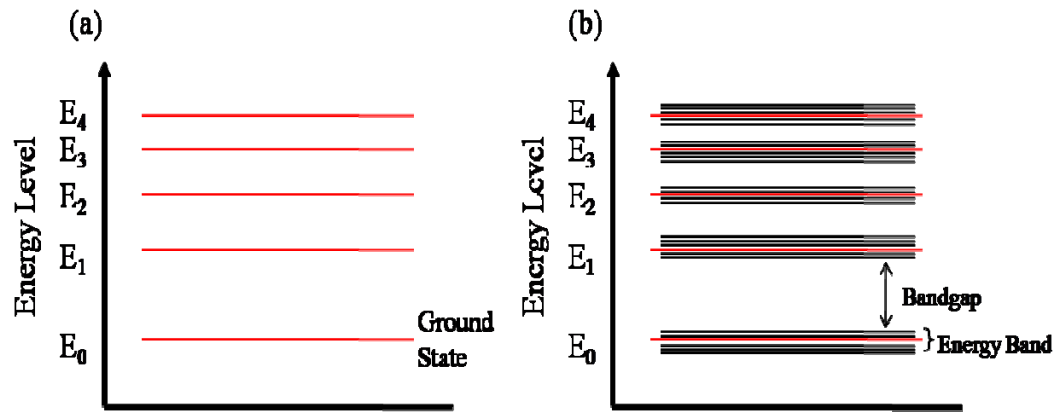


Figure 2.1.4: (a) Energy level diagram for a single atom (b) Energy level diagram for a crystal.

In contrast to the discrete energy levels of individual atoms, the tightly packed atoms of crystals result in the broadening of a single energy level into a band of allowed energy levels. These bands of allowed energies consist of many very closely grouped energy levels as shown in Figure 2.1.4b.

Two of the main energy bands of interest in solids are the valence band (E_v) and the conduction band (E_c), as shown in Figure 2.1.5. The valence band contains the highest energy level where electrons are present at absolute zero temperature ($T=0$). The conduction band is defined as the next highest energy band, where no electrons are present at absolute zero. The energy that separates these two energy bands is called the band gap energy (E_g) and is given by:

$$E_g = E_c - E_v \quad (2.8)$$

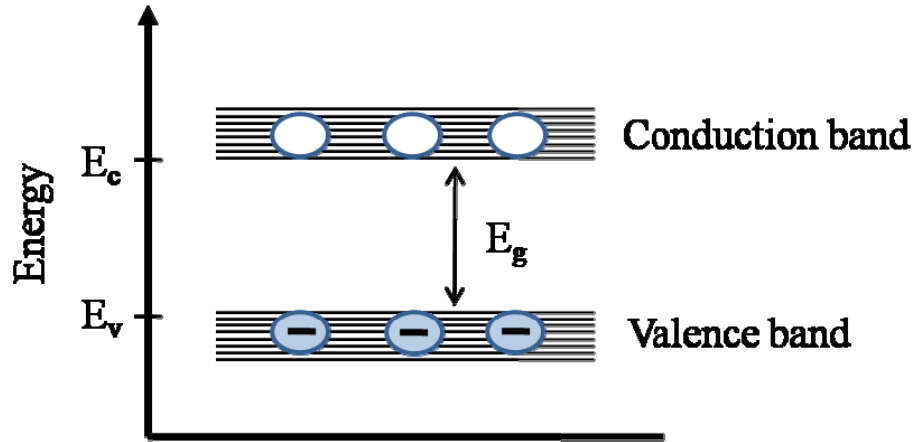
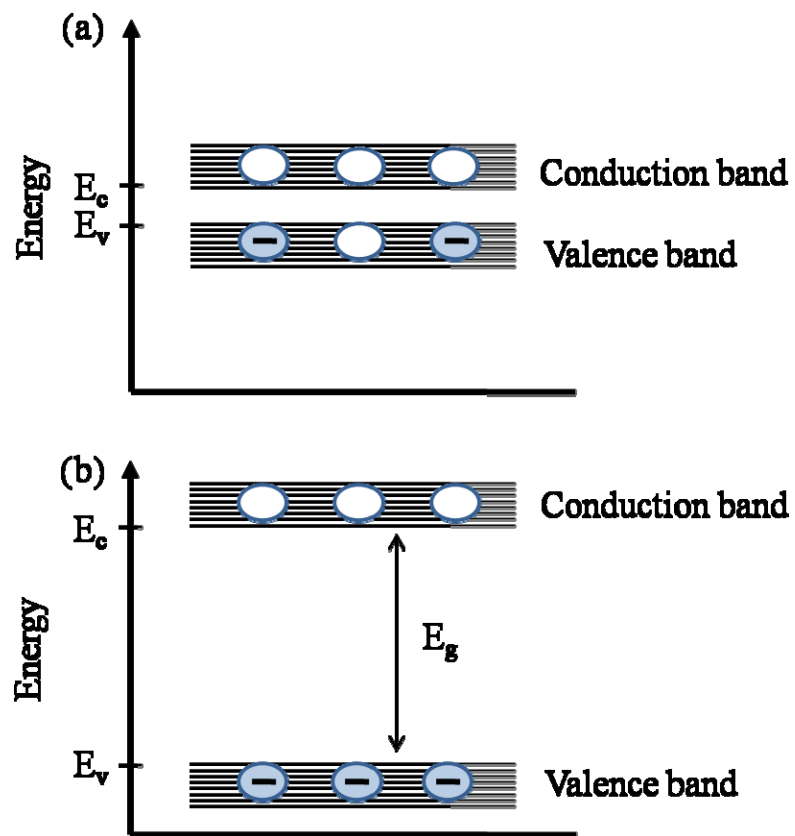


Figure 2.1.5: Energy level diagram showing valence band, conduction band, and band gap energy.

In conductors, the valence band is partially filled and the band gap energy is very low, as shown in Figure 2.1.6a. The small band gap energy allows for the slight addition of thermal energy to cause electrons to jump from the valence to the conduction band. This easy movement of electrons from one energy state to another makes for a good conducting material.

In contrast, the valence band in insulators is completely full of electrons at absolute zero as shown in Figure 2.1.6b. In addition, the band gap energy for an insulator is very large which therefore makes it very difficult for electrons to move between the different energy bands, even with the addition of thermal energy or electrical bias.

Semiconductors have properties similar to both conductors and insulators, as shown in Figure 2.1.6c. They have a full valence band at $T = 0$; however, the band gap energy in these types of materials is much smaller than that of insulators. Therefore, electrons in a semiconductor can more easily jump between the valence and conduction bands due to temperature fluctuations or the addition of electrical bias.



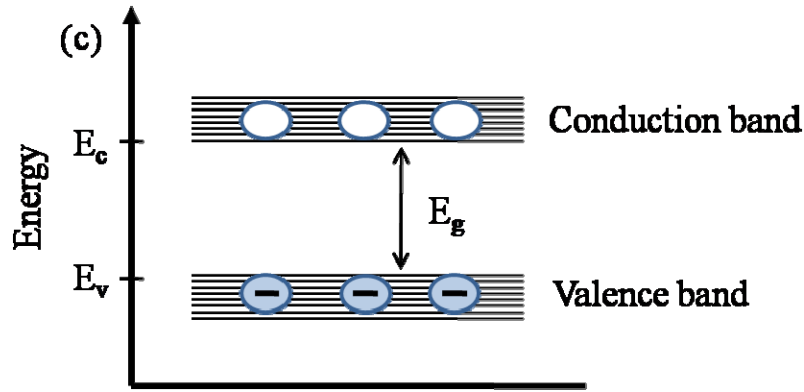


Figure 2.1.6: Energy level diagram for (a) conductors (b) insulators (c) semiconductors.

In this work, we are concerned with semiconductor lasers that in thermal equilibrium typically have the majority of the electrons located in the valence band. In order for lasing to occur, however, it is necessary for the excited state (the conduction band) to contain more electrons than the lower state (the valence band), which is known as a population inversion. Population inversion is necessary for the amplification of light, and under these conditions the material is known as an active medium.

There are several gain and absorption processes that take place inside the active region of the laser. The first of these processes is spontaneous emission, in which an electron from the conduction band decays spontaneously to the valence band. The energy lost by the electron in this transition is released in the form of a photon, with random direction and phase, as shown in Figure 2.1.7.

$$E_{\text{photon}} = h\nu = \Delta E_{\text{electron}} \approx E_c - E_v \quad (2.9)$$

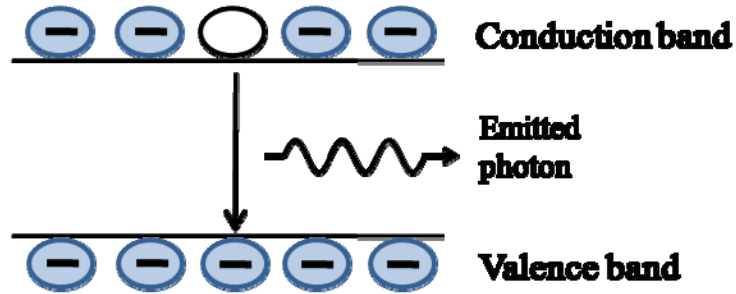


Figure 2.1.7: Spontaneous emission.

Stimulated emission, the source of gain in lasing materials, is the process in which a photon with energy roughly equal to the band gap energy interacts with the semiconductor material and causes an electron in the conduction band to decay to the valence band. The loss of energy of the electron results in the release of a second photon with energy equal to that of the original photon, as shown in Figure 2.1.8. This second photon is identical to the incident photon in that it has the same phase, direction, and energy. Due to the fact that the photons are identical, a coherent light beam is emitted from the lasing device.

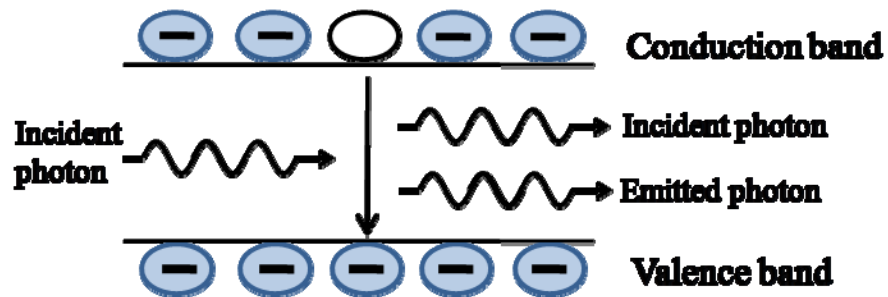


Figure 2.1.8: Stimulated emission.

Stimulated absorption is a process in which a photon with energy slightly greater than the band gap energy is incident on the material. In this case, unlike the previous two, no photons are emitted during the process, as illustrated in Figure 2.1.9. Instead, the energy of the photon causes an electron in the valence band to move to the conduction band, absorbing the energy from the photon.

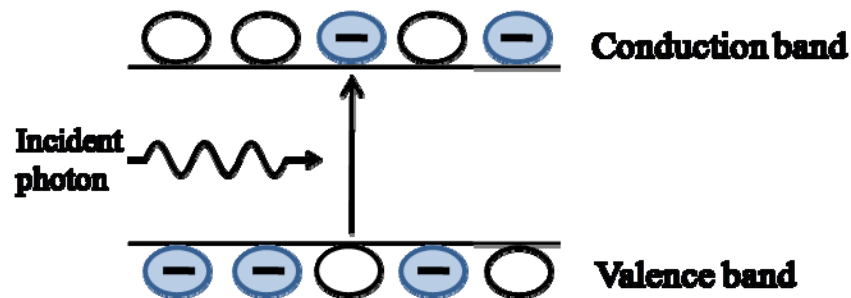


Figure 2.1.9: Stimulated absorption.

In addition to the processes described here, there are a variety of other possible non-radiative processes, such as scattering from defects, which reduce the overall operating efficiency of the laser. The gain medium will amplify light when the emission events described above, spontaneous and stimulated emission, occur more frequently than absorption events in combination with other photon loss mechanisms. It is important to note that while the number of photons produced may exceed those absorbed this does not guarantee lasing because of the many sources of optical loss that exist in the laser. The main source of this loss is the partially reflecting mirrors, with additional loss due to the absorption in the gain medium, scattering, and various other mechanisms. All of these cavity losses must be overcome in order for lasing to occur.

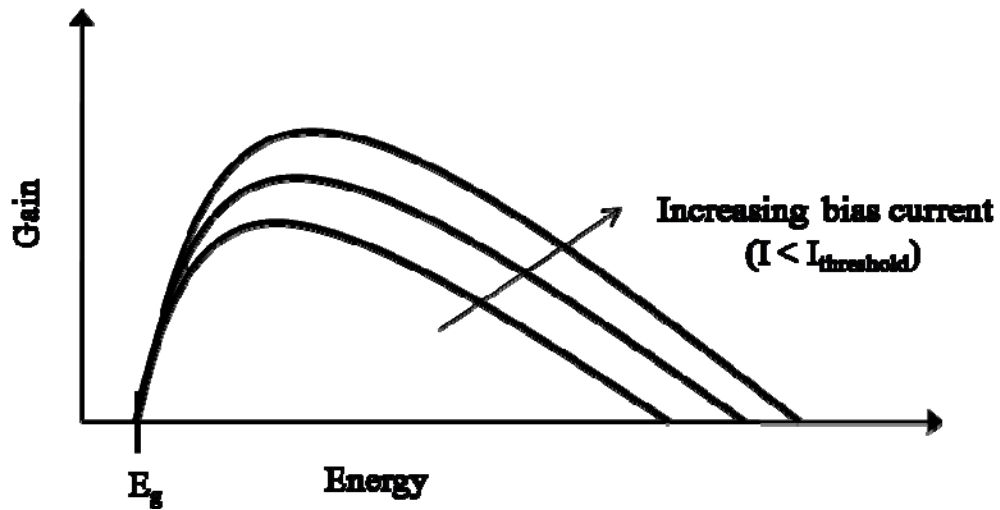


Figure 2.1.10: Gain spectrum for a laser.

Optical gain is defined as the number of photons produced by stimulated emission minus those lost due to absorption and other miscellaneous losses. Figure 2.1.10 shows a schematic of the gain spectrum, the total amount of gain within the lasing cavity for a given energy. One important feature is that the band gap energy (E_g) is the lowest possible energy that an incident photon can have in order for gain to occur in the active medium. By increasing the bias current to the laser, more electrons populate the conduction band, resulting in a higher probability of stimulated emission. The population of the higher energy levels with increasing current density results in a shift in the gain spectrum as shown in Figure 2.1.10. At the threshold current, discussed in greater detail in Section 2.2.6, the gain is equal to the loss in cavity and there is no longer an increase in the gain spectrum.

The shape of the gain spectrum can best be described by looking at the location of electron-hole pairs in the gain material. In order for a given incident photon with energy E_{photon} to cause a stimulated emission event, there must be an electron in the conduction band and hole in the valence band (an electron-hole pair) with energy separation equal to E_{photon} . The majority of the electrons in the conduction band are located near the bottom of the conduction band, while the majority of holes in the valence band are located near the top of the valence band, as shown in Figure 2.1.11.

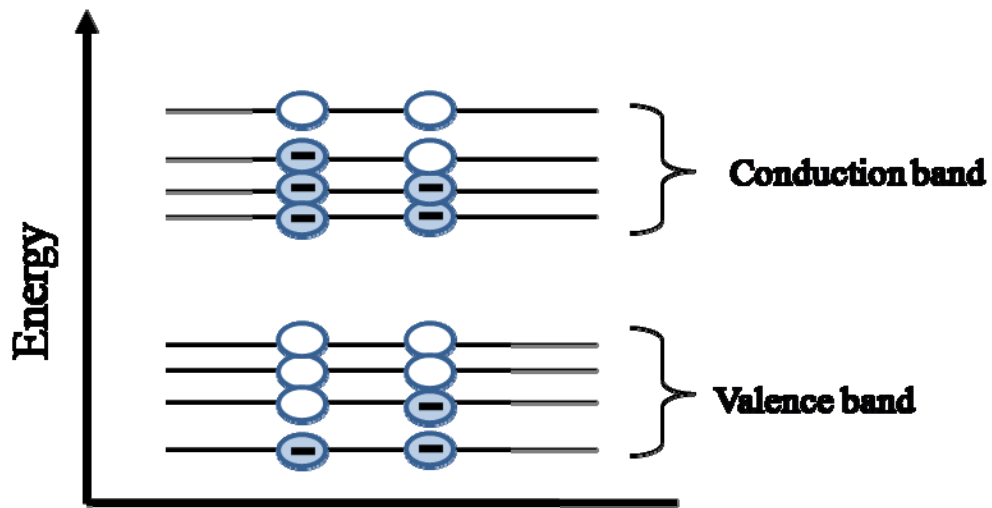


Figure 2.1.11: Electron and hole distribution in gain medium.

It is therefore more probable for an incident photon to cause an electron to move from an energy level near the bottom of the conduction band to a level near the top of the valence band, labeled Transition 1 in Figure 2.1.12, than it is for an electron in a higher energy level within the conduction band to move to a lower energy level within the valence band, labeled Transition 2 in Figure 2.1.12. This

results in the greatest gain for incident photon energies closest to the bandgap energy (E_g). As the incident photon energy increases, it is less likely that there will exist an electron-hole pair with that energy separation in the gain material. Therefore, the gain spectrum, Figure 2.1.10, decreases at higher energies.

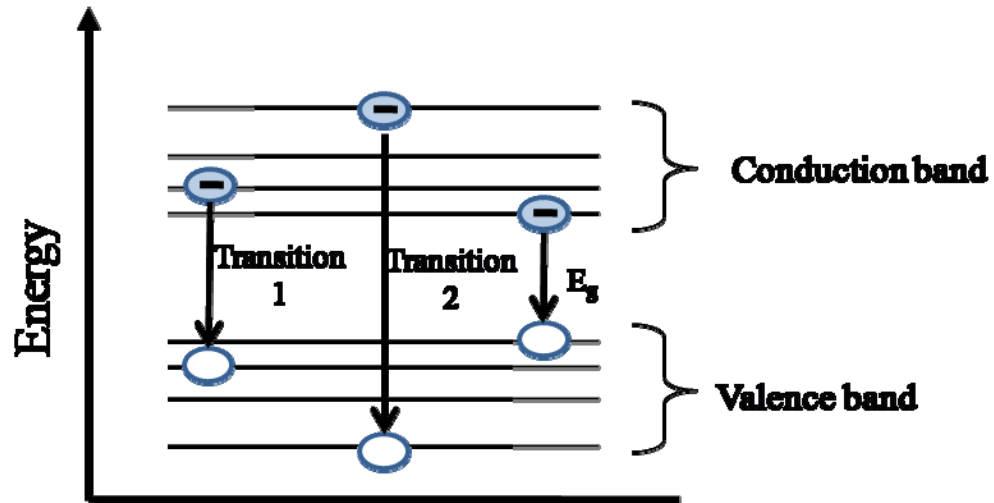


Figure 2.1.12: Electron hole recombination in gain medium.

2.2 Vertical Cavity Surface Emitting Lasers (VCSELs)

2.2.1 Overview of VCSEL Structure:

Vertical cavity surface emitting lasers (VCSELs) are cylindrical semiconductor lasers with light emitted vertically from the top or bottom surface with respect to the semiconductor surface on which they are grown and patterned.

Typically, VCSELs are formed by growing or bonding various crystalline semiconductor layers and materials one on top of another as shown in Figure 2.2.1. While Figure 2.2.1 shows the structure of the standard VCSEL used in most commercial applications, there are many possible geometries for VCSELs.

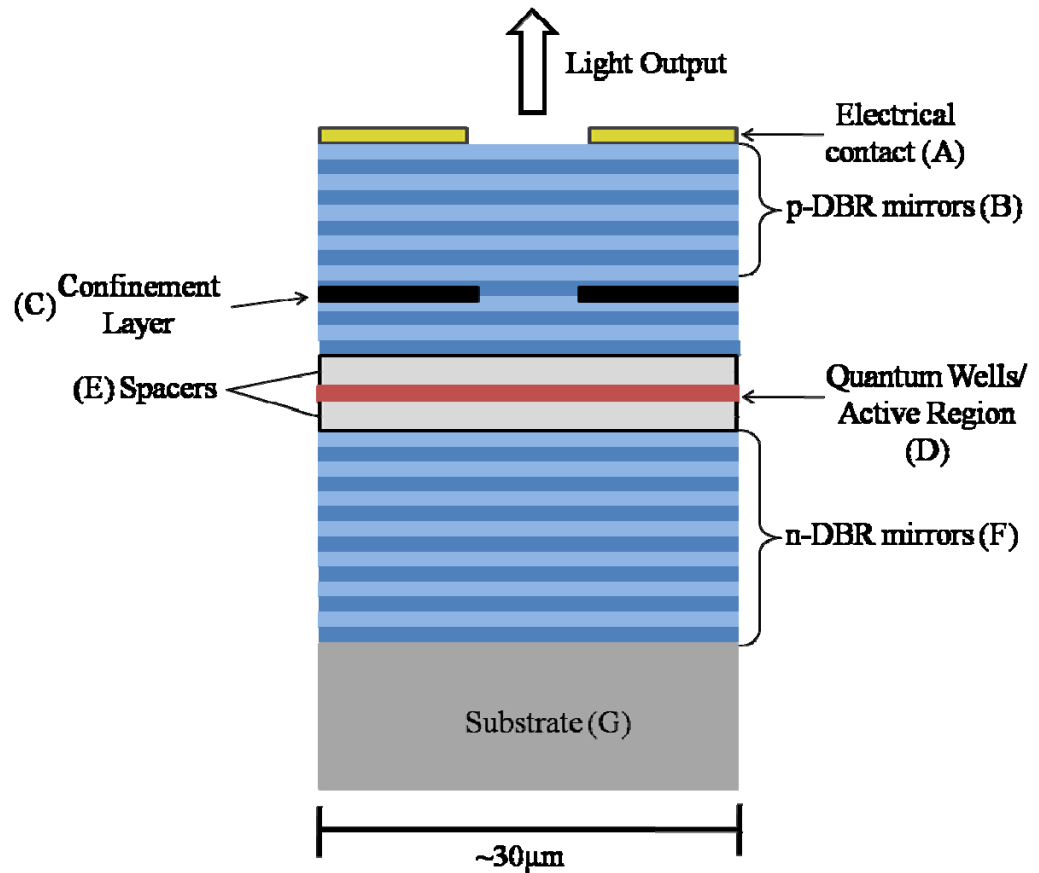


Figure 2.2.1: Typical vertical cavity surface emitting laser (VCSEL) structure viewed in cross-section.

Various types of materials are used in the fabrication of these lasers, in order to control the wavelength of the resulting light and threshold current. Some of the common combinations of materials include AlGaAs / GaAs ($\lambda_{\text{output}} = 680\text{nm}-890\text{nm}$), InGaAs / GaAs ($\lambda_{\text{output}} = 950\text{nm}-1100\text{nm}$), InGaAsP / InP (λ_{output}

= 1000nm-1700nm), AlGaInP / GaAs ($\lambda_{\text{output}} = 600\text{nm}-700\text{nm}$), etc. [15]. The VCSELs used in this work and discussed in Chapters 4 and 5 are made from gallium arsenide (GaAs) and aluminum gallium arsenide (AlGaAs) and emit at $\lambda_{\text{output}} = 850\text{nm}$. Several techniques including molecular beam epitaxy (MBE) and metal-organic chemical vapor phase epitaxy (MOVPE) are used to grow the layers of VCSELs on top of each other [16,17].

VCSELs are typically about $8\mu\text{m}$ tall and have a top aperture ranging between $10\mu\text{m}$ and $20\mu\text{m}$ depending on the fabrication and application. The various layers of the VCSEL are labeled (A-G) in Figure 2.2.1 and summarized below. More detailed discussions of distributed Bragg reflector mirrors and the gain medium are provided in following sections.

A. Electrical Contact

Typically made of gold, the annular top layer of VCSELs is where current is injected into the device. This metal contact is usually ring shaped to help with the even distribution of current to the laser, and light is emitted through the center aperture in the contact [18].

B. Upper Bragg Mirror (p-type)

The upper distributed Bragg reflector (DBR) mirrors are generally made by stacking 30-40 alternating layers of semiconductor material with slightly different indices of refraction. These DBR mirrors are commonly used in VCSELs because of their high reflectivity due to the constructive interference of the reflection from each layer of the mirror. Each layer is fabricated to be one

quarter wavelength thick to ensure constructive interference and a high total mirror reflectivity; this is discussed in greater detail in Section 2.2.4. This top p-type Bragg reflector is doped in order to increase the number of positive free charge carriers, or holes, in the material. The result of this doping is the creation of holes, empty energy states in the valence band where electrons could be [15]. In other words, these vacant energy states in the valence band can be injected into the active region to allow for a population inversion.

C. Confinement Layer

The confinement layer is used to control the flow of electrical current into the active region. In addition, the confinement layer is sometimes also used to confine the light to the center of the laser in order to improve the beam quality emitted from the central aperture. There are several techniques for achieving these desired effects, including proton implantation and oxide confinement. These techniques involve damaging a portion of the upper DBR mirrors in order to control the current path through the laser, as well as in some cases controlling the spatial distribution of the light [19].

Proton Implantation:

In this technique, extra protons are injected into the confinement layer during fabrication, damaging a ring-shaped layer of material and making it highly resistive, thus controlling the flow of electrical current. In addition to confining the current, the damaged area has a different index of refraction which allows for relatively weak optical confinement.

Oxide Confinement:

Oxide confinement is a technique in which, in the fabrication of the VCSEL, a layer of material is grown that allows for oxidation to take place. As in the case of proton implantation, this oxidation damages a ring shaped portion of the upper mirror. In addition to confining the current through the laser, this technique also allows for strong light confinement because the oxidized region is opaque at the lasing wavelength. Oxide confinement is used to create both single transverse mode and multimode VCSELs [19]. In the case of single mode VCSELs, the oxide confinement layer allows only the fundamental transverse mode of the cavity to lase. In the multimode case, this layer allows for additional transverse modes in the cavity. See Section 2.2.3 for a discussion of transverse modes.

D. Active Region/ Quantum Wells

The active region, consisting of multiple quantum wells, is the region in VCSELs where optical gain occurs and the light is amplified. These processes were discussed in greater detail in Section 2.1.2.

E. Spacers

A layer of spacers is included on either side of the active region to maximize the amplitude of the electromagnetic field at the active region. The spacers are positioned so that the gain region is aligned with the peak of the standing longitudinal wave.

F. Lower Bragg Mirror (n-type)

Similar to the distributed Bragg reflector mirror discussed above, the lower Bragg reflectors are located below the active region and contain between 30-40 layers of alternating material. This lower Bragg mirror, however, is doped so that there is an excess of negative free charge carriers, or electrons, in the conduction band.

G. Substrate

The bottom layer of the VCSEL is referred to as the substrate and is generally a n-doped layer on which all of the above layers are stacked. In a VCSEL, current is injected into the metal contact at the top and travels down to the substrate.

2.2.2 Lasing Frequency/ Longitudinal Modes:

The lasing frequency in a vertical cavity surface emitting laser is determined by which of the longitudinal modes lies in the gain spectrum. Figure 2.2.2 shows an overlay of the longitudinal mode frequencies (Figure 2.1.3) and the gain spectrum (Figure 2.1.10) discussed earlier. As can be seen, in vertical cavity surface emitting lasers, only one longitudinal mode falls inside of the gain spectrum because the very short cavity length leads to a large frequency separation between modes. Having a single longitudinal mode inside the gain

spectrum eliminates the possibility of mode hopping in VCSELs, which is a common problem in edge-emitting semiconductor lasers.

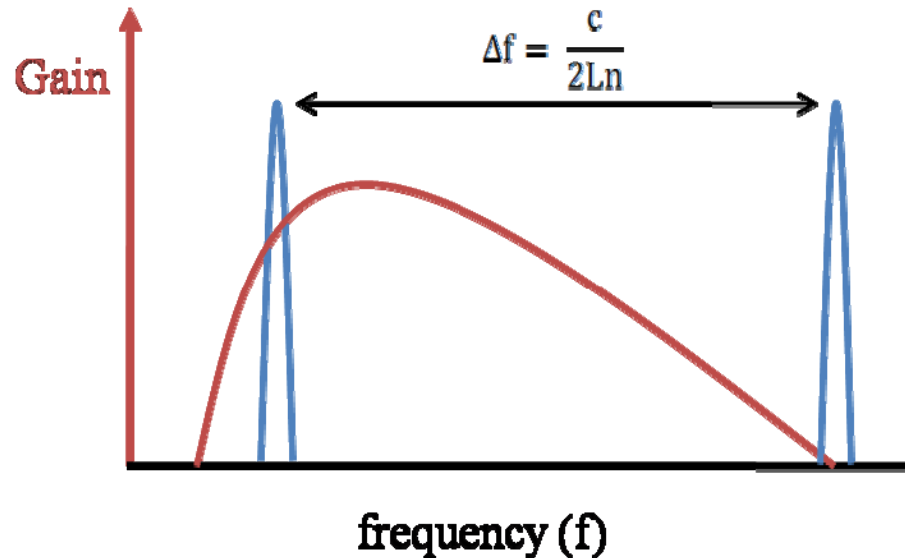


Figure 2.2.2: Overlay of longitudinal mode frequencies and gain spectrum in a VCSEL with Fabry Perot length L.

An example of a lasing longitudinal mode in a Fabry Perot cavity for a single mode VCSEL is shown in Figure 2.2.3. An increase in temperature of the VCSEL will cause shifts in the gain and the longitudinal mode of the laser and therefore a change in the lasing wavelength. Because VCSELs are very resistive devices, during their operation they get very warm due to resistive heating. Therefore, applying additional current to the VCSEL will cause an increase in its temperature as well as a shift in the lasing wavelength. Monitoring this shift in the lasing wavelength, as will be seen in later chapters, allows us to measure the change in temperature of a VCSEL.

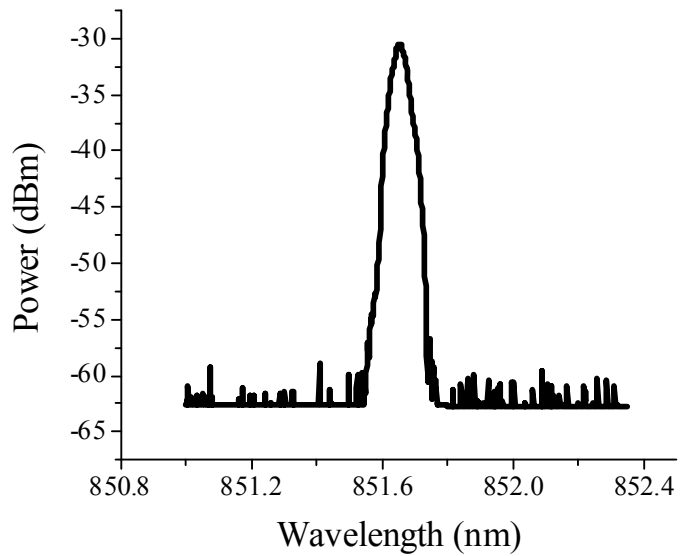


Figure 2.2.3: Typical lasing spectrum of a single transverse mode oxide confined VCSEL biased at 4mA.

2.2.3 Transverse Modes:

Although VCSELs lase in a single longitudinal mode, there are typically many possible transverse modes in a VCSEL. Transverse modes are standing waves that extend in the direction across the width of the cavity and have nodes on the edges of the cavity structure, as shown in Figure 2.2.4. These transverse modes represent the amplitude distribution of the electromagnetic field of the photons perpendicular to the propagation of the laser beam inside the cavity [19]. Transverse modes occur because of the boundary conditions imposed by the

cavity and determine both the output beam shape for the laser as well as the lasing spectrum for a VCSEL.

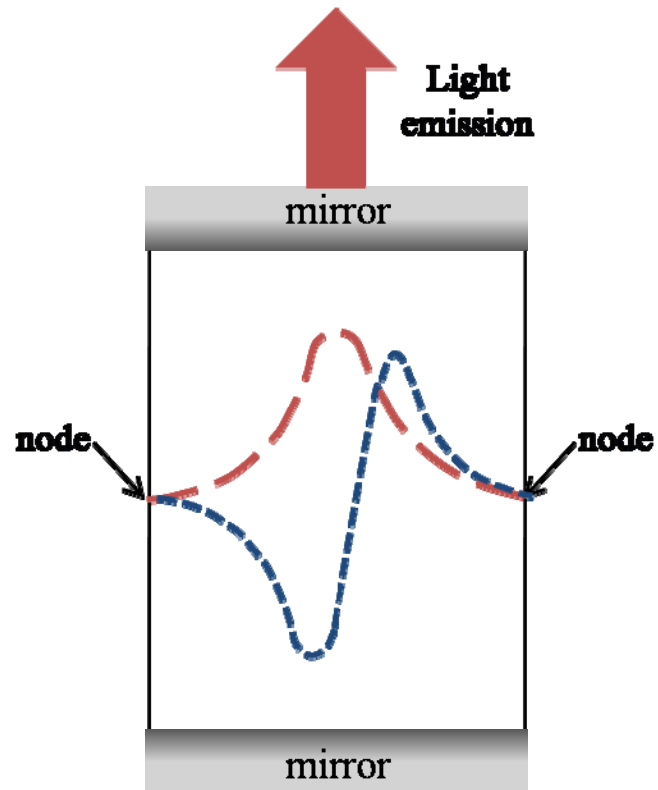


Figure 2.2.4: Standing waves in a 1-D Fabry Perot cavity resulting in transverse modes.

To best understand how the transverse modes affect the output beam shape of a VCSEL, one must realize that the transverse standing waves in the cavity are the “drumhead modes”, described by Hermite-Gaussian functions. Several of the lower order 1-D Hermite Gaussian functions (G_0 , G_1 , G_2 , and G_3) are shown in Figure 2.2.5a. The output beam shape of the VCSEL is determined by the two dimensional combination of the transverse waves, which together form a Hermite-

Gaussian beam of order (l,m). Several possible output beam shapes for lower order Hermite Gaussian beams are shown in Figure 2.2.5b.

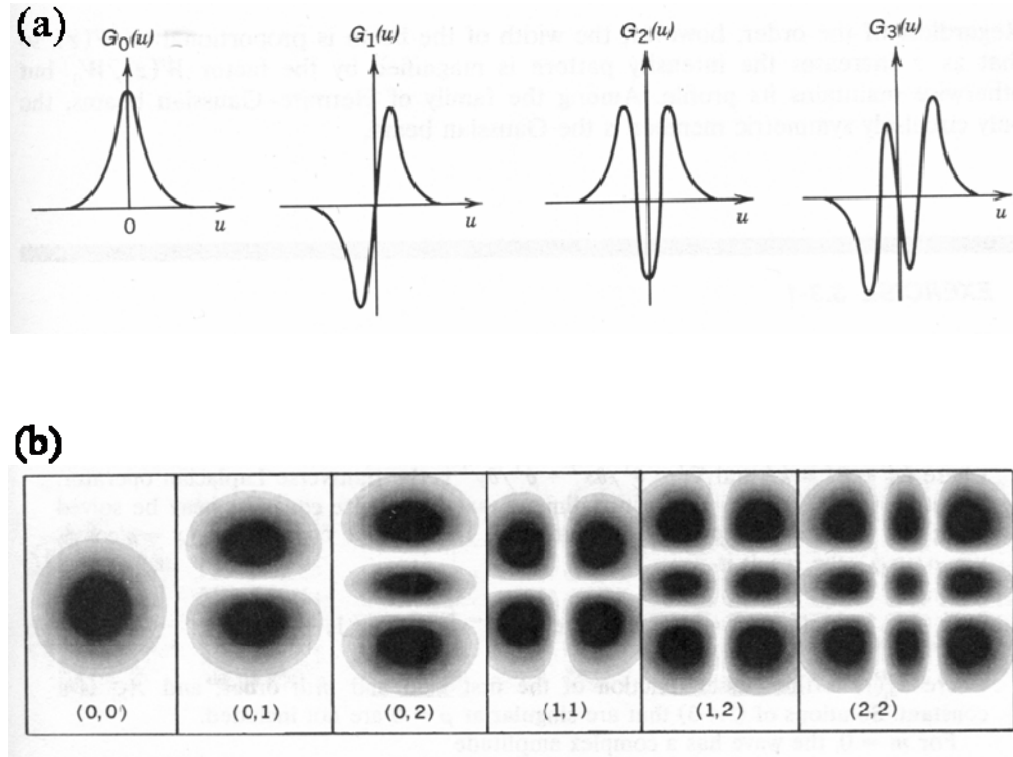


Figure 2.2.5: (a) Hermite Gaussian functions (b) Output beam shapes for a rectangular aperture VCSEL of order (l,m) [19].

If the transverse amplitude distribution is described by a single Gaussian curve across the laser cross section, shown in the left most picture in Figure 2.2.5b, the VCSEL is said to be lasing in the fundamental transverse mode. VCSELs that only lase in the fundamental transverse mode, regardless of applied bias current, are called single mode VCSELs. Multimode VCSELs typically lase in the fundamental transverse mode at low bias currents, but higher order transverse modes appear as the bias current increases.

In addition to determining the output beam shape of the laser, the transverse modes in a VCSEL change the laser's optical spectrum. While VCSELs only have one longitudinal mode, each of the transverse modes lase at a slightly different frequency depending on the effective refractive index seen by the mode. A VCSEL with a single transverse mode has a lasing spectrum shown previously in Figure 2.2.3 and is referred to as a single mode laser. When more transverse modes are present, additional peaks, as shown in Figure 2.2.6, become apparent in the lasing spectrum. These types of VCSELs are known as multimode lasers.

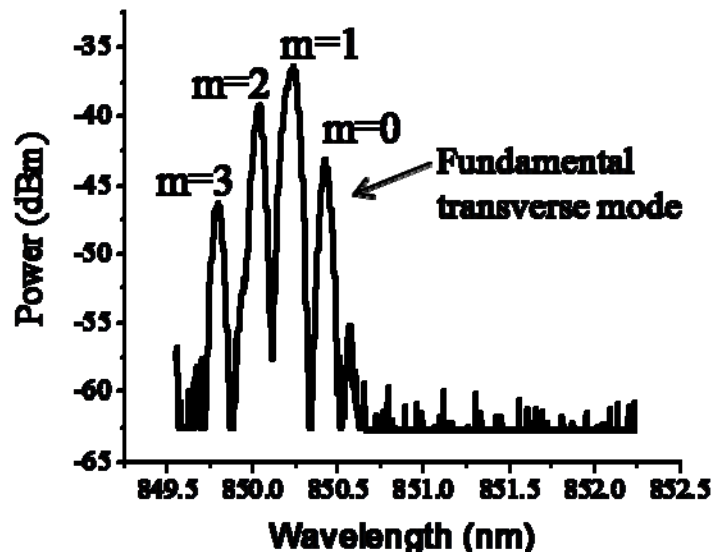


Figure 2.2.6: Lasing spectrum of a VCSEL with multiple transverse modes (m).

2.2.4 Distributed Bragg Reflector Mirrors:

When choosing the materials for the distributed Bragg reflector mirrors in VCSELs, it is important that the structure have high reflectivity, low thermal

resistance, and be compatible for growth on or bonding to the gain layer. Because the gain region in VCSELs is so small, it is necessary to have very highly reflective (~99.8%) mirrors so that the photons in the cavity will pass through the gain region numerous times. The mirrors in VCSELs are made by alternating thin layers of two semiconductor materials that have slightly different indices of refraction. In order to achieve high reflectivity, each set of mirrors in a VCSEL usually consists of approximately 30 pairs of semiconductors on either side of the gain medium. For example, a VCSEL which consists of 15 layer pairs has a reflectivity of 98%, while a laser with 30 layer pairs has a reflectivity of 99.96% [20].

A Bragg mirror is a structure that is made from alternating semiconducting materials of different indices of refraction, see Figure 2.2.8. The majority of photons are perpendicularly incident on the interfaces between the two materials [20]. For a wave that is normally incident on an interface between two materials with refractive indices n_1 and n_2 , the field reflectivity r is the ratio of the reflected electric field to the incident electric field. From the Fresnel equations, one can show:

$$r = \frac{E_{\text{reflected}}}{E_{\text{incident}}} = \frac{n_1 - n_2}{n_1 + n_2} \quad (2.10)$$

where the wave starts in the medium with index of refraction n_1 . Because power is proportional to the absolute value of the electric field squared $P \sim |E|^2$ the power reflectivity R is:

$$R = \frac{P_{\text{reflected}}}{P_{\text{incident}}} = r^2 = \left(\frac{n_1 - n_2}{n_1 + n_2} \right)^2 \quad (2.11)$$

It is interesting to note that when $n_1 > n_2$ the reflection coefficient is positive and there is no phase shift in the reflected beam relative to the incident beam, as shown in Figure 2.2.7a. However, when $n_1 < n_2$, the reflection coefficient is negative, which corresponds to a phase shift of π in the reflected beam relative to the incident beam, as shown in Figure 2.2.7b. Regardless of which material has the higher refractive index, the transmitted beam will always have the same phase as the incident beam.

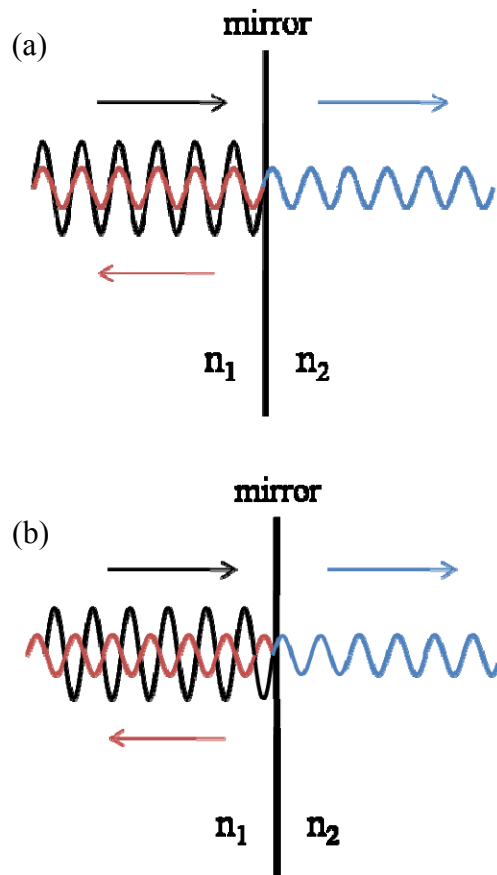


Figure 2.2.7: Phase shift resulting from a wave incident on a mirror when (a) $n_1 > n_2$ ($\varphi = 0$) (b) $n_1 < n_2$ ($\varphi = \pi$).

In order to fully understand how a Bragg mirror works in a VCSEL it is important to look at the interaction at several material pair interfaces (1, 2, 3, etc.) in the mirror stack. As shown in Figure 2.2.8, the thickness of each layer of material is equal to one quarter the wavelength of the longitudinal mode in that material (thickness = $n\lambda_0/4$). When this ideal condition is met, the incident and all of the reflected beams constructively interfere, yielding a large overall reflectivity R for the mirror stack.

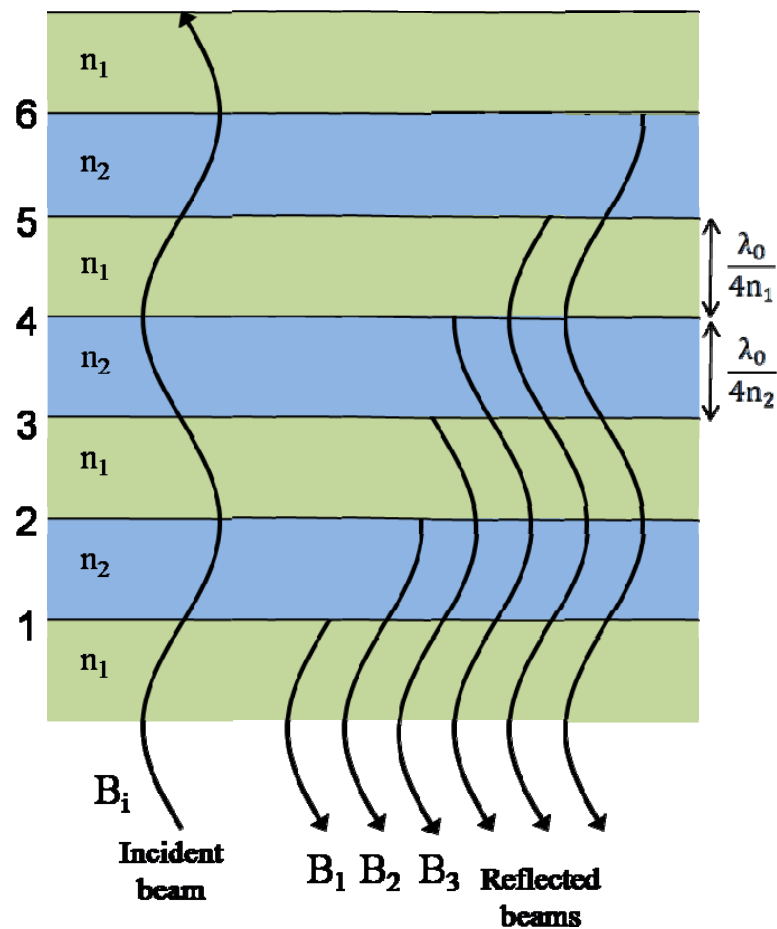


Figure 2.2.8: Distributed Bragg reflected mirror with reflection at each interface.

Consider the case of an incident light wave B_i of free space wavelength λ_0 that is exactly matched to the mirror layers. Take the phase of the incident beam to be $\varphi=0$ when it first enters the mirror at the bottom of the figure and $n_1 > n_2$. Then the beam B_1 , which results from the reflection off the first interface, has no additional phase shift at the boundary so $\varphi_1 = 0$ and the incident and reflected beams are in phase. Beam B_2 , which results from the reflection off the second interface, has traveled an additional distance of $\lambda/2$ compared to the first reflected wave and has an additional phase shift of π at the boundary. Therefore, the total phase shift of the second reflected wave is equal to:

$$\varphi_2 = k \left(\frac{\lambda}{2} \right) + \pi = \left(\frac{2\pi}{\lambda} \right) \left(\frac{\lambda}{2} \right) + \pi = 2\pi \quad (2.12)$$

The third beam B_3 , which results from the reflection off the third interface, has traveled an additional distance of λ compared to the first reflected wave, but has no additional phase shift at the boundary, so $\varphi_3 = 2\pi$. Lastly, the fourth beam B_4 has traveled an additional distance of $3\lambda/2$ compared to the first reflected wave. In addition, the fourth interface results in a phase shift of π , making the total phase shift of B_4 equal to $\varphi_4 = 4\pi$. Hence, all of the reflected beams add in phase and interfere constructively within the distributed Bragg reflector mirrors.

The reflectivity spectrum for distributed Bragg reflector mirrors is shown in Figure 2.2.9.

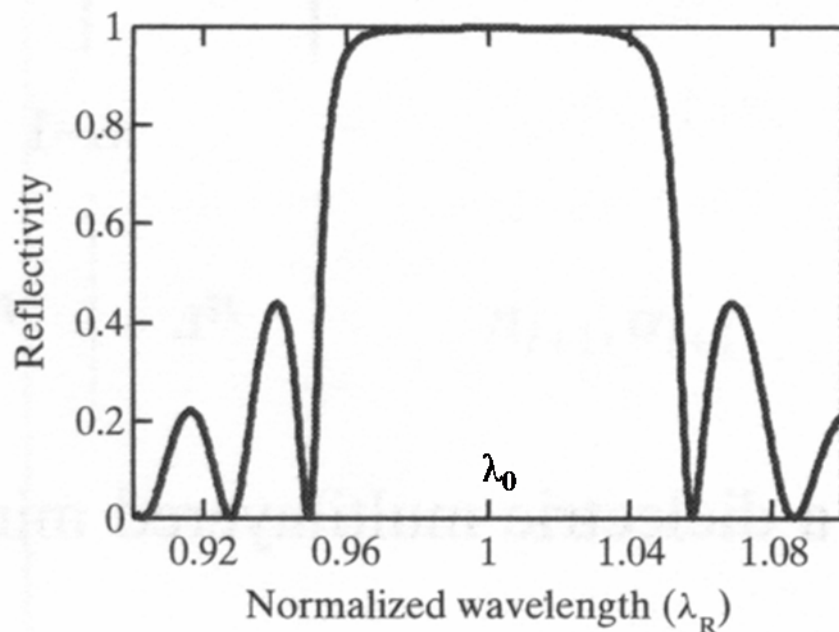


Figure 2.2.9: Example reflectivity spectrum for DBR mirrors in a VCSEL [19].

The shape of the reflectivity spectrum is produced by the wavelength dependent interference conditions at the Bragg mirror. At λ_0 , the design wavelength of the laser, total constructive interference at the mirrors leads to a high mirror reflectivity. At wavelengths further away from the design wavelength, a decrease in the reflectivity results because the interference of the longitudinal back reflected waves at the individual interfaces in the mirror no longer interfere entirely constructively.

Ideally, the VCSEL distributed Bragg reflector mirrors are designed such that the layer thickness ($\lambda_0/4$) exactly matches the lasing wavelength (λ_0) of the laser. An increase in temperature of the laser cavity, however, results in a shift in the lasing wavelength. Since each layer of the mirrors in the VCSEL is no longer

equal to one quarter of the new lasing wavelength, the reflectivity of the total DBR mirrors decreases as mentioned above [21].

2.2.5 Gain Medium:

The gain medium in a laser is the location where optical amplification takes place. In VCSELs, the gain medium consists of semiconductor quantum wells. These quantum wells are formed by sandwiching a material, in our case gallium arsenide (GaAs), between two layers with a larger bandgap, aluminum gallium arsenide (AlGaAs), as shown in Figure 2.2.10.

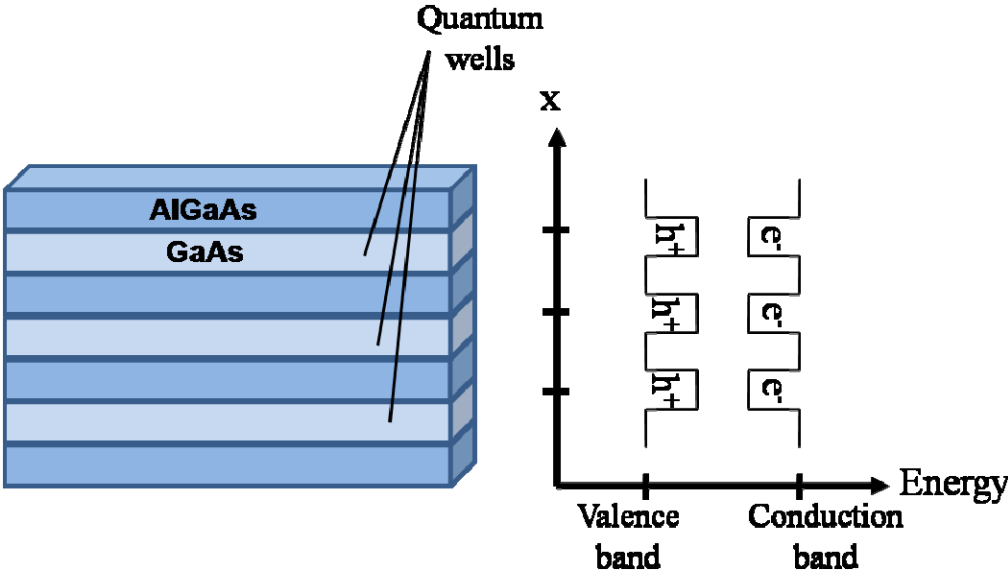


Figure 2.2.10: Illustration of quantum well and energy band structure in active region of a VCSEL.

In general, the active region of a VCSEL consists of two or three quantum wells. The thickness of each quantum well (GaAs layers), whose purpose it is to confine the electrons as shown in the energy band structure in Figure 2.2.10, is comparable to the de Broglie wavelength for an electron in the material, given by Equation 2.12 where h is Planck's constant and p , m , and v are the momentum, mass, and velocity of a particle in the material.

$$\lambda = \frac{h}{p} = \frac{h}{mv} \quad (2.12)$$

Therefore, the thickness of the GaAs quantum well layer in a VCSEL is typically around 10nm, while the AlGaAs spacers are usually slightly thicker, leading to a total thickness of the quantum well stack of approximately 60nm [20].

One of the main advantages to using semiconductor quantum wells in a laser instead of other types of gain materials is their ability to reduce the threshold current of the device. The presence of quantum wells in the active region of VCSELs changes the density of states in the laser and therefore reduces the number of electrons and holes needed for lasing to occur.

2.2.6 Standard Operating Characteristics of VCSELs:

The previous sections have discussed the physics behind how a VCSEL operates. There are several characteristics of VCSELs that will play an important role in the analysis of data in subsequent chapters.

Figure 2.2.11 shows a graph of the output power versus current, known as the LI curve, for a typical VCSEL. There are several important regions to point out when looking at an LI curve including the threshold current, spontaneous emission, and stimulated emission. The threshold current is the current where lasing begins and the point where the gain in the laser is equal to all of the losses in the cavity. Below the threshold current most of the detected light output is due to spontaneous emission, while above the threshold current most is due to stimulated emission. In addition, Figure 2.2.11 shows a plot of the voltage versus current, known as the IV curve, for a VCSEL.

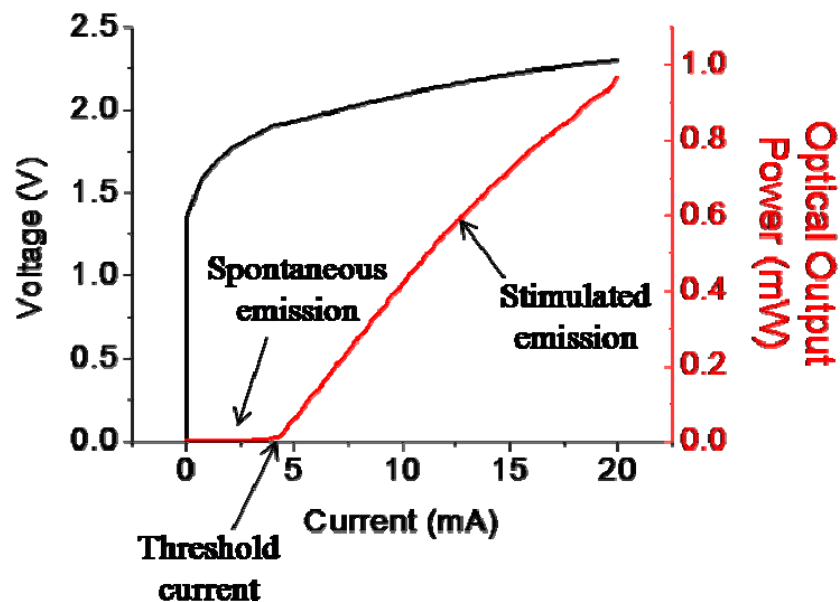


Figure 2.2.11: LI and IV curve for a VCSEL.

A typical lasing spectrum for a VCSEL can be seen in Figure 2.2.12. One can clearly see the broad low-power range of the spontaneous emission in addition to the sharp peak of the stimulated emission.

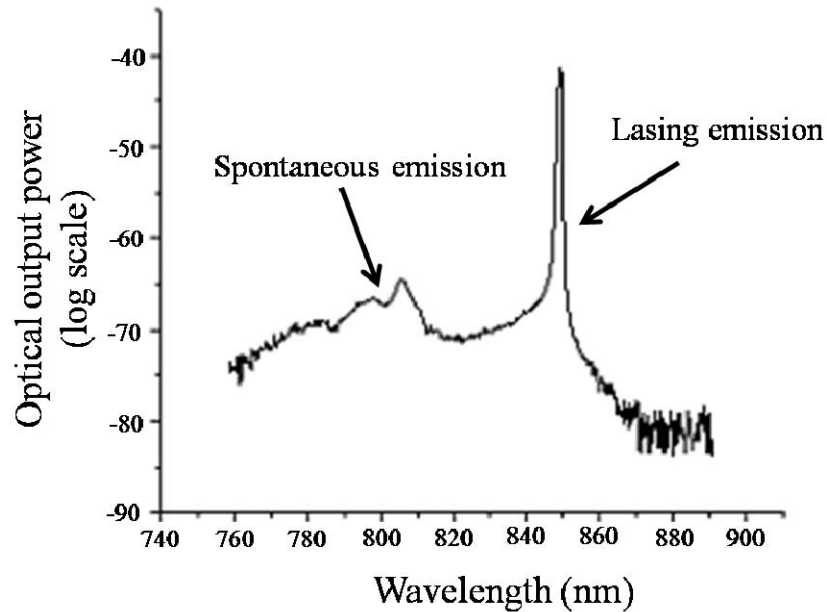


Figure 2.2.12: Lasing spectrum for VCSEL biased above threshold, showing both spontaneous and lasing emission [11].

Lasing spectra for oxide confined single mode VCSELs at various bias currents are shown in Figure 2.2.13. At both low and high currents, only a single longitudinal peak can be seen in the lasing spectrum indicating that only one transverse mode is present in the VCSEL cavity. In addition, the two spectra in Figure 2.2.13 show that the lasing wavelength increases with bias current of the VCSEL.

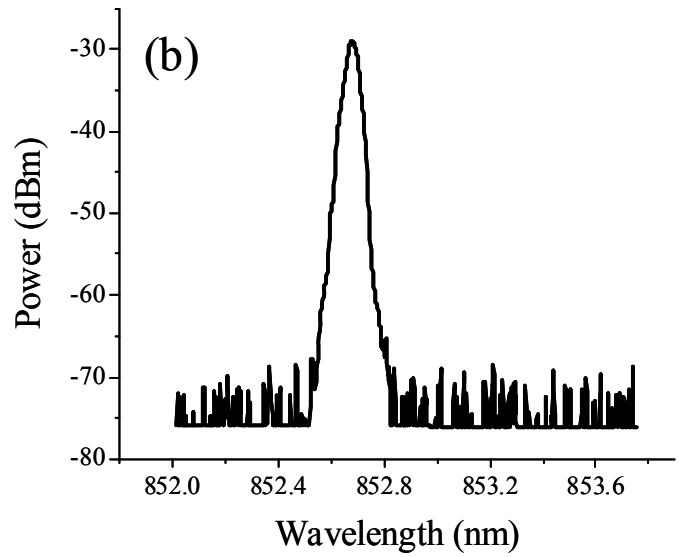
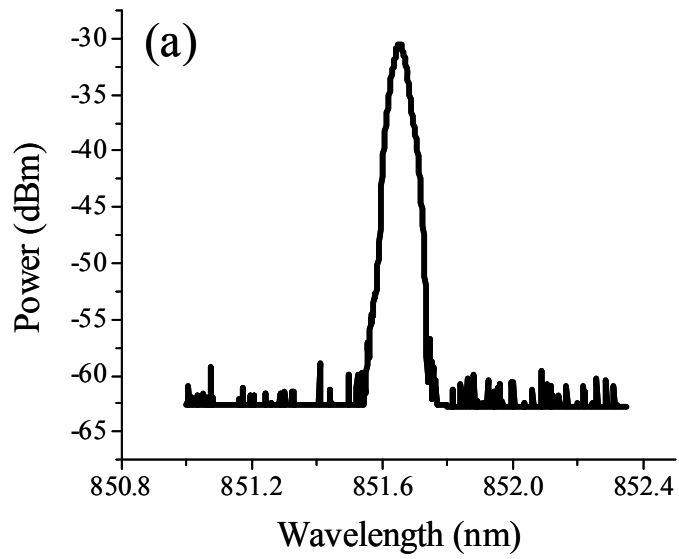


Figure 2.2.13: Lasing spectra for single mode oxide confined VCSEL at (a) 4mA (b) 6mA. Lasing wavelength increases with current.

Lasing spectra for an oxide confined multimode VCSEL at various bias currents is shown in Figure 2.2.14. At low bias currents, only a few transverse

modes are apparent, but as the current to the multimode laser is increased several more transverse modes can be seen. In addition, Figure 2.2.14 shows a shift in the VCSEL spectrum with an increase in current.

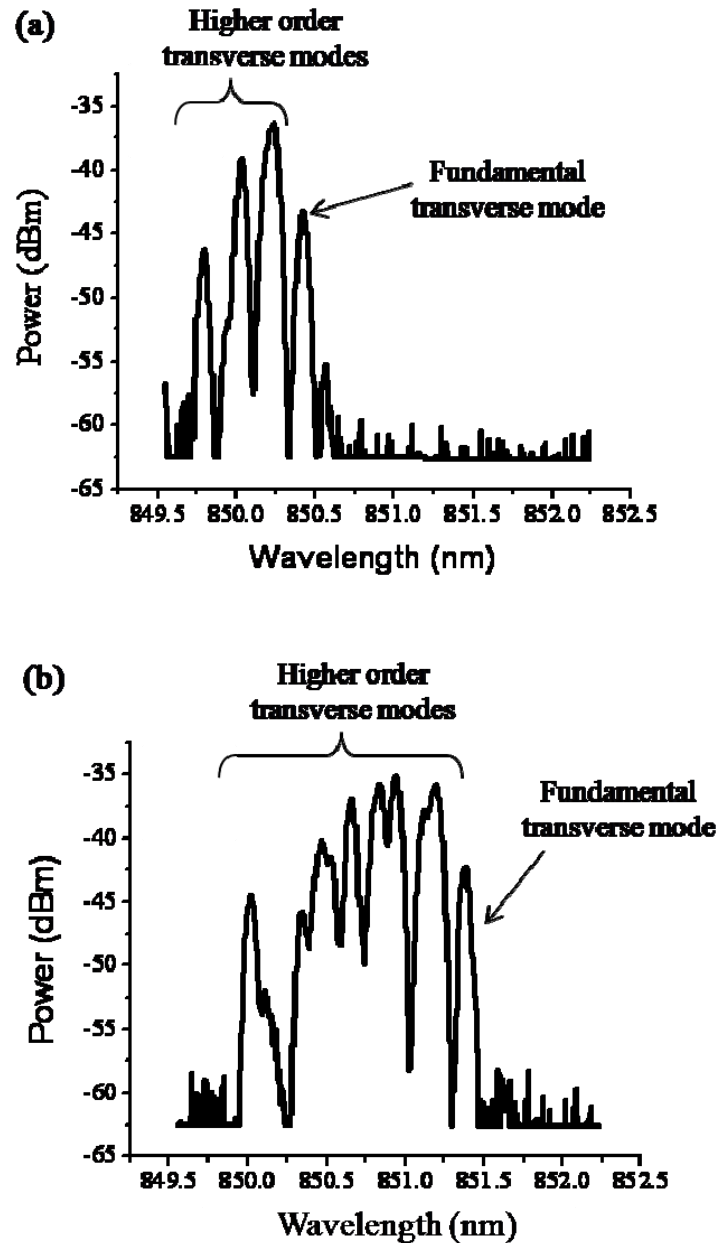


Figure 2.2.14: Lasing spectra for multimode oxide confined VCSEL at (a) 3mA (b) 10mA. Spectrum shifts to higher wavelengths with increasing current.

Overall, this section has provided many of the fundamentals necessary to understand how VCSELs work. This includes an overview of the basic VCSEL structure, a discussion of longitudinal and transverse modes in the laser cavity, details about specific elements that make up the VCSELs, and characteristics (LI curve, IV curve, and lasing spectrum) of different types of VCSELs. All of this information will be necessary to analyze the results presented in Chapters 4 and 5.

3. EXPERIMENTAL METHODS

3.1 Introduction

Many techniques have been developed to measure the thermal properties of materials and devices. While each of these techniques, which were discussed in Chapter 1, has advantages for specific applications, thermorefectance microscopy is the only one that can be used on light emitting surfaces such as a VCSEL aperture while providing high spatial and thermal resolutions. In addition to thermorefectance microscopy, we have also used the traditional method of low resolution, single point wavelength shift measurements to study bulk thermal effects in VCSELs, which will be discussed in greater detail in Chapters 4 and 5.

3.2 Wavelength Shift Technique

In order to validate our thermorefectance measurements, we compared them to results from the traditional methods of measuring bulk operating temperature by monitoring a shift in either the lasing wavelength or the emitted electroluminescence peak in the optical spectrum of the VCSEL. Wavelength shift measurements are non-contact, single point, bulk measurements with no spatial resolution. Monitoring a shift of the lasing wavelength provides the average cavity temperature, while measuring a shift in the emitted

electroluminescence provides the average change in temperature of the top mirror of the VCSEL, which will be discussed in greater detail in Chapter 4.

3.2.1 Single VCSELs:

Wavelength shift measurements on single VCSELs were performed using the experimental setup shown in Figure 3.2.1.

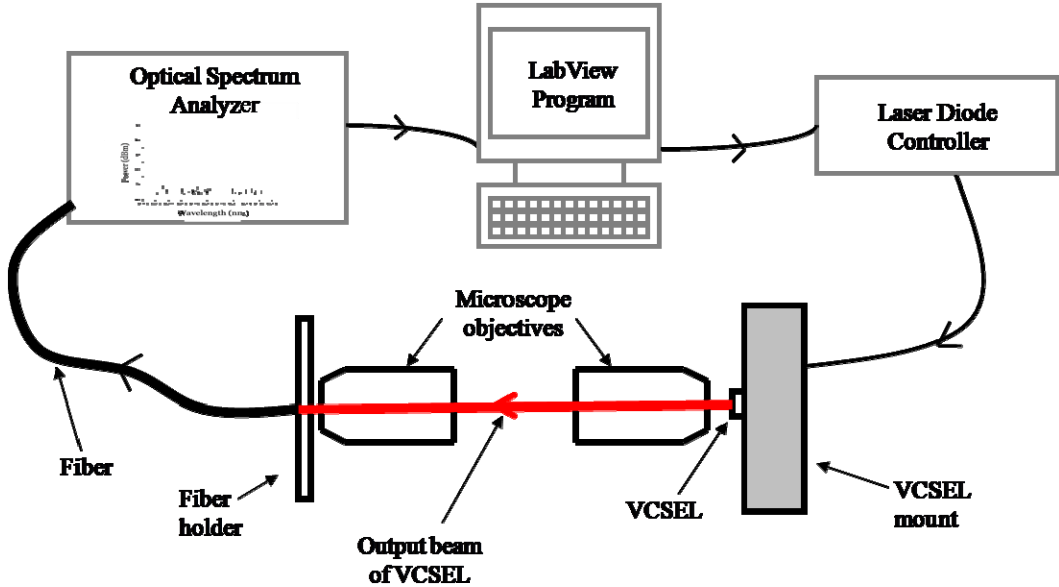


Figure 3.2.1: Experimental setup for single VCSEL wavelength shift measurements.

The first step in these measurements was to mount the VCSEL in a commercial laser diode mount (Model TCLDM9-TEC LD mount). The laser mount was connected to a laser diode controller (LDC-3900 Modular Laser Diode Controller) which was used to change the temperature and bias current of the laser. The glass window of the packaged VCSEL was removed in order to bring

the microscope objective as close as possible to the surface of the laser. Using a pair of microscope objectives, the output beam of the laser was collimated and focused into a multimode optical fiber with 62.5 μm inner diameter and 125 μm outer diameter. A micro-positioner was used to position the fiber so that the maximum amount of light from the laser was collected. During the alignment, the other end of the fiber was connected to a power meter (ILX Lightwave Fiber Optic Power Meter FPM-8200) so that the amount of light being focused into the fiber could be closely monitored. After careful alignment, the fiber was removed from the fiber optic power meter, cleaned, and connected to the optical spectrum analyzer (Agilent 86140B Optical Spectrum Analyzer). The optical spectrum analyzer was used to collect lasing spectrum for the VCSEL at various bias currents and temperatures. In addition to saving the optical spectrum on the computer, the Markers \rightarrow Peak Search function on the optical spectrum analyzer was used to monitor the shift in the emitted electroluminescence and lasing wavelength peaks for different bias currents and temperatures. Single VCSEL wavelength shift results will be discussed in detail in Chapter 4.

3.2.2 VCSEL Arrays:

Changes in the lasing wavelength of VCSEL arrays were also measured in order to determine the amount of thermal coupling between individual lasers in the array. The experimental setup for measuring the wavelength shift of

individual lasers in VCSEL arrays, which is very similar to that for single VCSELs, is shown in Figure 3.2.2.

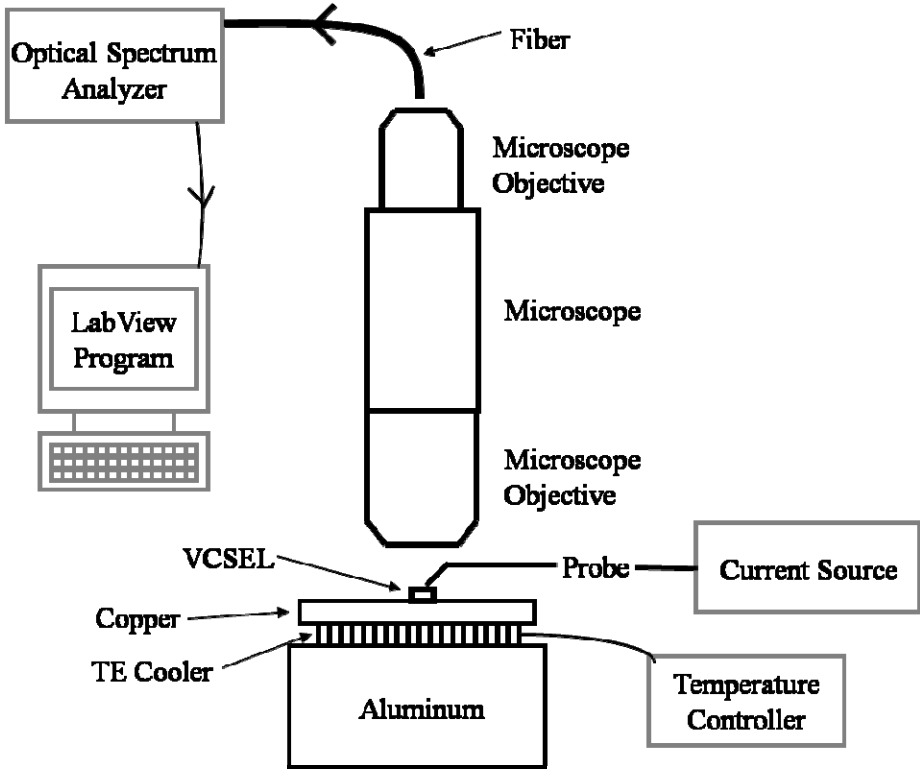


Figure 3.2.2: VCSEL array wavelength shift experimental setup.

Unlike our single VCSEL wavelength shift measurements that used tabletop optics, the VCSEL array wavelength shift experiments were performed using a microscope (Nikon Optiphot Optical microscope). Instead of directly mounting the laser in a commercial mount, the VCSEL array was soldered onto a piece of copper which was heat sunk to a large aluminum block using a Peltier thermoelectric cooler and thermal paste. The temperature of the copper heat sink was set using an ILX Temperature Controller (LDT-5525) and current was

supplied to the VCSELs by directly probing individual lasers in the array. The current was controlled using an ILX Current Source (LDX-3320). The output beam of the laser was focused, using the microscope optics, as well as an additional objective, into a multimode fiber. Optical spectra were obtained in the same way as for the single VCSEL and will be discussed in Chapter 5.

3.3 Thermoreflectance Microscopy

The primary thermal measurement technique that is used in this research is thermoreflectance microscopy, a non-contact, optical method of obtaining very high resolution two dimensional temperature maps. In this technique, a change in the reflectivity (ΔR) of a material's surface is used to measure a change in the temperature (ΔT). The reflectivity of a material depends on its refractive index n , which is slightly temperature-dependent. Hence, a change in the temperature of the VCSEL or VCSEL array causes a variation in its refractive index. It is this change in the refractive index which in turn causes a change in the reflectivity of the laser surface, given by Equation 3.1 where n_1 and n_2 are the refractive index of the air and surface material of the VCSEL respectively.

$$R = \left(\frac{n_1 - n_2}{n_1 + n_2} \right) \quad (3.1)$$

The change in surface temperature (ΔT) of a sample is related to the relative change in reflectivity ($\Delta R/R$) by a calibration coefficient κ as shown in Equation 3.2.

$$\frac{\Delta R}{R} = \frac{1}{R} \left(\frac{\partial R}{\partial T} \right) \Delta T = \kappa \Delta T \quad (3.2)$$

The calibration coefficient, typically with values between 10^{-6} K and 10^{-3} K, is both material and wavelength dependent [21]. Section 3.4 explains in greater detail how the thermorefectance calibration coefficients for both single VCSELs and VCSEL arrays were obtained.

Thermorefectance produces two dimensional thermal maps of a surface by imaging $\Delta R/R$ across the sample, from which ΔT can be extracted if κ , the calibration coefficient, is known. Thermorefectance microscopy, unlike wavelength shift measurements, provides both high thermal resolution (10mK) and high spatial resolution (250nm). High spatial resolution is important when working with VCSELs so that temperature distributions across their small apertures ($\sim 10\mu\text{m}$) can be measured to investigate large temperature gradients that are responsible for thermal lensing. High thermal resolution allows for the measurement of small changes in temperature, which is particularly important when measuring the thermal coupling between individual lasers widely spaced in VCSEL arrays. In addition to providing high resolution, thermorefectance microscopy is a non-contact technique that can be used on light emitting surfaces such as VCSELs, which is not the case with some other temperature techniques mentioned in Chapter 1, such as scanning thermal microscopy [2].

Thermorefectance microscopy produces 2-D thermal images of the surface of the VCSEL using a CCD camera (Opteon CCD Camera; 60 frames/second; 652x494 pixels) and an optical microscope. This technique was

used to measure the temperature distribution across the surface of a single VCSEL for different bias currents and to measure the thermal coupling between multiple VCSELs in a VCSEL array, which will be discussed in greater detail in Chapters 4 and 5. The experimental setup for both the single VCSEL and VCSEL array thermoreflectance measurements is shown in Figure 3.3.1.

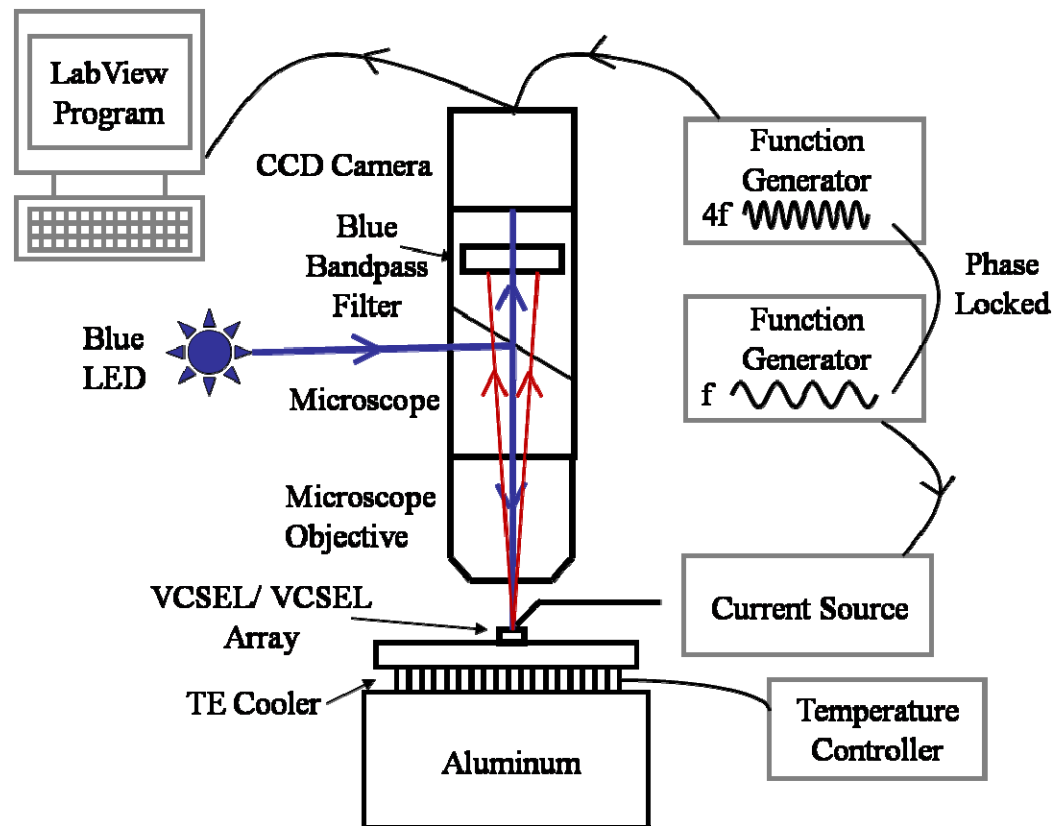


Figure 3.3.1: Thermoreflectance Experimental Setup.

In this setup, the VCSEL or VCSEL array is mounted on a piece of copper which is placed on top of a thermoelectric (TE) cooler, which provides active temperature control of the copper block. The TE cooler is heat sunk to a large

aluminum block so that even as the VCSEL warms up during operation, the bottom side of the laser will be held at a fixed temperature ($T = 20^{\circ}\text{C}$). Current is supplied to the laser using an ILX laser diode current source that is modulated using a function generator at a fixed frequency f . Another function generator modulated at $4f$ is phase locked to the first and used to trigger the CCD camera, which leads to an effective pixel-by-pixel lock-in technique described below.

As discussed earlier, the modulation of the current will cause a temperature dependent change in the reflectivity of the VCSEL. In order to measure this change, a blue LED is used to uniformly illuminate the surface of the laser and the reflected light is imaged through an optical microscope onto a CCD camera. The red light emitted from the VCSEL is blocked from the CCD camera using a blue band pass optical filter.

Since the signal we are looking for is very small compared to the noise, lock-in amplification is used to extract the signal. Since our detector is a 652×494 array, we use signal processing techniques, described here, to perform effective pixel-by-pixel lock-in amplification. To do this, we trigger the camera at four times the frequency of the temperature modulation of the VCSEL, so that during each period of the modulation of the sample reflectivity R , a pixel of the CCD records a succession of four images, as shown in Figure 3.3.2.

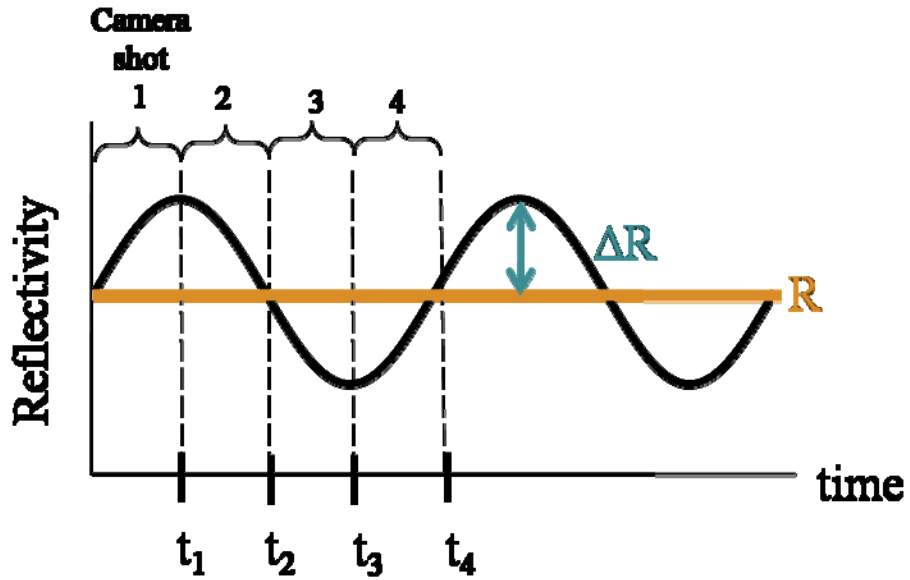


Figure 3.3.2: Reflectivity versus time for one pixel of VCSEL thermoreflectance image, showing the four snapshots taken per period of the wave.

During each of the four time intervals per modulation period that the camera shutter is open, a pixel essentially integrates the reflectivity curve over one quarter of the wave, as shown in Figure 3.3.3, so that the following four images are collected for each pixel:

$$I_1 = \int_0^{t_1} (\Delta R \sin(\omega t) + R) dt$$

$$I_2 = \int_{t_1}^{t_2} (\Delta R \sin(\omega t) + R) dt \quad (3.3)$$

$$I_3 = \int_{t_2}^{t_3} (\Delta R \sin(\omega t) + R) dt$$

$$I_4 = \int_{t_3}^{t_4} (\Delta R \sin(\omega t) + R) dt$$

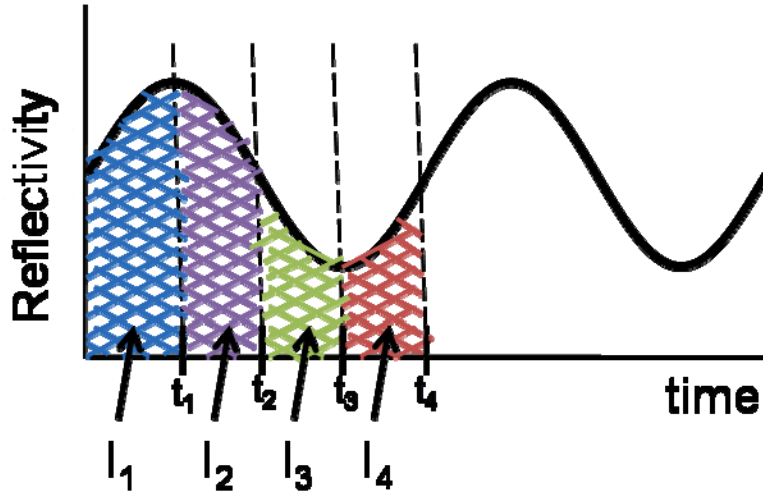


Figure 3.3.3: Four images calculated by integrating under the reflectivity curve between subsequent snapshots.

In order to extract a small $\Delta R/R$ signal in the presence of noise, thermoreflectance experiments typically run for several thousand to several hundreds of thousands of iterations. We define four “buckets” B_i , where each bucket is the sum of all of the integrals for that quarter of the wave over many periods:

$$B_i = \sum_{j=1}^N I_i(j) \quad (3.4)$$

N is equal to the number of iterations, $i \in \{1,2,3,4\}$, and $I_i(j) = I_i$ during the j^{th} iteration. After determining the total value of the four buckets for each pixel in

the image, the amplitude ($\Delta R/R$) and relative phase (φ) of our signal can be calculated from Equations 3.5 and 3.6 [21].

$$\left| \frac{\Delta R}{R} \right|_{\text{ideal}} = \frac{\pi \sqrt{(B_1 - B_3)^2 + (B_2 - B_4)^2}}{2(B_1 + B_2 + B_3 + B_4)} \quad (3.5)$$

$$\varphi = \arctan\left(\frac{B_1 - B_2 - B_3 + B_4}{B_1 + B_2 - B_3 - B_4}\right) \quad (3.6)$$

It is this measured change in the relative reflectivity along with the calibration coefficient, experimentally found in the next section, which allows us to calculate the changes in temperature of the VCSELs and VCSEL arrays under investigation in Chapters 4 and 5. For clarity, we emphasize that this four bucket technique is implemented independently for each individual pixel in the camera. Since each pixel images a different location on the sample surface, the net result is a two dimensional map of $\Delta R/R$ across our surface, from which we can extract a thermal image of the sample, providing that the calibration coefficient is known.

3.4 Thermoreflectance Calibration Coefficient

In order to extract the change in temperature ΔT from the relative change in reflectivity $\Delta R/R$ (see Equation 3.2), a calibration coefficient κ was measured for both the single VCSEL and VCSEL array.

3.4.1 Single VCSELs:

To determine the calibration coefficient for a single VCSEL, the experimental setup shown in Figure 3.4.1 (a) was used.

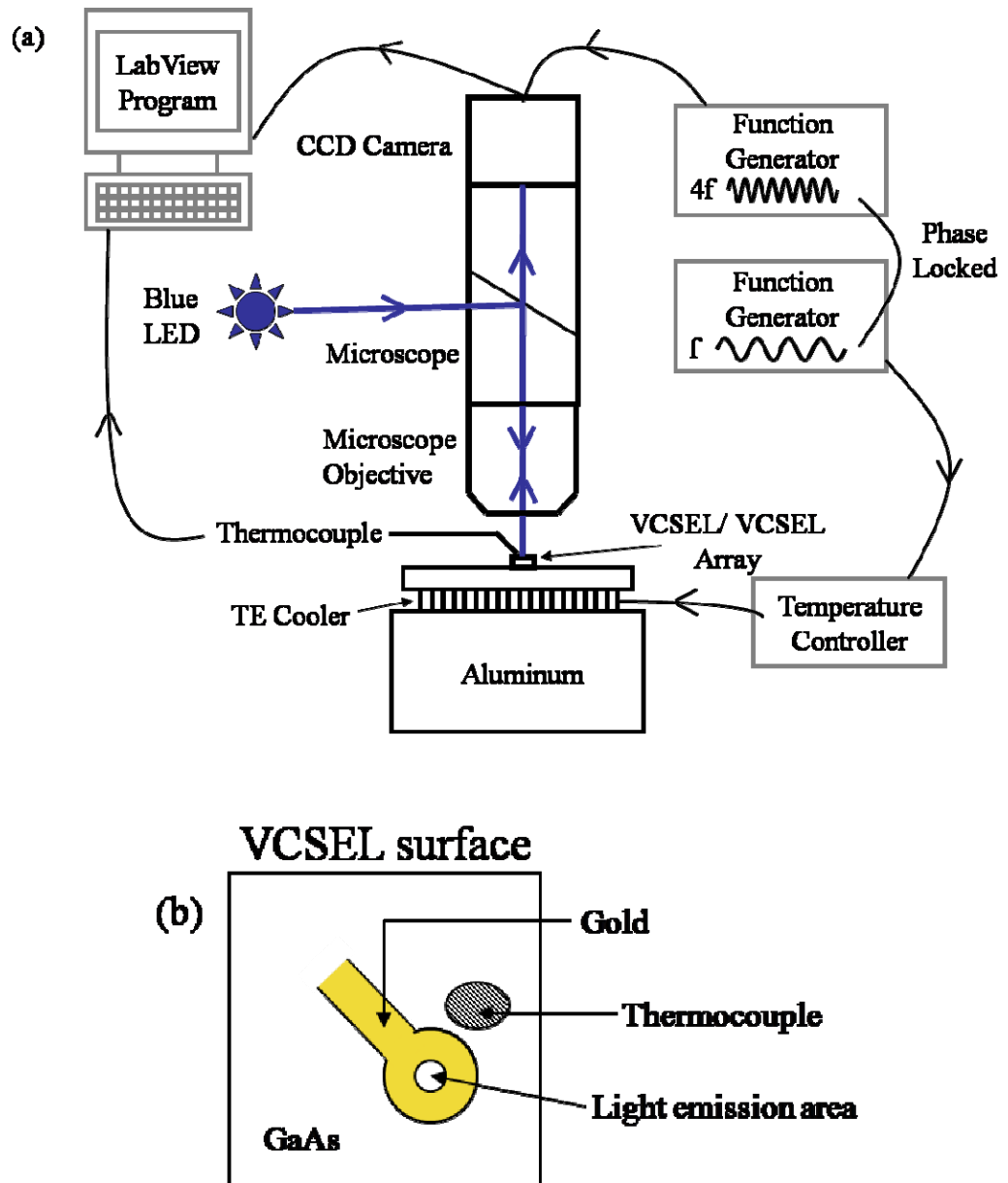


Figure 3.4.1: (a) Thermoreflectance calibration coefficient experimental setup (b) Placement of thermocouple on VCSEL surface.

In this experiment, the temperature of the VCSEL is driven sinusoidally at 250mHz, while the CCD camera is triggered at 1Hz. The temperature of the TE cooler was modulated and no current was supplied to the VCSEL. By modulating the temperature of the VCSEL, we are able to measure a change in the reflectivity using the thermorefectance technique described in Section 3.3. During the same experiment, the surface temperature is measured independently using a micro-thermocouple that is placed near the aperture of the VCSEL, as shown in Figure 3.4.1 (b). The micro-thermocouple directly measures the temperature of an area very close to the laser aperture where light is emitted. Even though we are measuring the calibration coefficient for the aperture of the laser, the thermocouple can not be placed on the aperture of the VCSEL for two reasons. Firstly, the thermocouple is too large ($\sim 25\mu\text{m}$ in diameter) to be placed on the VCSEL aperture ($\sim 10\mu\text{m}$). Secondly, thermocouples can not be used on light emitting surfaces, as previously discussed in Chapter 1, because they absorb the light emitted from a laser, leading to inaccurate temperature readings.

From the calibration coefficient experiment described above, the relative change in reflectivity ($\Delta R/R$) and change in temperature (ΔT) of the VCSEL surface were measured using the CCD camera and thermocouple respectively, as shown in Figure 3.4.2 (a) and (b).

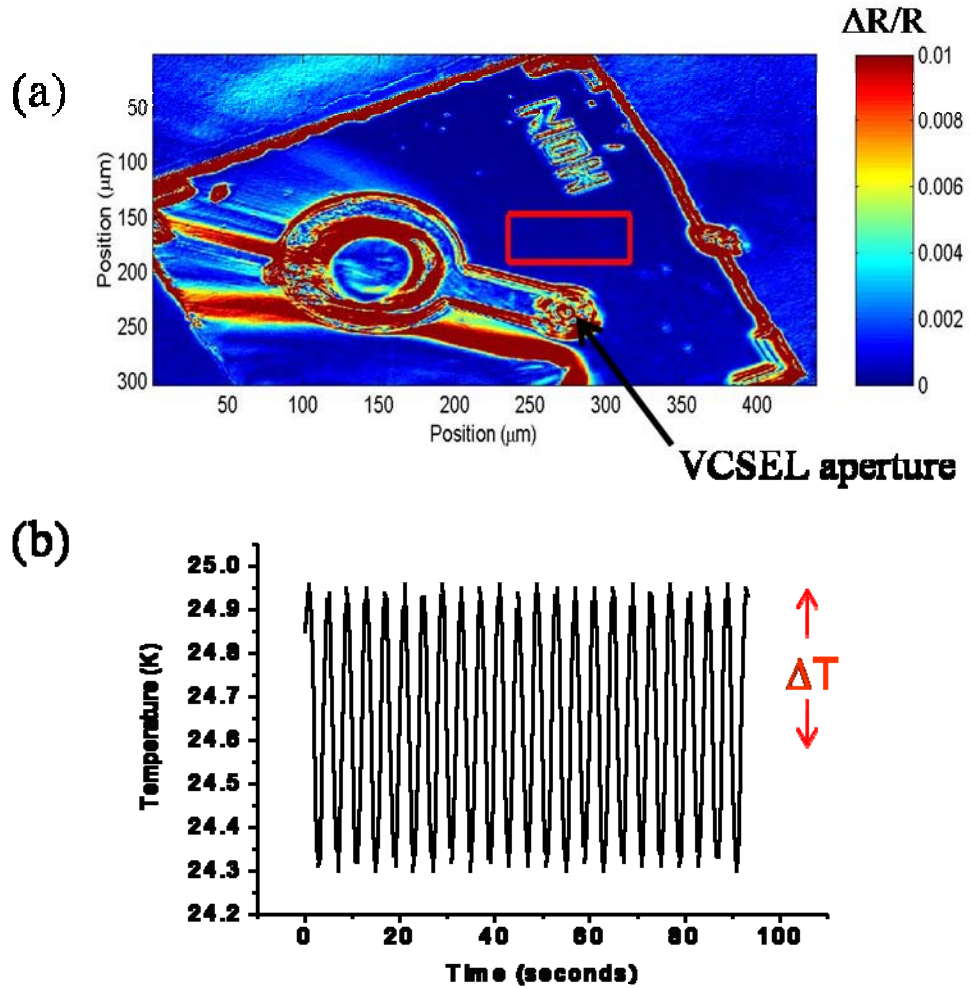


Figure 3.4.2: (a) $\Delta R/R$ thermoreflectance image (b) Change in temperature (ΔT) measured using micro-thermocouple.

The calibration coefficient for the aperture of the VCSEL was calculated using Equation 3.2 and found to be $\kappa = 2.3 \times 10^{-4} \text{ K}^{-1}$. This number is in good agreement with the literature [22], however there still remains some question as to whether our assumption that the material near the VCSEL aperture is the same as the material inside the aperture is true [11]. In this research, we assumed that the material was the same and therefore found the calibration coefficient for the

material near the aperture. We used this calibration coefficient to convert the values for the change in reflectivity of the aperture of the VCSEL to changes in temperature.

3.4.2 VCSEL Arrays:

A different technique was used to determine the calibration coefficient for the aperture of the VCSELs in the array. The technique was changed from that of the single VCSEL in order to eliminate the uncertainty of whether the calibration coefficient was being calculated for the aperture or the nearby material. The experimental setup for the determination of the VCSEL array calibration coefficient is the same as that used for the actual thermorefectance measurements, Figure 3.3.1. An image of the VCSEL array is shown in Figure 3.4.3.

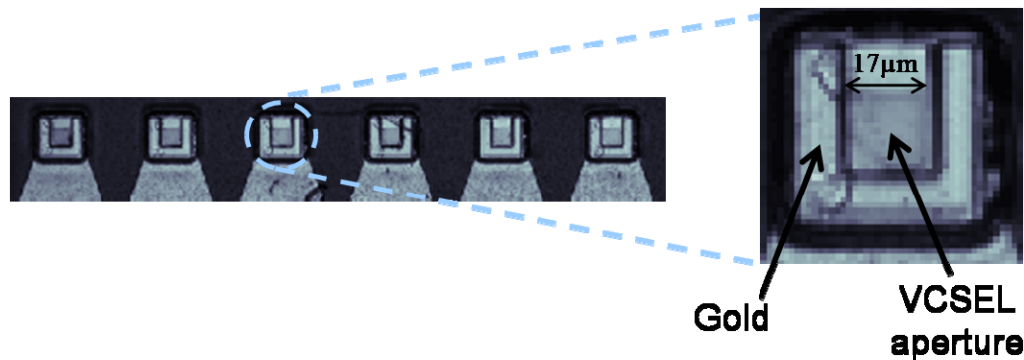


Figure 3.4.3: VCSEL array image showing laser aperture and gold contact surrounding aperture.

Unlike the case of the single VCSEL calibration experiment where the temperature is varied using a thermoelectric cooler, in the calibration experiment for the VCSEL array, the heat sink temperature is kept constant (20°C) while the current of one of the lasers, VCSEL #4, (see the thermal coupling discussion in Chapter 5) is modulated to provide a variation in the temperature of the neighboring VCSEL. The adjacent, unbiased VCSELS in the array are the ones used for the actual calculation of the calibration coefficient.

A thermoreflectance experiment was performed at a camera frequency of 60Hz and current modulation frequency of 15Hz for 800,000 iterations. The temperature controller was set to 20 °C to keep the substrate temperature of the VCSEL array constant. The change in surface temperature was calculated at the gold contacts on either side of the adjacent laser's aperture, as shown in Figure 3.4.4, using the relative change in reflectivity from the thermoreflectance experiment and the known calibration coefficient for gold ($\kappa = 4.0 \times 10^{-4} \text{ K}^{-1}$) [12]. These values are listed in Table 3.1.

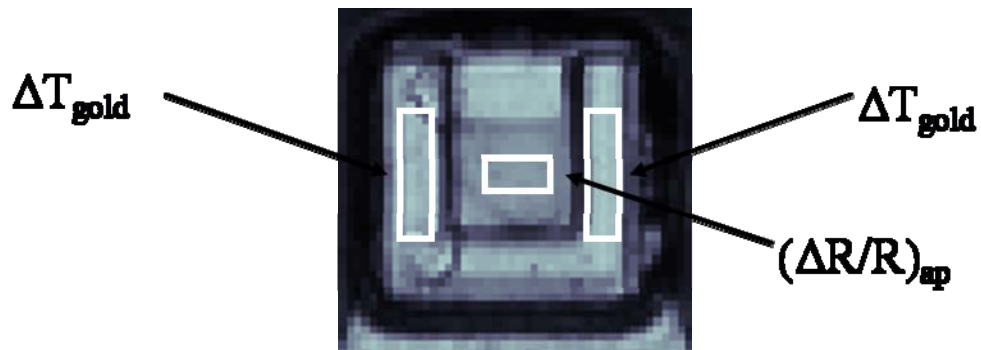


Figure 3.4.4: Enlarged image of adjacent VCSEL and areas where ΔT and $\Delta R/R$ were calculated.

From the changes in temperature (ΔT) on either side of the aperture it was assumed that the change in temperature in the center of the aperture of the VCSEL would be the average of the ΔT s for gold on either side. We believe that this assumption is valid due to the heat spreading out radially across the array from the modulated VCSEL. (The results in Chapter 5 discuss this thermal coupling behavior in detail). Using the data acquired from the thermoreflectance experiment, we were also able to determine the $\Delta R/R$ for the center of the aperture. Using this technique and Equation 3.2, the calibration coefficient for VCSEL #5 was found to be $\kappa = 2.05 \times 10^{-4} \text{ K}^{-1}$. This was done for several of the closest neighboring lasers to the modulated VCSEL (VCSEL #4) and the calculated calibration coefficients are given in Table 3.1.

VCSEL Number	ΔT on left side of aperture	ΔT on right side of aperture	$\Delta R/R$ in aperture	Calibration Coefficient (κ)
2	0.15 K	0.18 K	2.98×10^{-5}	$1.8 \times 10^{-4} \text{ K}^{-1}$
3	0.26 K	0.29 K	5.50×10^{-5}	$1.98 \times 10^{-4} \text{ K}^{-1}$
5	0.29 K	0.28 K	5.93×10^{-5}	$2.05 \times 10^{-4} \text{ K}^{-1}$

Table 3.1: Experimentally determined changes in temperature (ΔT) of the gold on each side of the laser aperture, changes in reflectivity ($\Delta R/R$) inside the aperture, and calibration coefficients for individual laser apertures in the VCSEL array. VCSEL #4 is probed and modulated.

The calibration coefficient used for all of the VCSEL array thermoreflectance experiments, which will be discussed in Chapter 5, was estimated by averaging the three calibration coefficients given in Table 3.1, $\kappa = 1.94 \times 10^{-4} \text{ K}^{-1}$ [23].

4. RESULTS: HIGH RESOLUTION THERMAL IMAGING OF A SINGLE VCSEL

4.1 Introduction

This chapter describes the experimental results obtained for individual vertical cavity surface emitting lasers. We are interested in studying the thermal behavior of three different types of VCSELs using both wavelength shift and thermorefectance microscopy techniques. As mentioned in Chapter 2, while all VCSELs have the same basic structure, there are several modifications to this basic design that can be used to tailor the electrical and optical characteristics of VCSELs. In this research, we focus on three specific types of VCSELs: oxide confined single mode, oxide confined multi-mode, and proton implanted multi-mode. All three types of VCSELs are manufactured by Advanced Optical Components, fabricated in a GaAs-based materials system, and have an output lasing wavelength of ~850nm.

One of the main goals of the research in this chapter is to understand the effect the structure of the VCSEL has on its temperature distribution. As mentioned in Chapter 1, understanding the temperature distribution throughout the laser structure is important in developing more efficient devices. Section 4.2 provides the general laser characteristics of the single VCSELs used in this research. In Section 4.3, we compare the temperature results obtained using the

standard lasing wavelength shift technique for three types of VCSELs. In section 4.4, we compare the temperature results obtained using the lasing wavelength and emitted electroluminescence wavelength shift for an oxide confined single mode VCSEL.

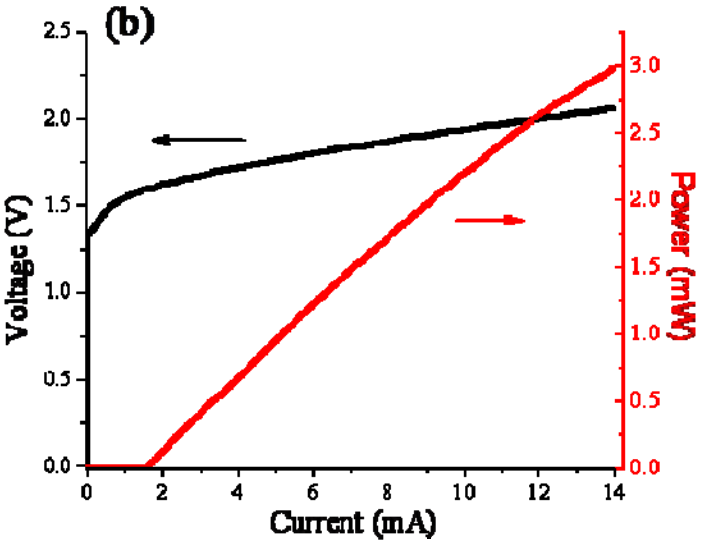
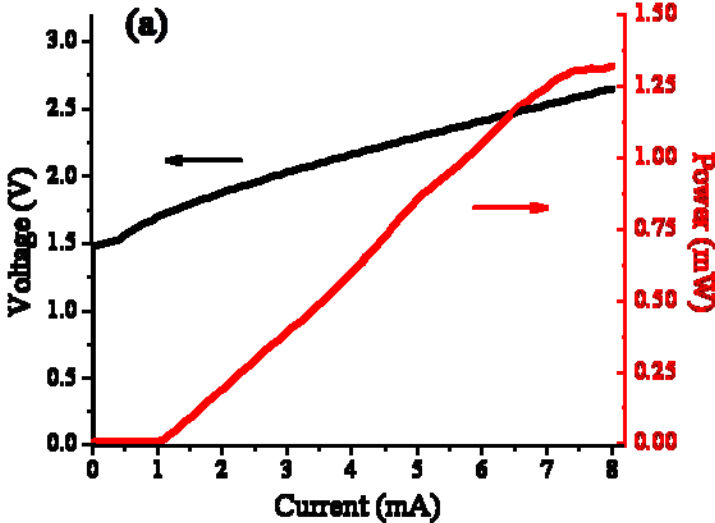
In addition to the conventional bulk temperature measurements discussed in Sections 4.3 and 4.4, we use thermoreflectance microscopy to perform two dimensional, spatially resolved, non-destructive profiling of the surface temperature in these three lasers under operating conditions. Section 4.5 compares the thermoreflectance results obtained for the three different types of VCSELs. These high resolution measurements provide detailed temperature mappings of the VCSEL's apertures at different operating conditions.

Finally, the thermoreflectance microscopy results are compared to the traditional method of using wavelength shift to determine the temperature, in the case of the oxide confined single mode VCSEL. This part of the research is aimed at understanding how the different temperature measurements compare for a vertical cavity surface emitting laser.

4.2 VCSEL Characteristics

Optical output power versus current plots (LI curves) and voltage versus current (IV curves) for the oxide confined single mode, oxide confined multi-mode, and proton implanted multi-mode VCSELs are shown in Figure 4.2.1 (a), (b), and (c), respectively. As mentioned in Chapter 2, the threshold current is the

current where the gain equals the optical loss in the laser cavity and the point at which lasing begins. The threshold currents for oxide confined single mode, oxide confined multi-mode, and proton implanted multi-mode VCSELs presented here are 1.10mA, 1.56mA, and 3.36mA respectively.



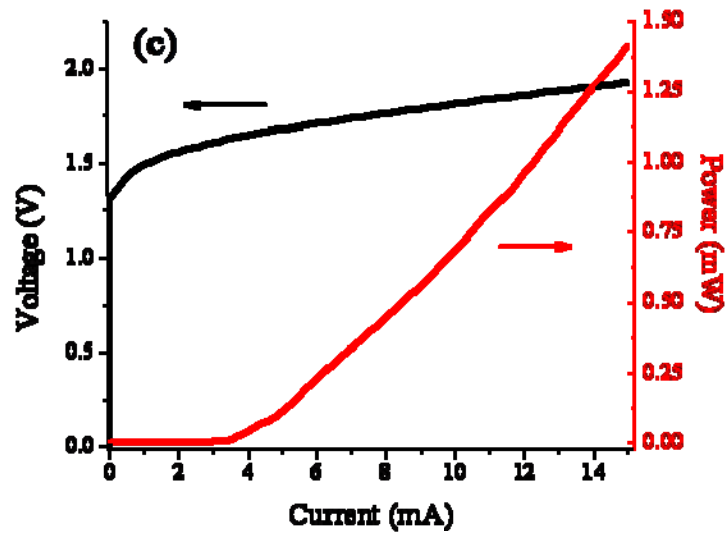


Figure 4.2.1: LI and IV curves for a typical (a) oxide confined single mode VCSEL (b) oxide confined multi-mode VCSEL and (c) proton implanted multi-mode VCSEL.

4.3 Wavelength Shift Measurement: Lasing Wavelength Shift

4.3.1 Wavelength Shift with Temperature:

The first technique used to measure the temperature of the VCSELs involved monitoring a shift in the lasing wavelength as the temperature of the VCSEL was varied. To measure this wavelength shift, the setup described in Chapter 3 was used for each of the three lasers. In this set of experiments, the current of the VCSEL was set at a fixed value and the operating temperature of the VCSEL was changed by varying the temperature of the heat sink, on which

the VCSEL sits, between 20°C and 68°C. The actual operating temperature of the VCSEL is unknown but is certainly greater than the heat sink temperature. However, in this experiment we are only interested in the change in temperature and to the first order we expect that a change in the heat sink temperature should result in a similar change in the operating temperature. At each temperature, the emission spectra and lasing wavelength peaks were recorded on the computer. Figure 4.3.1 shows a plot of the lasing wavelength versus temperature for the three types of VCSELs. The slope of the linear fit ($d\lambda/dT$) for the data is the temperature calibration coefficient. In the case of the oxide confined single mode, oxide confined multi-mode, and proton implanted multi-mode VCSELs these values are 0.04nm/°C, 0.06nm/°C, and 0.05nm/°C.

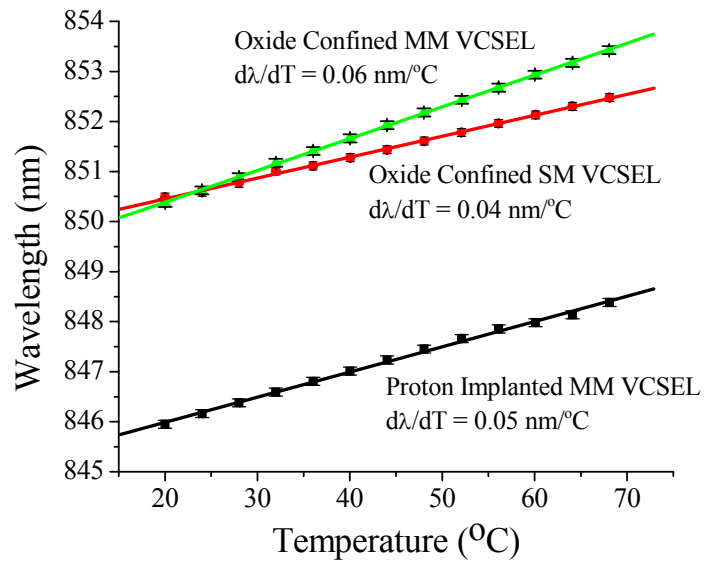


Figure 4.3.1: Lasing wavelength versus temperature for three types of VCSELs.

This shift in the lasing wavelength with temperature is due to the variation in the wavelength of the longitudinal mode. A change in the operating temperature causes a variation in the refractive index of the laser material and hence in the effective length of the cavity. The frequency at which the VCSEL lases depends on the cavity length, and therefore a change in temperature results in a shift in the lasing peak of the VCSEL spectrum. Because the photons move back and forth between the DBR mirrors and through the active region hundreds of times before exiting the laser, the lasing wavelength provides an average temperature for the VCSEL cavity.

4.3.2 Wavelength Shift with Current:

One way of changing the temperature of the VCSELs is by applying a current to them in order to make them lase. Similar to the technique in the previous section, we monitor a shift in the lasing wavelength as we vary the current to the VCSEL. In all of these measurements, the thermoelectric cooler was set to 20.0°C and the current varied between the threshold current and rollover current for the VCSEL. As the current to the laser was increased, the temperature of the VCSEL also increased, and the lasing wavelength shifted to the right. This shift in wavelength with increasing current occurred in each of the three types of VCSELs, one of which (oxide confined single mode VCSEL) is shown in Figure 4.3.2.

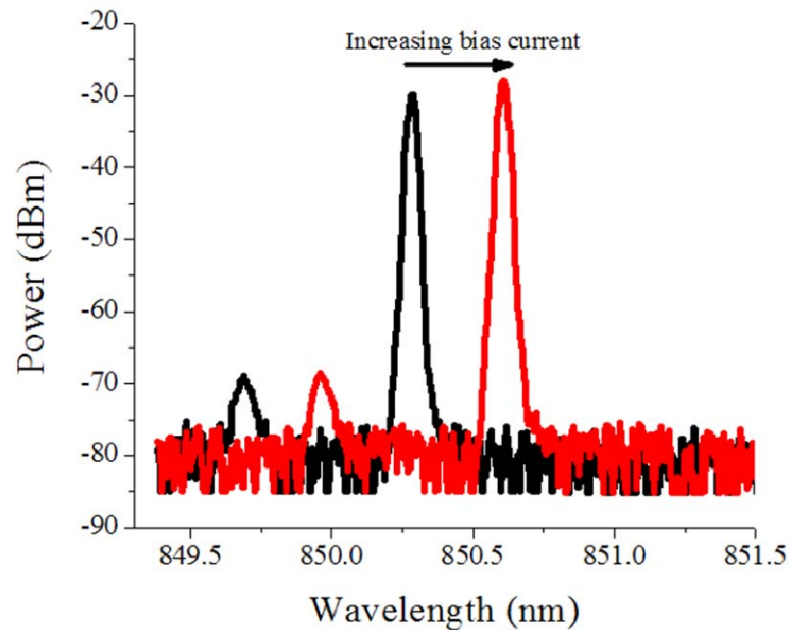


Figure 4.3.2: Shift in lasing spectrum with increasing current for oxide confined single mode VCSEL.

In the oxide confined and proton implanted multi-mode VCSELs, as the current to the lasers was increased, additional transverse modes began to appear, see Figure 2.2.14. In order to monitor the change in the lasing wavelength, the shift in the peak with the greatest intensity was measured. For each of the three types of VCSELs, a linear ($d\lambda/dI$) relationship was found between the lasing wavelength and the bias current to the laser, as plotted in Figure 4.3.3. The difference in the slopes of the three different types of VCSELs shows that for the same change in current, the oxide confined single mode VCSEL has a greater change in the lasing wavelength than both the oxide confined and proton implanted multi-mode VCSELs. Discussed more in Section 4.3.3, this greater

shift in the lasing wavelength for the oxide confined single mode VCSEL can be related to a larger change in temperature of the device due to its smaller size.

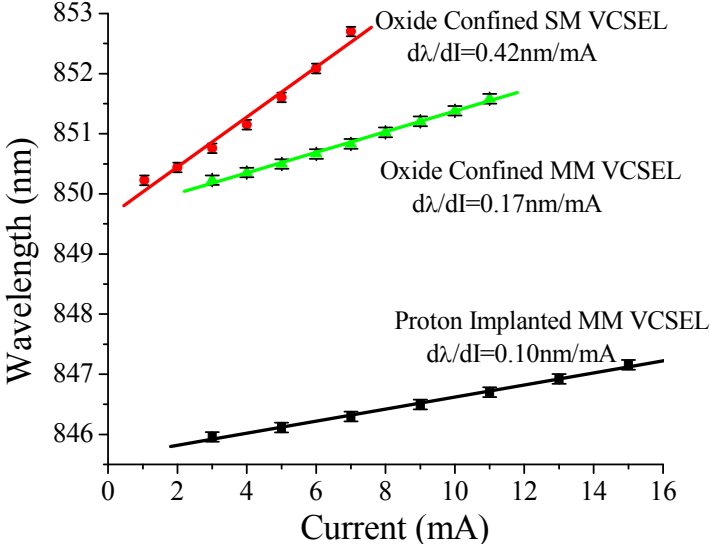


Figure 4.3.3: Plot of lasing wavelength versus current for three types of VCSELs.

4.3.3 Temperature versus Current:

A change in temperature can be obtained as a function of the bias current, Equation 4.1, using the slopes of the wavelength versus current ($d\lambda/dI$) and wavelength versus temperature ($d\lambda/dT$) data for each VCSEL.

$$\left(\frac{d\lambda}{dI}\right)\left(\frac{d\lambda}{dT}\right)^{-1} = \frac{dT}{dI} \tag{4.1}$$

Using the slopes of the fitted curves from Figures 4.3.1 and 4.3.3, we are able to show a linear relationship between temperature and dissipated power for the three types of VCSELs, as shown in Figure 4.3.4. The dissipated power was calculated

by multiplying the current applied to the VCSEL by the voltage across the laser and subtracting the output power:

$$\Delta P = IV - P_{rad} \tag{4.2}$$

The slope of linear fit for the oxide confined single mode VCSEL is larger than that for both of the multi-mode lasers and is attributed to a smaller aperture size for the single mode VCSEL (~5µm). The apertures for the oxide confined and proton implanted multi-mode VCSELs are ~17µm and ~15 µm respectively. The smaller aperture of the oxide confined single mode VCSEL means that for a given electrical power there is a greater current density inside the laser. In other words, more current is being forced through a narrower pathway in the case of the single mode VCSEL, leading to a greater change in temperature.

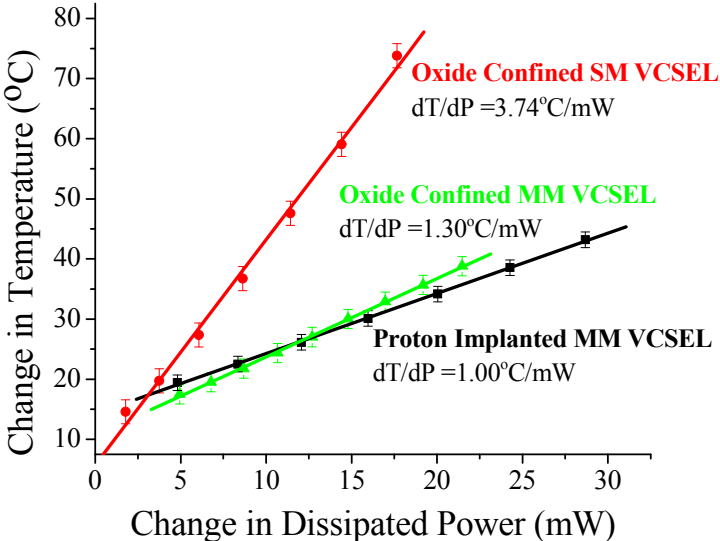


Figure 4.3.4: Change in temperature measured monitoring a shift in the lasing wavelength versus change in dissipated power for three types of VCSELs.

4.4 Wavelength Shift Measurement: Emitted Electroluminescence

From this point forward in the single VCSEL results, the same three lasers were used (one oxide confined single mode VCSEL, one oxide confined multi-mode VCSEL, and one proton implanted multi-mode VCSEL). The following research was also published in the *IEEE Photonics and Technology Letters* in 2007 [14].

It is important to note that the two wavelength shift techniques (lasing and emitted electroluminescence) measure two different temperatures. Emitted electroluminescence, unlike the lasing emission, allows us to measure the temperature of the top DBR mirror of the VCSEL. As shown previously in Figure 2.2.12, the spontaneous emission of a VCSEL is a very broad peak spanning tens of nanometers. However, the reflectivity spectrum of the DBR mirrors, shown in Figure 4.4.1, has a decrease in reflectivity (increase in transmission) at only a small fraction of the spontaneous emission wavelengths of the VCSEL. Therefore, the photons measured by monitoring a shift in the emitted electroluminescence are a small portion of those that make up the spontaneous emission. In addition, they have a wavelength where the reflectivity of the DBR mirrors is at a minimum and goes to almost zero (transmission at a maximum), see Figure 4.4.1.

As the operating temperature of the VCSEL changes, the reflectivity spectrum of the DBR mirrors also shifts due to a change in the effective thickness of the mirror layers as the refractive index varies with temperature. This change in the reflectivity spectrum in turn causes the wavelength of the transmission window through the top DBR mirror to vary, resulting in a measurable shift in the wavelength of the emitted electroluminescence to greater wavelengths for increasing temperatures.

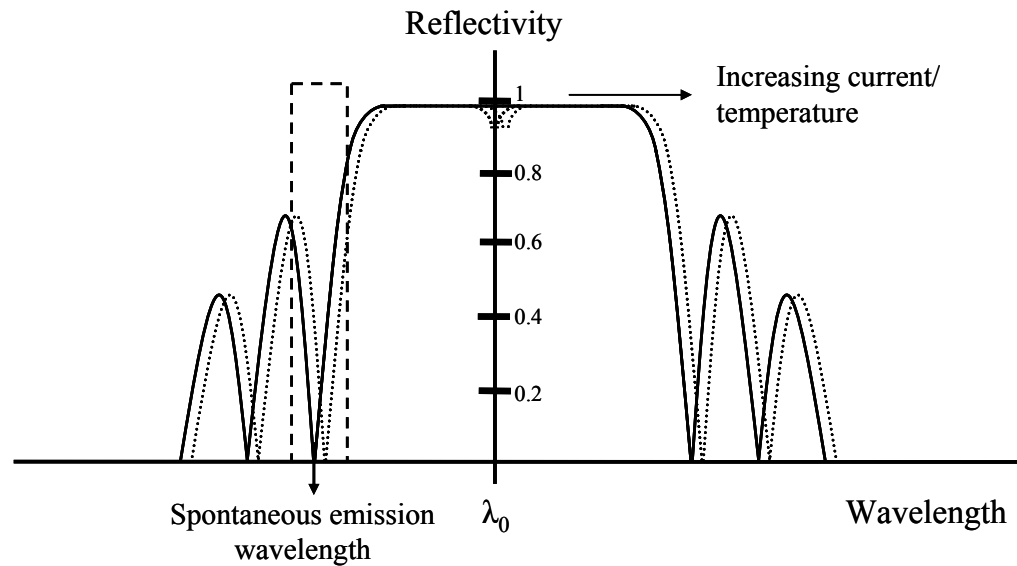


Figure 4.4.1: Schematic of top mirror reflectivity spectrum showing transmission window through which emitted electroluminescence is visible.

For the oxide confined single mode VCSEL, sufficient coupling of the output beam into an optical fiber was obtained to monitor a shift in the peak wavelength of the emitted electroluminescence. The same experimental setup, Figure 3.2.1, was used as before to collect wavelength spectra. From the emission spectra, the shift in the peak electroluminescence wavelength was traced and

plotted as a function of current and temperature, enabling us to extract the change in temperature versus change in current as in Section 4.3. This data was used to produce a plot of the change in temperature versus change in dissipated power for the VCSEL, as shown in Figure 4.4.2.

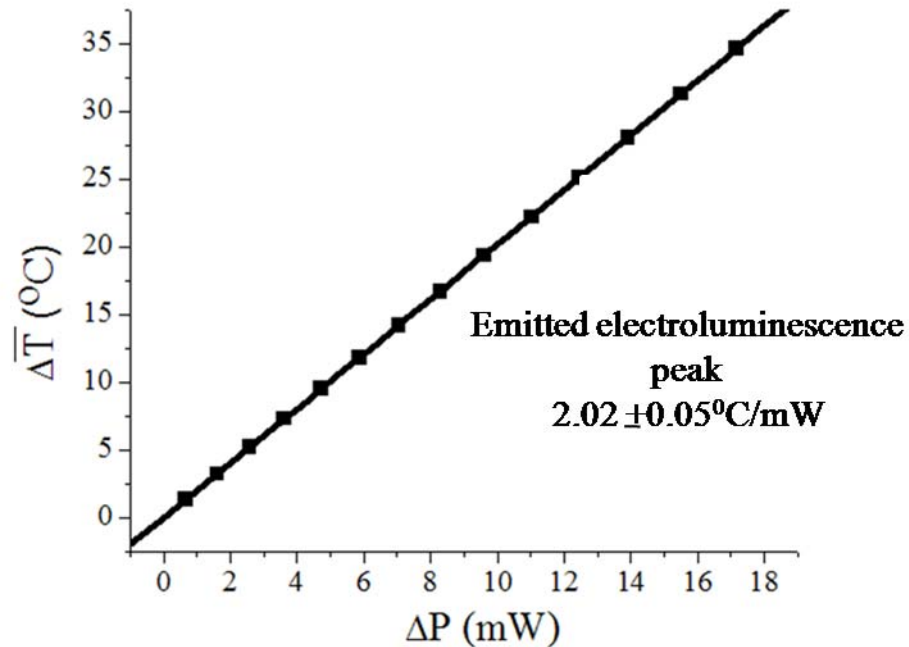


Figure 4.4.2: Plot of temperature versus dissipated power using emitted electroluminescence wavelength shift technique.

In the case of the oxide confined single mode VCSEL, the change in temperature with dissipated power of the device measured using a shift in the lasing wavelength was greater than that measured using a shift in the emitted electroluminescence. Therefore, we conclude that the average change in temperature of the cavity is greater than that of the overall change in temperature of the top mirror of the VCSEL, as shown in Figure 4.4.3.

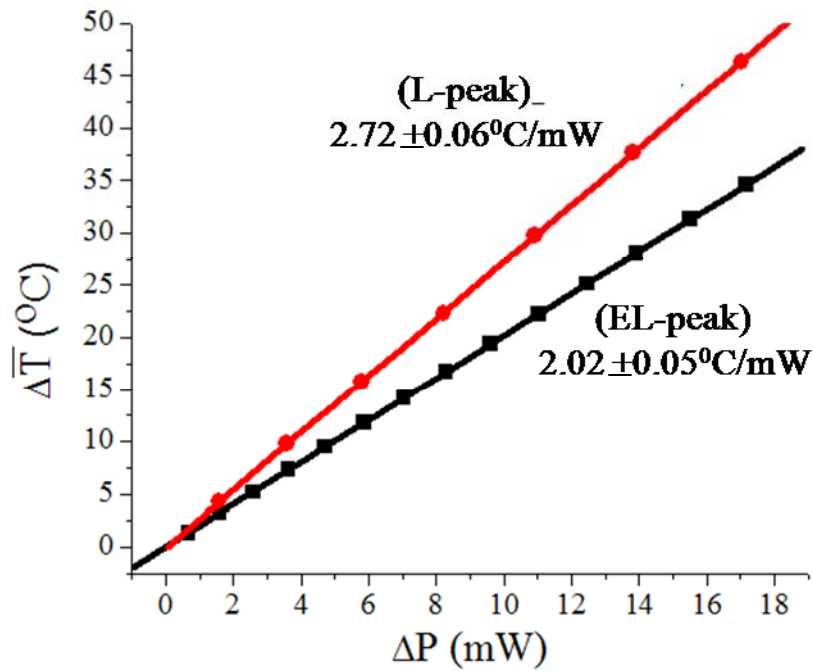


Figure 4.4.3: Comparison of lasing wavelength shift (L-peak) and emitted electroluminescence wavelength shift (EL-peak) temperature measurement techniques.

These results are consistent with previous publications [2]. Specifically, as discussed in Chapter 1, scanning thermal microscopy of a VCSEL revealed a greater change in temperature for the laser cavity than for the top mirror of the device [2]. While scanning thermal microscopy provided similar results, wavelength shift measurements are non-contact and do not require damaging the VCSEL in any way to obtain temperature profiles of the various layers. In the next section, we will compare the temperatures measured with the wavelength shift techniques to those obtained using thermoreflectance microscopy.

4.5 Thermoreflectance Microscopy

In addition to wavelength shift measurements for each of the three different types of single VCSELs, high resolution thermoreflectance microscopy measurements were also taken. This technique, described at greater length in Chapter 3, provides surface temperature distribution profiles across the surface of the VCSEL. The purpose of using thermoreflectance microscopy in this research is to investigate spatial variations in the surface temperatures for the three different types of lasers as well as to compare the surface temperature with the average cavity and top mirror temperatures obtained earlier for the oxide confined single mode VCSEL.

The experimental setup discussed in Chapter 3 was used for all of the thermoreflectance measurements. In each of the experiments, the laser current was modulated at 10Hz and the CCD camera was triggered at 40Hz. The substrate temperature of the VCSEL was held at 20.0°C using a thermoelectric cooler, while the VCSEL current was sinusoidally modulated above threshold current. Figures 4.5.1-4.5.3 show a sample of the spatially resolved thermoreflectance microscopy images for an oxide confined single mode VCSEL, oxide confined multi-mode VCSEL, and proton implanted multi-mode VCSEL respectively. Several reflectivity images at different dissipated powers (ΔP) are shown. The dissipated power was calculated the same way as for the wavelength

shift measurements; by multiplying the current by the voltage and subtracting the radiative power measured using a photo detector.

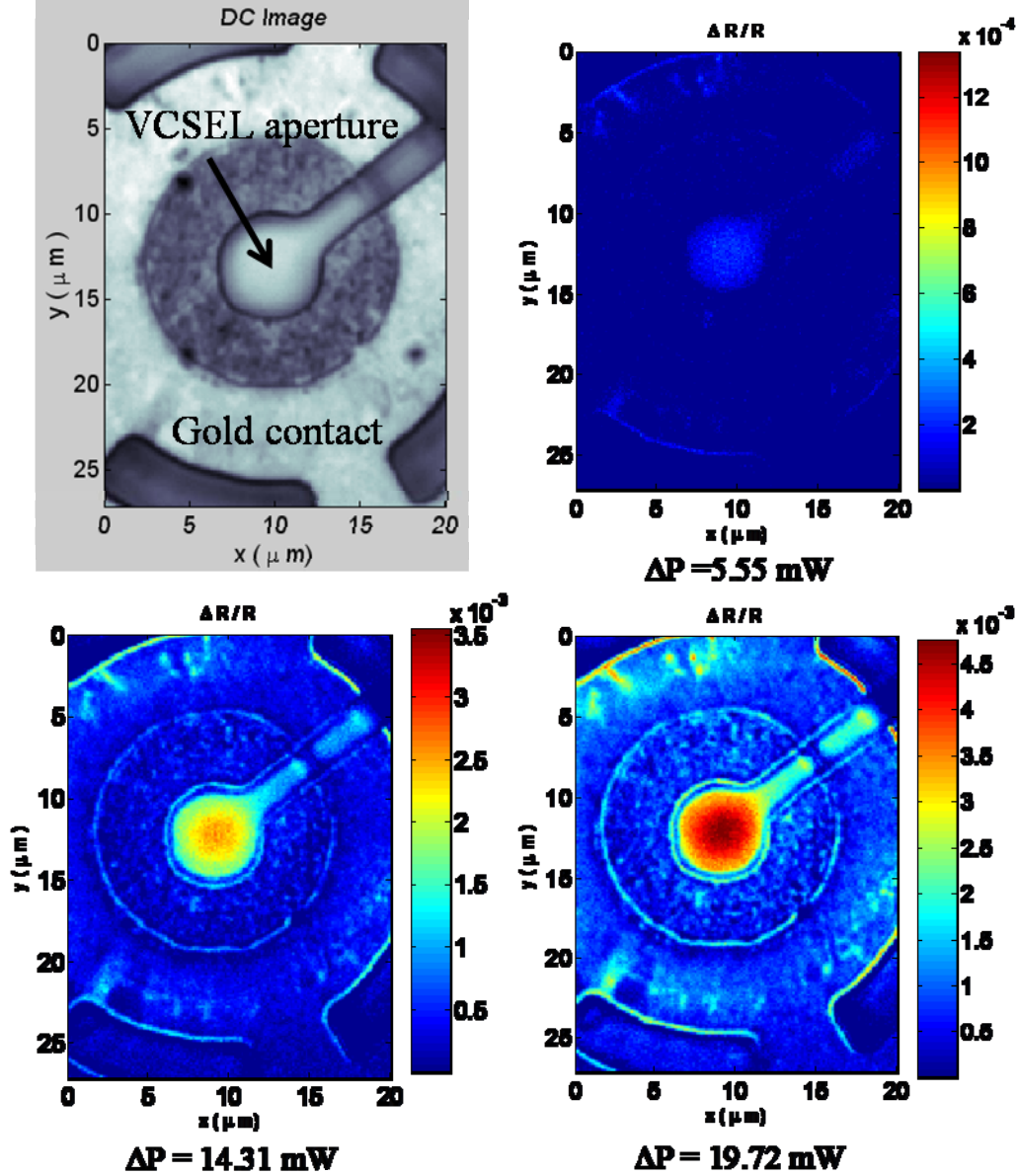


Figure 4.5.1: Uncalibrated thermoreflectance images for oxide confined single mode VCSEL with various changes in dissipated power ΔP .

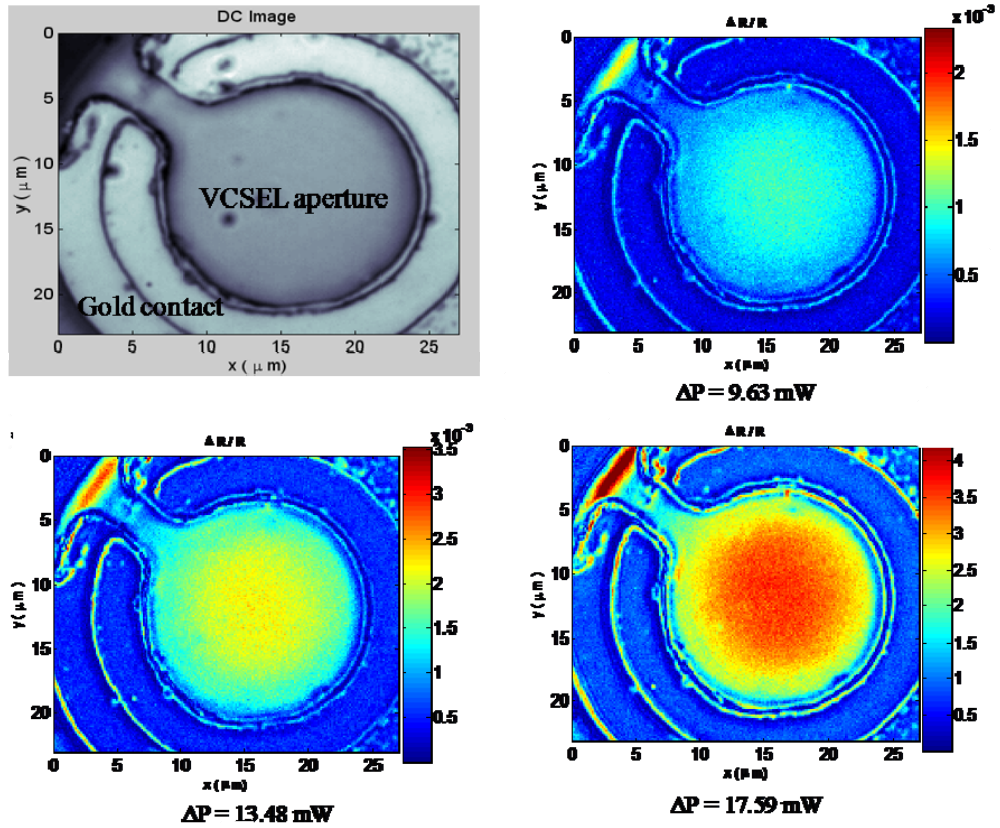


Figure 4.5.2: Uncalibrated thermoreflectance images for oxide confined multi-mode VCSEL with various changes in dissipated power ΔP .

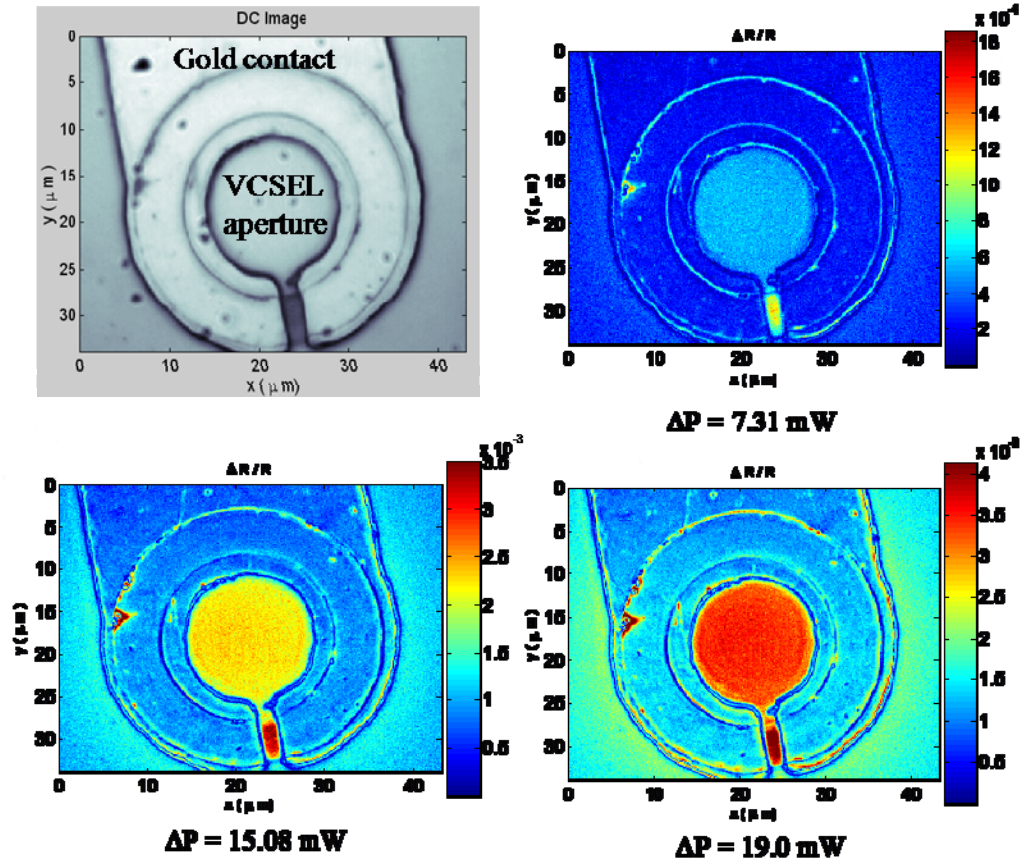


Figure 4.5.3: Uncalibrated thermorefectance images of change in reflectivity for proton implanted multi-mode VCSEL with various changes in dissipated power ΔP .

In the above three figures, it can be seen that the change in reflectivity of the VCSEL aperture increases with the change in power. In addition, the VCSELs are warmer in the center than at the edges of the apertures. This parabolic radial temperature distribution was studied by a previous thesis student who worked in Professor Hudgings' lab. She found that this temperature variation across the surface caused several thermo-optical effects, including thermal lensing in VCSELs [11].

From these thermoreflectance images in Figures 4.5.1, 4.5.2, and 4.5.3, we were able to calculate the change in temperature using the calibration coefficient, $\kappa = 2.3 \times 10^{-4} \text{ K}^{-1}$, determined earlier in Chapter 3. In order to compare the changes in temperature of the three types of lasers, the surface temperature was averaged over the entire aperture of each VCSEL. Figure 4.5.4 shows a plot of the experimentally measured change in temperature versus change in power for the three different VCSELs.

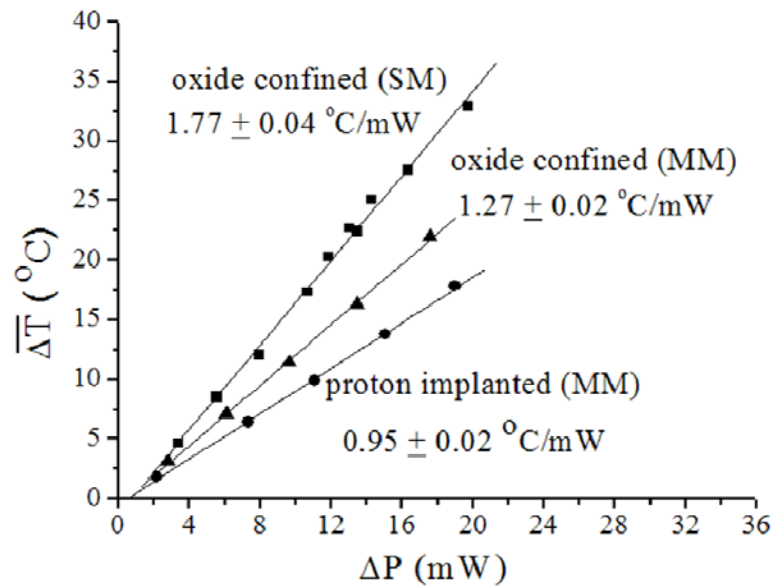


Figure 4.5.4: Experimentally measured change in temperature (ΔT) averaged over the VCSEL's aperture as a function of the change in power ΔP for the three types of VCSELs.

We found that the surface temperature for each of the three types of VCSELs varies linearly with the modulated dissipated power as expected. The measured rate of change is greatest for the oxide confined single mode VCSEL,

with a value of $1.77\text{ }^{\circ}\text{C/mW}$. The linear rate of change for the oxide confined and proton implanted multi-mode VCSELs were $1.27\text{ }^{\circ}\text{C/mW}$ and $0.95\text{ }^{\circ}\text{C/mW}$. These results are consistent with previously published values, especially in the case of the proton implanted multi-mode VCSEL [14, 25].

The three types of temperature measurement techniques for the oxide confined single mode VCSEL revealed slight discrepancies in slope of the change in temperature of the VCSEL versus the change in dissipated power, see Figure 4.5.5. This difference in the linear rate of change between the three techniques is due to each method measuring the temperature of a slightly different area of the VCSEL structure. The thermoreflectance microscopy technique measures the VCSEL's top surface, while the lasing wavelength shift and emitted electroluminescence wavelength shift measure the effective average temperature of the VCSEL as a whole and the temperature of the top DBR mirror respectively.

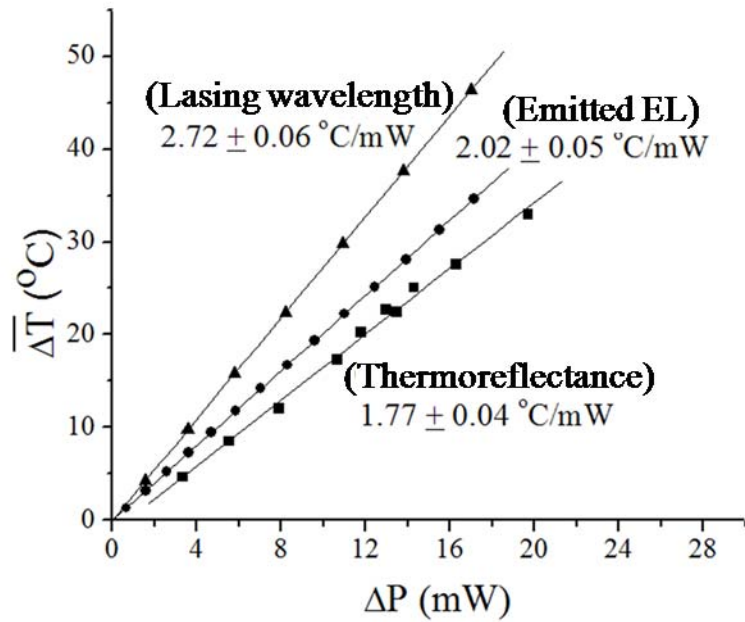


Figure 4.5.5: Experimentally measured change in temperature (ΔT) as a function of change in power dissipated (ΔP) in the oxide confined single mode VCSEL for three types of temperature measurement techniques.

The slope of the change in temperature (ΔT) versus change in dissipated power (ΔP) measured by thermoreflectance microscopy, $1.77 \text{ }^\circ\text{C/mW}$, is closer to that measured by the emitted electroluminescence peak, $2.02 \text{ }^\circ\text{C/mW}$, than the lasing wavelength peak, $2.72 \text{ }^\circ\text{C/mW}$. This leads us to conclude that the average cavity temperature of the oxide confined single mode VCSEL is the greatest, followed by the average temperature of the top DBR mirror and surface temperature of the laser. This is again consistent with published results which measure the temperature of a VCSEL using scanning thermal microscopy [2].

Overall, the single VCSEL research has shown a measurable difference in both the average cavity temperature and the surface temperature for three different types of lasers. This difference in temperature is due to the specific

structure and design of each VCSEL. In the case of the oxide confined single mode VCSEL, which showed the greatest change in surface temperature, this higher temperature was attributed to the smaller oxide confined aperture. In addition, for the oxide confined single mode VCSEL, the traditional technique of monitoring a shift in the lasing as well as emitted electroluminescence wavelengths, was compared to the high resolution thermoreflectance technique. This analysis showed the greatest temperature being that measured for the cavity followed by the temperature of the top DBR mirror and surface of the VCSEL.

5. RESULTS: VCSEL ARRAY

5.1 Introduction

With the ever increasing demand for faster transmission of information, the development and fabrication of arrays of lasers has become increasingly commercially important. In the case of vertical cavity surface emitting laser arrays, the packing density of VCSELs in such arrays has become greater and greater in the past several years, raising concerns about the inter-element thermal crosstalk between individual lasers. As discussed in Chapter 1, thermal coupling between individual VCSELs can lead to several undesirable effects including thermal lensing, decreased output power, and changes in the threshold current [9,10].

Previous research has focused on measuring the thermal coupling between individual VCSELs in an array by monitoring the shift in the lasing wavelength for each laser [12]. While this provides the average cavity temperature of the laser and allows for the investigation of bulk thermal coupling in the array, it is a single point measurement that lacks details about how the heat spreads across the array or distributes over the VCSEL apertures. In addition to the low resolution, the wavelength shift technique requires each laser under investigation to be on and coupled to optical fiber.

Instead, we use high resolution, spatially resolved thermoreflectance microscopy to simultaneously measure the temperature of multiple lasers in the array. This work on thermal coupling is presented and discussed in greater detail in Section 5.4. Using this technique we are able to measure the temperature distribution across the aperture of each VCSEL and quantify the amount of thermal crosstalk between lasers. We compared the thermal coupling in the VCSEL array measured using the wavelength shift technique to that from thermoreflectance microscopy. In addition, our thermoreflectance measurements unexpectedly revealed a possible misalignment between the optical and current apertures in the modulated VCSEL.

Several properties of the VCSEL array, including the thermal conductivity and thermal diffusivity, were also experimentally determined. The thermal conductivity was calculated using the data from the thermoreflectance microscopy measurements and compared to previously reported values for the array material. This calculation will be discussed in more detail in Section 5.4. The thermal diffusivity was experimentally determined using a time gating experiment explained in Section 5.5. By comparing the phase shift between the temperature modulations for the driven VCSEL and neighboring VCSEL at different frequencies, the thermal diffusivity of the VCSEL array could be calculated. This novel technique enables measurement of the thermal diffusivity of complex structures such as VCSELs, which are made of hundreds of thin layers. We contrast these results to traditional measurements on bulk and thin film materials.

5.2 VCSEL Array Characteristics

The VCSEL array, shown in Figure 5.2.1, used in this research was originally fabricated at Sandia National Labs and given to us second hand. Therefore, before conducting experiments to measure the thermal coupling, conductivity, and diffusivity, basic characterization of the VCSEL needed to be done. Figure 5.2.1 shows the one dimensional array consisting of ten, $17\mu\text{m}$ square aperture, VCSELS spaced approximately $125\mu\text{m}$ apart. The VCSEL array was soldered onto a copper heat sink and directly probed for all measurements.

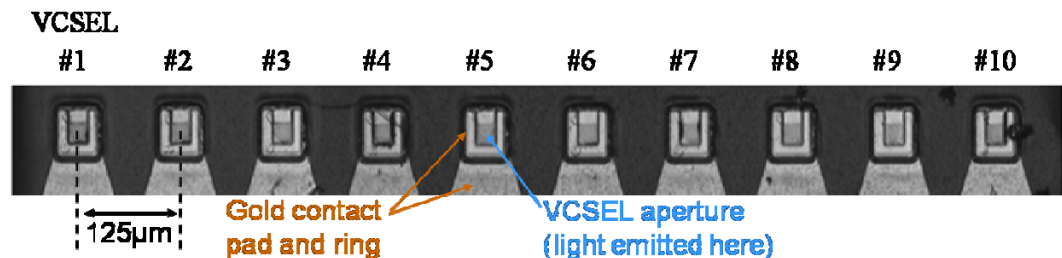


Figure 5.2.1: Picture of 1D Sandia VCSEL array.

In order to gain more insight into the structure of the device, wavelength spectra for several of the VCSELS in the array were taken using the setup in Figure 3.2.2. From these spectra, shown in Figure 5.2.2, it was determined that the VCSELS in the array were 850nm multi-mode lasers. At low currents a few transverse mode peaks were observed, but as the current and/ or temperature of the lasers was increased, numerous other transverse modes began to appear.

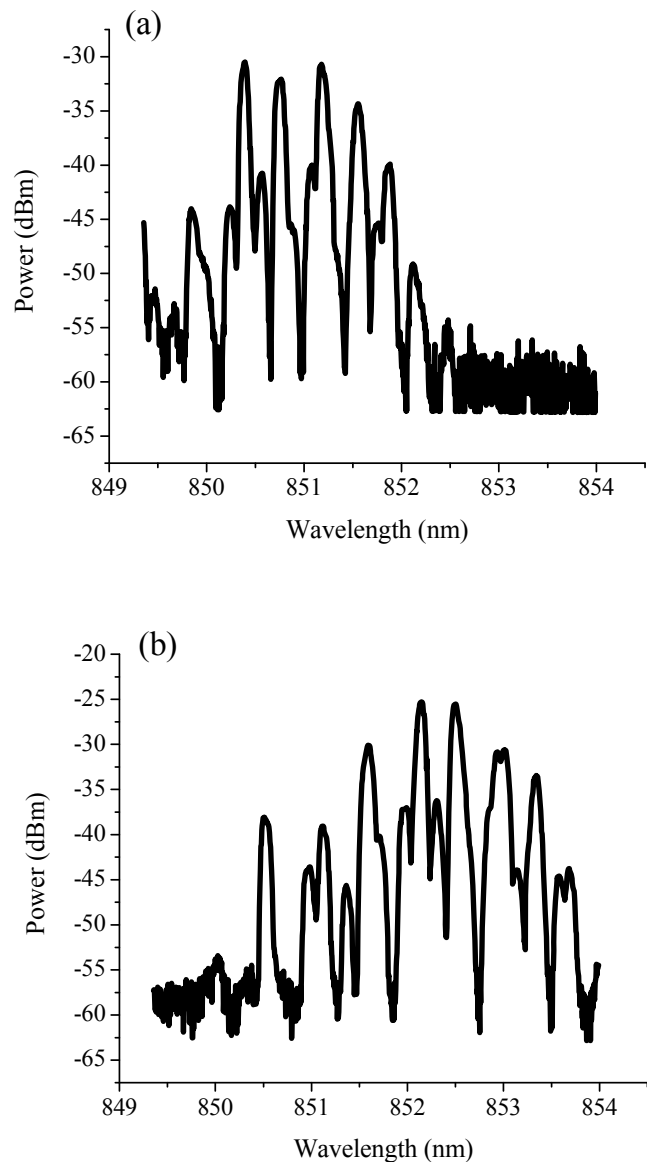


Figure 5.2.2: Emission spectrum for a VCSEL in the Sandia array at (a) 10mA and (b) 20mA. Lasers clearly lase in multiple transverse modes.

In addition, plots of the power versus current (LI curve) and voltage versus current (IV curve), for one of the VCSELs in the array, are shown in Figure 5.2.3. The average threshold current for the lasers in the array is

approximately 4mA. These lasers also have a wallplug efficiency of ~5%, meaning that almost all of the power is dissipated as heat in the device.

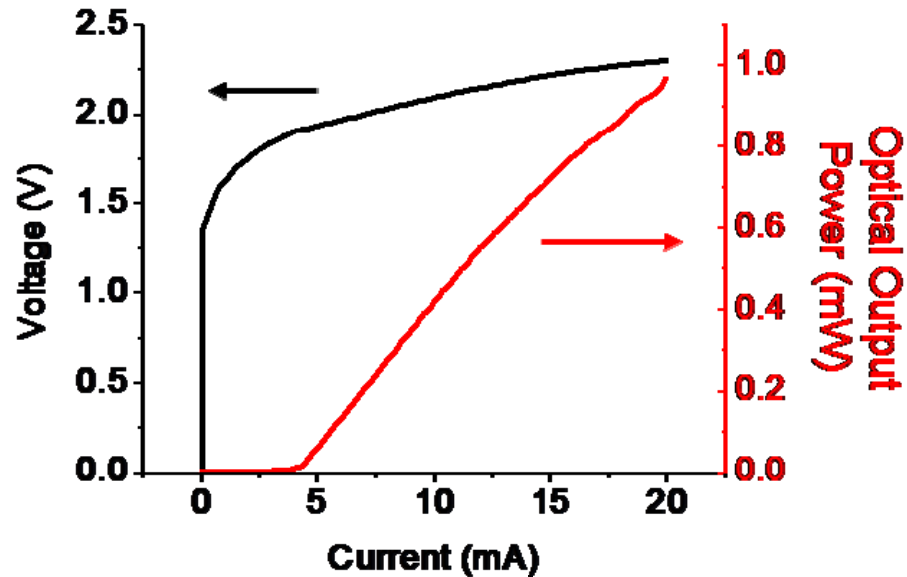


Figure 5.2.3: LI and IV curves for a typical VCSEL in the array.

5.3 Temperature Distribution Across Individual VCSEL Apertures

As mentioned previously, one of the advantages of thermoreflectance microscopy over traditional techniques is its high spatial resolution. In these thermoreflectance measurements, the first VCSEL in the array (VCSEL #1) was probed and sinusoidally modulated between 0-20mA. The experimental setup in Figure 3.3.1 was used with VCSEL #1's current modulated at 5Hz and the CCD camera triggered at 20Hz. The remaining three VCSELs (VCSEL #2, VCSEL #3, and VCSEL #4) were unbiased. An image taken, using a 20x microscope

objective, of the change in reflectivity $\Delta R/R$ for this experiment is shown in Figure 5.3.1.

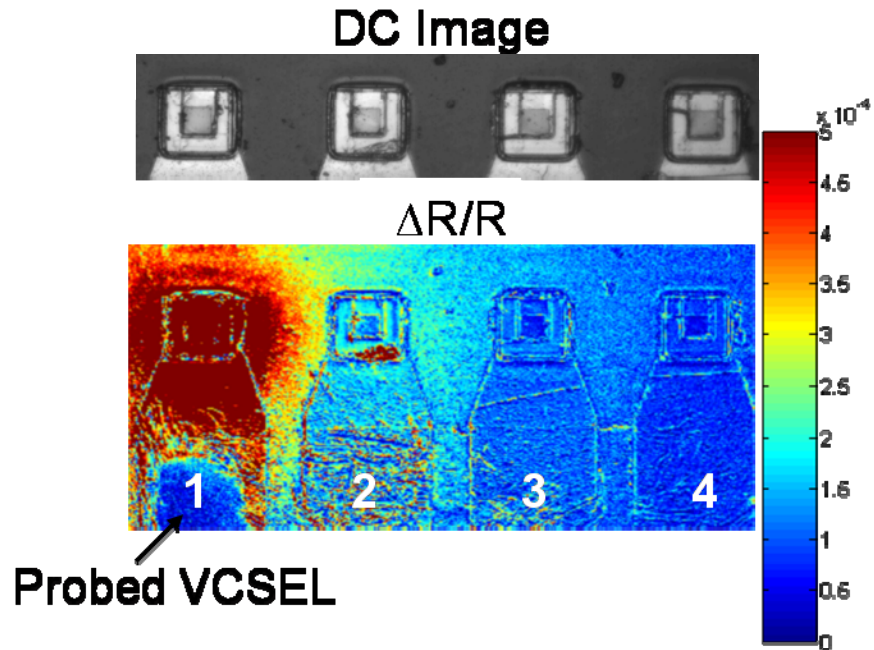


Figure 5.3.1: DC and thermoreflectance image of $\Delta R/R$ for VCSELs #1-4 using a 20x objective with VCSEL #1's current modulated from 0mA-20mA.

The resulting temperature distribution across each VCSEL was imaged, as shown in Figure 5.3.2. These temperature distributions were obtained by vertically averaging the temperatures over the aperture of the VCSEL.

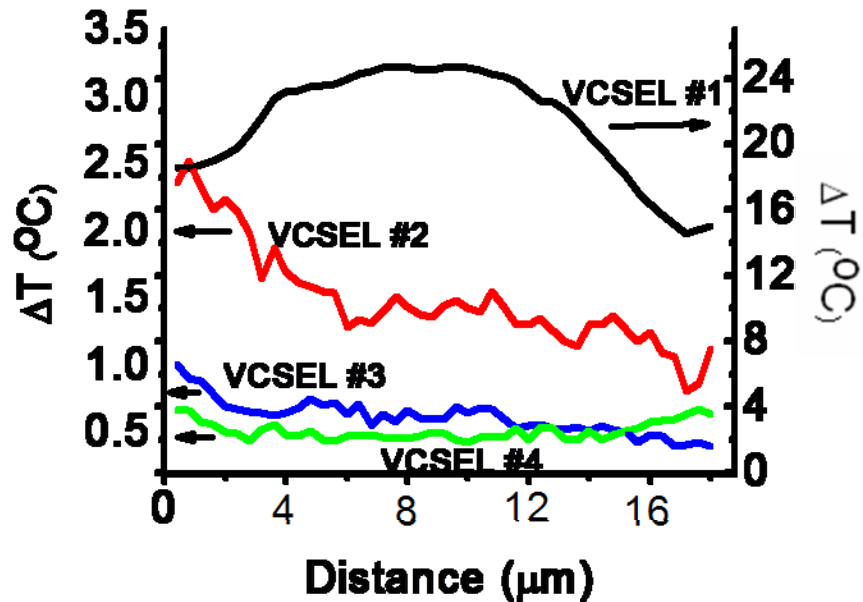


Figure 5.3.2: Temperature profile across horizontal cross section of VCSEL apertures.

The temperature profile of the modulated laser (VCSEL #1) in the array shows thermal lensing which agrees with previous research performed on single VCSELs [14]. The thermoreflectance microscopy images for the apertures of adjacent lasers, VCSEL #2 and VCSEL #3, show the temperature on the side of the aperture closest to the modulated VCSEL is greater than the temperature on the opposite side. This temperature variation across the aperture of the neighboring lasers is due to the thermal coupling between VCSEL #1 and the neighboring VCSEL. As expected, the amount of thermal coupling between the lasers decreases as the distance between them increases.

Additional measurements were performed to examine the curvature in the thermal distribution of the modulated VCSEL at numerous electrical powers.

Figure 5.3.3 shows three thermoreflectance images at different changes in electrical powers ΔP , $\Delta P = 24\text{mW}$, $\Delta P = 34\text{mW}$, and $\Delta P = 44\text{mW}$.

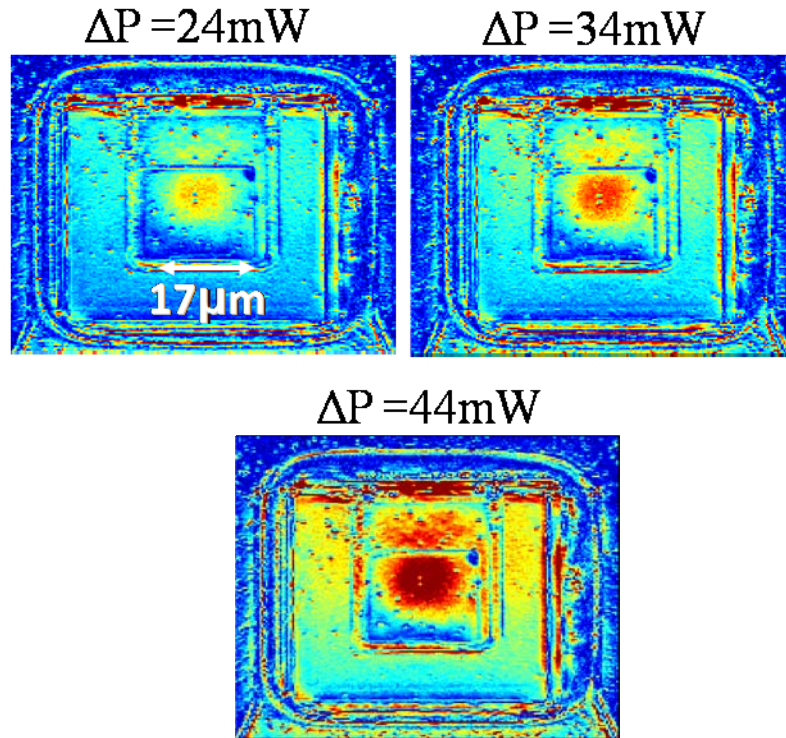


Figure 5.3.3: Thermoreflectance images of a single VCSEL in array at various changes in electrical powers (ΔP).

As the change in electrical power increases, the change in the reflectivity, and therefore the change in temperature, also increases. These results are consistent with single VCSEL work presented in Chapter 4 [14]. To analyze the curvature of the temperature profile, radial averaging across the VCSEL aperture was done using Matlab and is shown in Figure 5.3.4. These results show an increase in the curvature of the thermal profiling with increasing electrical bias powers. This curvature in the operated VCSEL leads to thermal effects mentioned before such as thermal lensing [9,14].

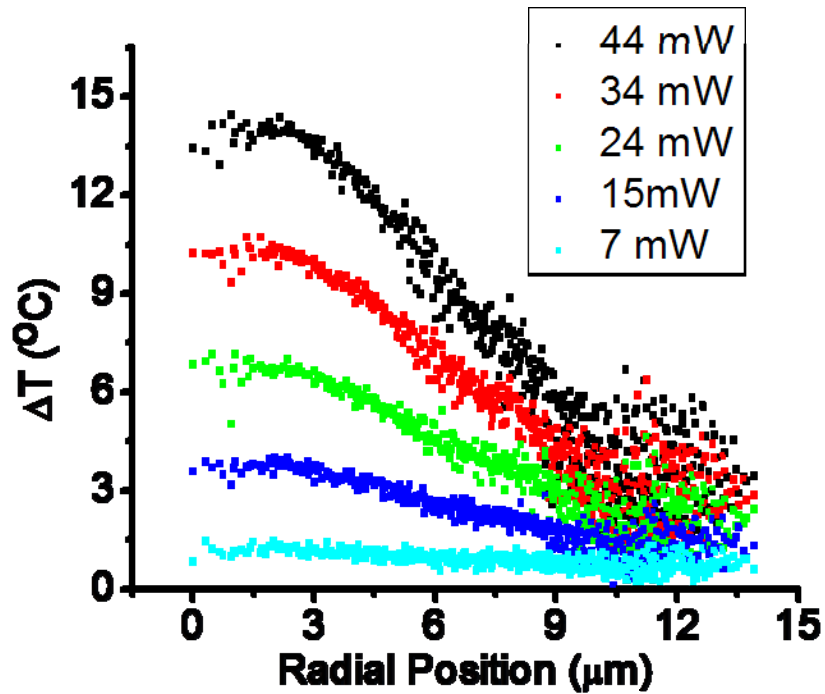


Figure 5.3.4: Curvature in thermal profiles with increasing change in electrical bias powers measured from the center of the modulated VCSEL aperture.

Another interesting but unanticipated discovery using thermoreflectance microscopy on individual VCSELs in the array is that the hotspot of the VCSEL appears to be offset from the center of the aperture. The temperature profile of the single VCSEL is compared to an image of the beam shape in Figure 5.3.5. While the hottest portion of the aperture is offset from the center, the output beam is not. This offset in the beam and temperature profile may be due to a possible misalignment in the optical aperture, which determines where the output beam is located, and the current aperture, which determines where the current is directed and therefore the location of the warmest temperature, of the laser. This

misalignment would have been undetected using any of the other techniques described in Chapter 1.

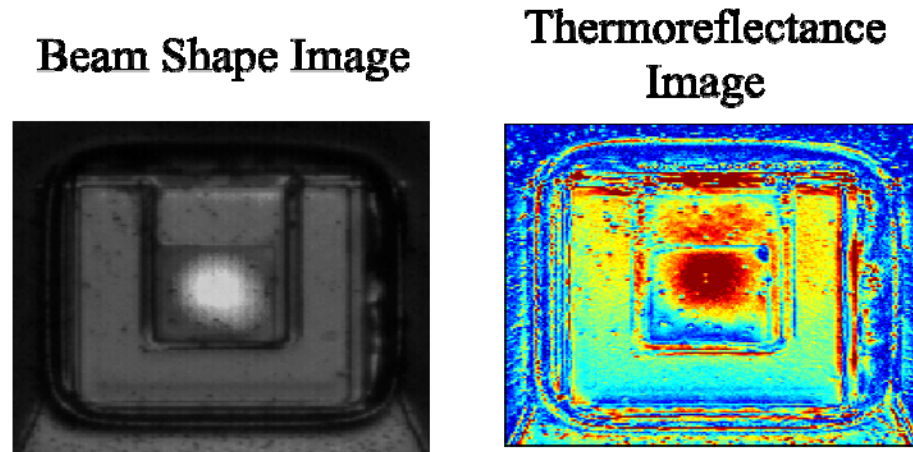


Figure 5.3.5: Comparison of beam shape and thermoreflectance image for single VCSEL in the array.

5.4 Thermal Coupling

Two techniques, wavelength shift and thermoreflectance microscopy, were used in this research to measure the amount of thermal coupling between individual lasers in the array.

5.4.1 Thermoreflectance Microscopy:

Using the wavelength shift technique to examine thermal coupling in a VCSEL array requires several individual measurements and only provides a single data point for each laser aperture. Instead, spatially resolved, high resolution thermoreflectance microscopy offers the ability to resolve heat

spreading between individual VCSELs in the array, while simultaneously imaging the temperature distribution across individual VCSEL apertures. As mentioned before and shown in Figure 5.4.1, significant thermal coupling is measured between VCSEL #1 and the neighboring VCSELs.

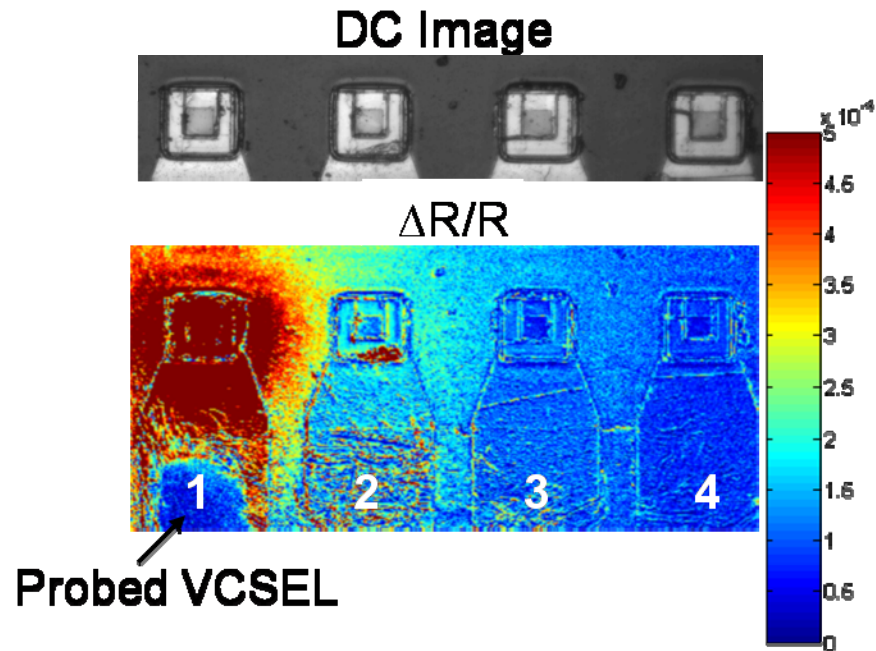


Figure 5.4.1: DC and thermoreflectance image of $\Delta R/R$ for VCSELs #1-4 using a 20x objective with VCSEL #1's current modulated from 0mA-20mA.

In Figure 5.4.1, the modulated VCSEL is the left most laser and the change in reflectivity ($\Delta R/R$) is proportional to the change in temperature, given by Equation 3.2. The change in the reflectivity is greatest near the modulated VCSEL and is seen to spread radially outward from the first VCSEL. Using this thermoreflectance data, the thermal coupling between individual VCSELs was calculated. The change in reflectivity was averaged over each VCSEL aperture

and the change in temperature was calculated using the thermoreflectance calibration coefficient from Chapter 3. The change in temperature (ΔT) for each of the four VCSELs was experimentally measured to be 21.35°C, 1.50°C, 0.62°C, and 0.52°C respectively, see Figure 5.4.2. Additionally, thermoreflectance microscopy measurements were done using a 40x microscope objective and provided consistent results to those obtained using the 20x objective.

5.4.2 Wavelength Shift and Thermoreflectance Microscopy Comparison:

The VCSEL array temperatures obtained using thermoreflectance microscopy are compared to those measured using the shift in the lasing wavelength in Figure 5.4.2. The thermal coupling experiments measured by monitoring a shift in the lasing wavelength were performed by varying the current to VCSEL #1 and measuring the change in wavelength of VCSEL #1, VCSEL #2, VCSEL #3, and VCSEL #4 separately. For each wavelength shift experiment, with the exception of VCSEL #1 which was being modulated, the VCSEL under investigation was on at a constant current of 10mA. To relate the resulting shift in wavelength to a change in temperature for each VCSEL calibration experiments similar to those presented in Chapter 4 were performed.

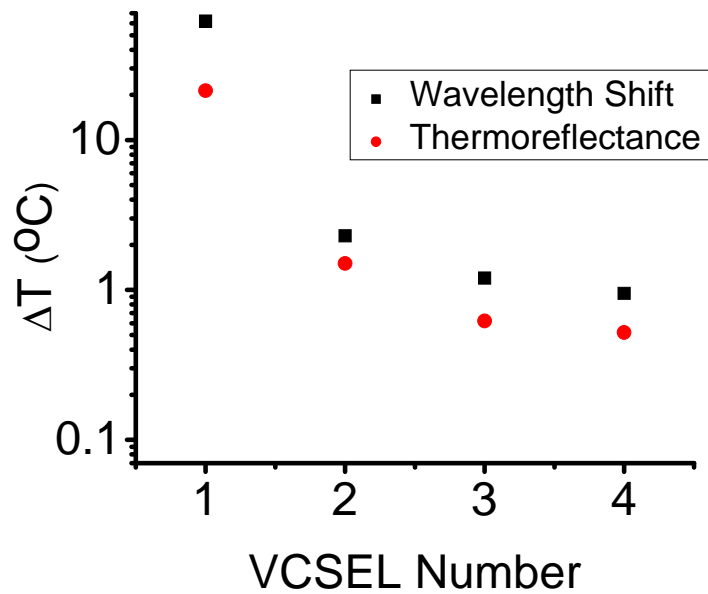


Figure 5.4.2: Thermal coupling in VCSEL array measured using wavelength shift and thermoreflectance microscopy techniques. VCSEL #1 is probed and modulated. The temperature of each of the four VCSELs is measured.

The thermal coupling measured using the shift in the lasing wavelength provides a greater change in temperature than the thermoreflectance microscopy technique [23]. The VCSEL array data is qualitatively similar to the single VCSEL results and is consistent with previous research [14]. The higher changes in temperature measured for each VCSEL using the lasing wavelength shift are due to the technique measuring the average cavity temperature, as discussed previously in Chapter 4. The thermoreflectance technique, on the other hand, measures the top surface temperature of the laser. If there is a large thermal impedance between the VCSEL cavity and the top surface, one would expect the surface to be significantly cooler than the cavity where the heat source is located.

5.4.3 Thermal Impedance and Lateral Thermal Conductivity:

To better understand this difference in the measured temperatures for the array, the lateral thermal impedance between the lasers and the lateral thermal conductivity across the array were calculated. Previous researchers have calculated the lateral thermal impedance of a 4x4 array of vertical cavity surface emitting lasers; a similar approach was used in this research [12]. The thermal impedance (Z_{12}) between VCSEL #1 and VCSEL #2 in the array depends on the thermal resistivity of the material ρ_{th} and the geometry of the heat flow:

$$Z_{12} = \frac{\rho_{th} (\text{length})}{(\text{area})} \quad (5.1)$$

In the case of the VCSEL array, the length is the distance between the lasers r and the cross-sectional area through which the heat flows is $(1/2) (4\pi r^2)$. This area is half the surface area of a sphere and is due to the heat spreading out radially from the modulated VCSEL, depicted pictorially in Figure 5.4.3.

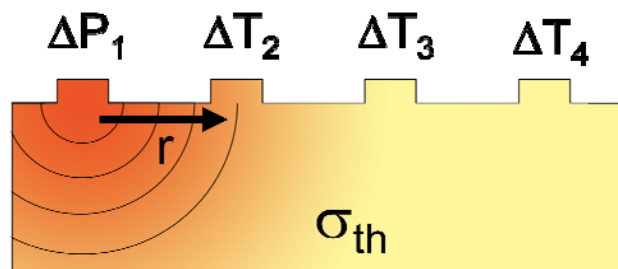


Figure 5.4.3: Radial heat spreading from modulated VCSEL.

In addition, the thermal resistivity ρ_{th} is related to the thermal conductivity σ_{th} , a material property that describes how well it is able to conduct heat:

$$\rho_{th} = \frac{1}{\sigma_{th}} \quad (5.2)$$

Therefore, the thermal impedance Z can be expressed as:

$$Z = \frac{2\pi r^2 \sigma_{th}}{r} = (2\pi r) \sigma_{th} \quad (5.3)$$

In order to extract σ_{th} , we wish to measure Z for various values of r . In practice this was accomplished by measuring the thermal impedance between VCSEL #1 and its three closest neighbors. The thermal impedance of the VCSEL determines how much the temperature will change (ΔT) in the laser for a certain change in power (ΔP). Experimentally, the thermal impedance was measured by monitoring the change in temperature of VCSEL #2, #3, and #4 ($\Delta T_2, \Delta T_3, \Delta T_4$) as the power to VCSEL #1 was modulated (ΔP_1):

$$Z_{12} = \frac{\Delta P_1}{\Delta T_2} \quad Z_{13} = \frac{\Delta P_1}{\Delta T_3} \quad Z_{14} = \frac{\Delta P_1}{\Delta T_4} \quad (5.4)$$

The thermal impedance, measured using thermoreflectance microscopy, between VCSEL #1 and VCSEL #2 was equal to 0.030 W/K. In addition the thermal impedance between VCSELs #1 and #3 and VCSELs #1 and #4 was experimentally determined to be 0.072 W/K and 0.086 W/K respectively. A plot of Z versus $2\pi r$ for both the data obtained using the wavelength shift and thermoreflectance microscopy is shown in Figure 5.4.4. From Equation 5.4, the slope of these plots is the desired thermal conductivity σ_{th} .

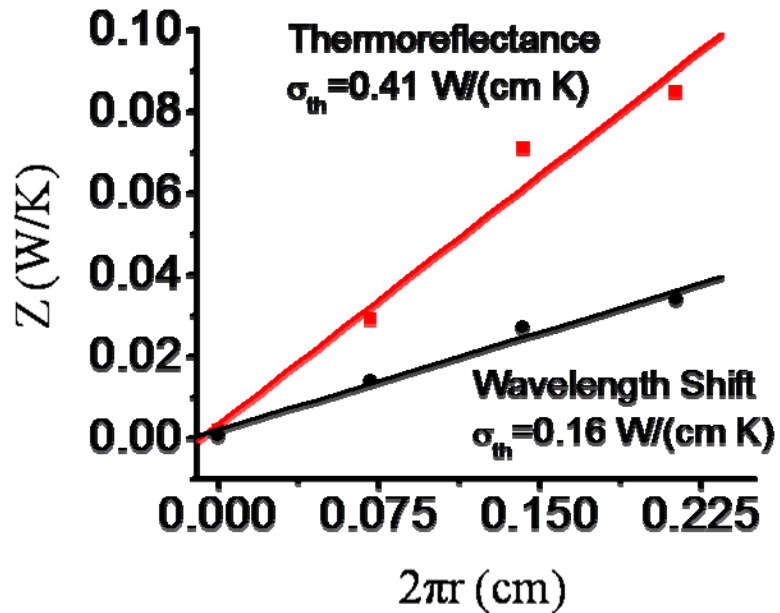


Figure 5.4.4: Thermal impedance versus VCSEL spacing for VCSEL array using wavelength shift and thermoreflectance techniques.

The thermal conductivity determined using the wavelength and thermoreflectance techniques was equal to 0.16 W/(cm K) and 0.41 W/(cm K) respectively. These results were compared to typical values for the thermal conductivity of GaAs, $\sigma_{th} = 0.45$ W/(cm K) and AlGaAs, $\sigma_{th} = 0.9$ W/(cm K), the two main materials from which the VCSEL array is made [26]. The experimentally determined thermal conductivity value of the VCSEL array using thermoreflectance shows good agreement with the value of GaAs from the literature.

5.5 Thermal Diffusivity

In addition to measuring lateral thermal coupling and lateral thermal impedance between VCSELs in the array, a time gated experiment was conducted to determine the thermal diffusivity. Thermal diffusivity is a measure of how quickly a material can change its temperature due to the addition of heat. In particular in our work, thermal diffusivity is a measure of how fast a thermal wave will move from the modulated VCSEL across the array surface. While thermal diffusivity values can be found in the literature for bulk materials as well as thin films, very little research has focused on measuring the thermal diffusivity in a complex VCSEL array structure, consisting of metal contacts, DBR mirrors, gain medium, etc. [27,28].

The experimental setup for these set of experiments is very similar to that for the wavelength shift measurements and is shown in Figure 5.5.1. The two function generators are phase locked with sinusoidal modulation of the current (between 10mA and 20mA) to one of the VCSELs (VCSEL #4). The second function generator, connected to the optical spectrum analyzer, is set on pulse with a duty cycle of 1%. The duty cycle determines how much of the sine wave the optical spectrum analyzer will look at when building up the lasing spectrum of the VCSEL under investigation. For each measurement taken, the phase of this pulse is changed by 30 degrees. This will be discussed in greater detail later in

this section. The spectra at each of the different pulse phases are obtained on the optical spectrum analyzer.

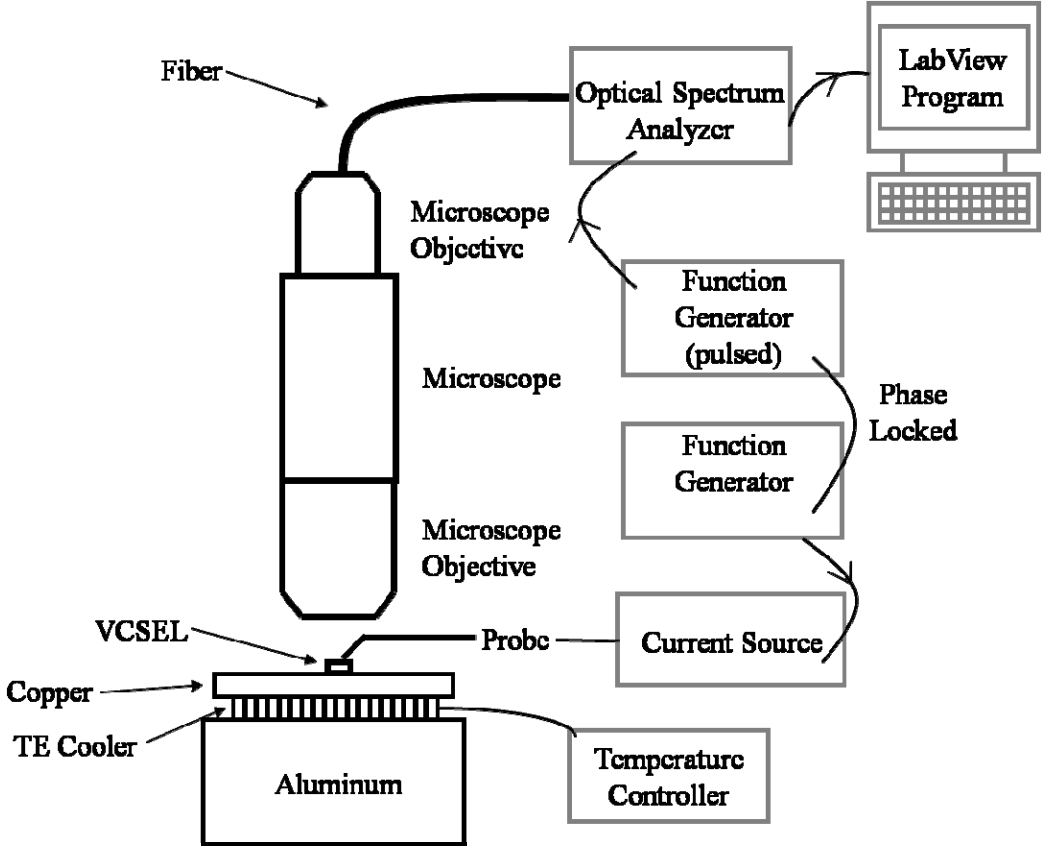


Figure 5.5.1: Experimental setup for time gated experiment.

In this experiment, the current to VCSEL #4 is sinusoidally changed causing a sinusoidal modulation of the temperature, shown schematically in Figure 5.5.2 (a). This modulation of the current of VCSEL #4 also causes the temperature of the neighboring VCSEL to change. As shown in Figure 5.5.2 (b), however, it takes some time for the heat to move from the modulated VCSEL to the neighboring VCSEL. Therefore, there is a phase shift between the

temperature versus time plot for the modulated VCSEL and the temperature versus time plot for the neighboring VCSEL. We measure this change in temperature for both the modulated and neighboring VCSEL by monitoring the shift in the lasing wavelength for each VCSEL. By comparing the shifts in wavelength for the two VCSELs, we are able to determine the phase shift between the temperature modulations of the two VCSELs, shown in Figure 5.5.2 (c).

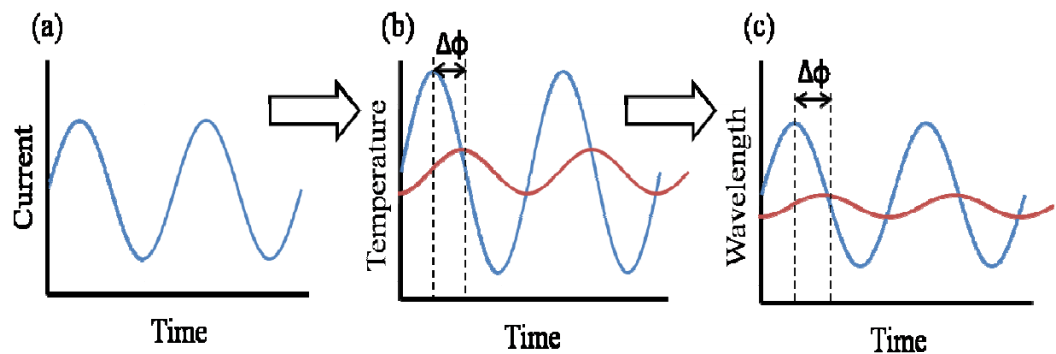


Figure 5.5.2: (a) Schematic of current versus temperature of modulated VCSEL (b) The sinusoidal modulation of temperature in VCSEL #4 (blue) causes a time delayed modulation of the temperature in VCSEL #5 (red). The temperature variations can be measured via the resulting wavelength shift, shown schematically in (c).

The first step in the time gated experiment is to obtain a plot of the wavelength versus phase of the pulse. (It is important to note that this phase is not the same phase mentioned in the above paragraph.) Figure 5.5.3 shows the sine wave modulation to VCSEL #4, the pulse from the second function generator, and the spectra at three different phases. In this figure, it can be seen that as the phase of the second function generator (pulse) is adjusted, the wavelength shifts to the left. This shift in the wavelength to the left is due to the

fact that the pulse is looking at a part of the wave where the current is lower than before and therefore the temperature is less, corresponding to a wavelength shift.

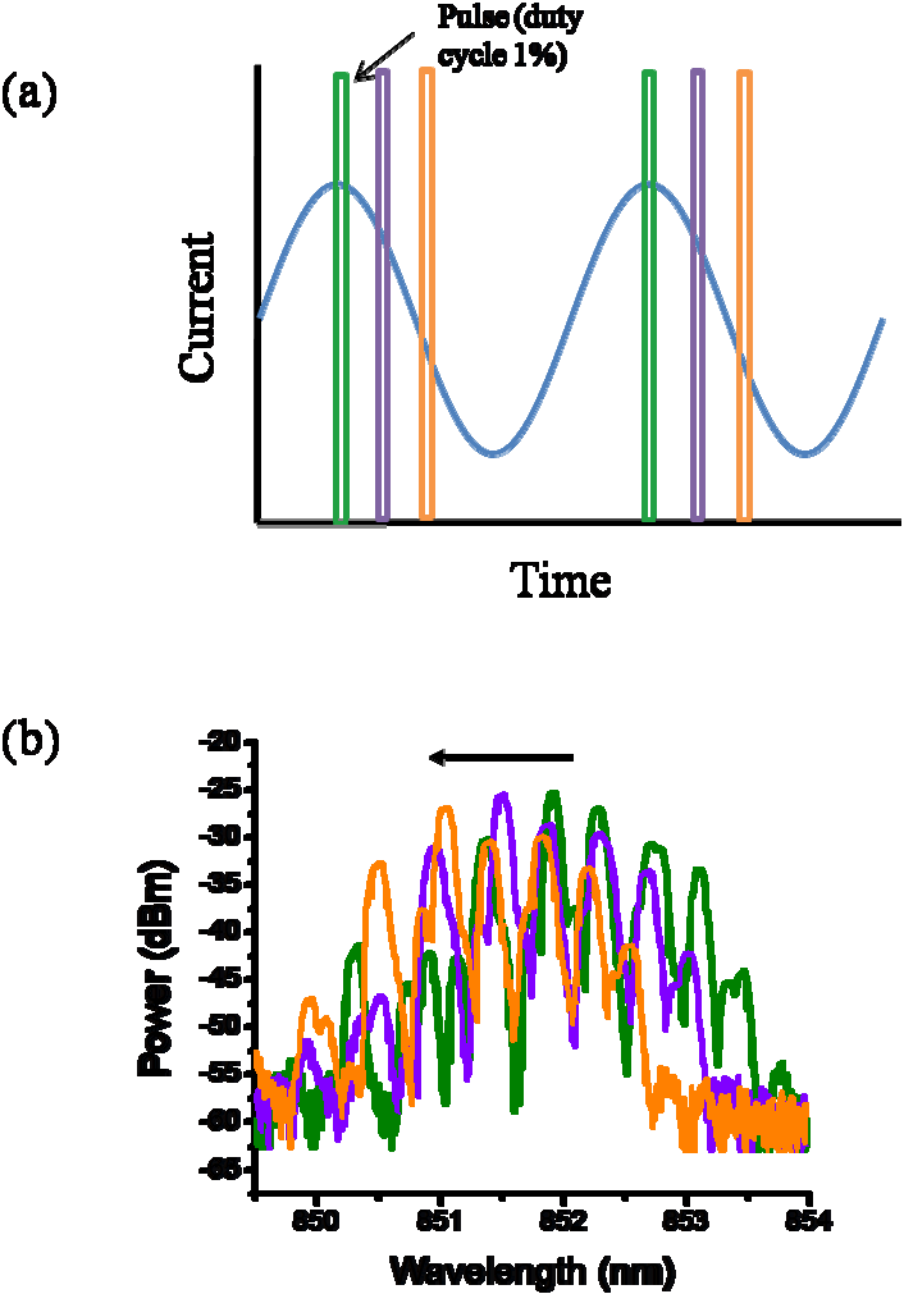


Figure 5.5.3: (a) Current versus time for modulated VCSEL, showing pulses at three different windows of time in which we capture the optical spectra (b) lasing spectra corresponding to the pulses in (a). $\theta = 120^\circ$ shown in green, $\theta = 150^\circ$ shown in purple, $\theta = 180^\circ$ shown in orange.

This experiment was repeated 13 times by changing the phase from 0° to 360° in increments of 30° . One of the peaks in the spectrum was chosen and its shift monitored throughout all of the experiments. A plot of the wavelength for the chosen peak versus measurement phase, at a modulation frequency of 400Hz, is shown in Figure 5.5.4. This figure clearly shows a shift in the wavelength due to the sinusoidal current modulation of the VCSEL.

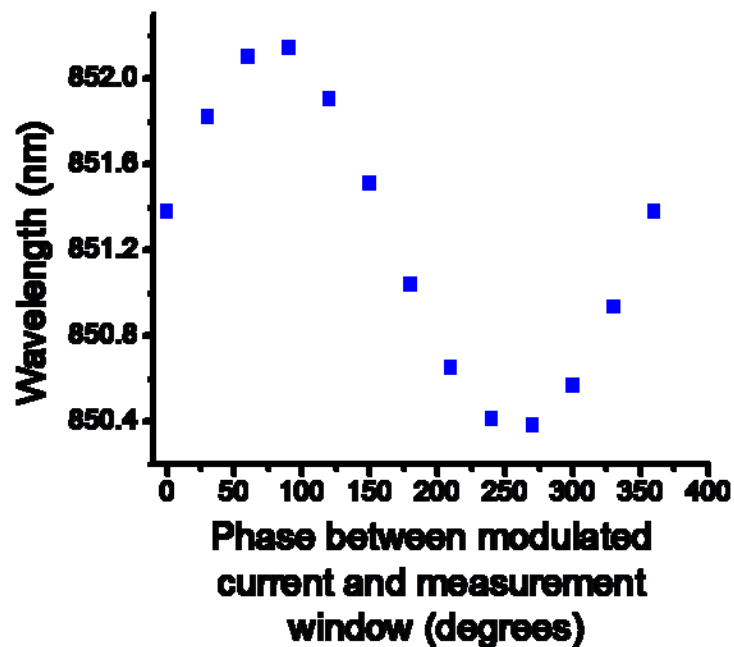


Figure 5.5.4: Wavelength shift versus phase of the pulse for the modulated VCSEL ($I = 10\text{mA} - 20\text{mA}$) at a frequency of 400Hz .

The same experiment as above was repeated, except for this time we monitored a shift in the lasing wavelength of the neighboring VCSEL #5 instead

of the modulated VCSEL #4. As expected, the shift in the wavelength was much smaller for the neighboring VCSEL (~0.015nm).

Comparing the two normalized wavelength versus measurement phase plots shows a clear phase shift ($\Delta\phi$) between the data for the two VCSELs, as shown in Figure 5.5.5. At 400Hz this phase shift is approximately 58.8° .

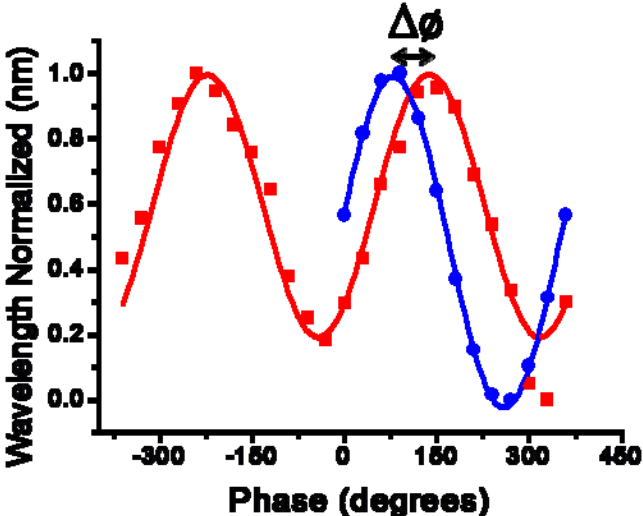


Figure 5.5.5: Phase shift between change of wavelength for modulated VCSEL 4 (blue) and neighboring VCSEL 5 (red) at a frequency of 400Hz.

To calculate the thermal diffusivity for the VCSEL array, the set of experiments described above was done at a range of frequencies between 200Hz and 1kHz. At each frequency the phase shift between VCSEL #4 and VCSEL #5 was measured; results (phase shift versus square root of frequency) are shown in Figure 5.5.6.

As expected, the phase shift at lower frequencies was less than that at higher frequencies. This is due to the fact that the heat takes a certain amount of time to move between VCSEL #4 and VCSEL #5. At the lower frequencies, the period of the wave, time it takes to complete one cycle, is longer than at higher frequencies. Given that the time it takes for the heat to travel between VCSELs is fixed, a smaller phase shift at a lower frequency will correspond to the same time as a larger phase shift at a higher frequency.

The thermal diffusivity α can be obtained from our phase shifts by:

$$\Delta\varphi = \frac{180}{\pi} \sqrt{\frac{f\pi}{\alpha}} d \quad (5.6)$$

where $\Delta\varphi$ is the phase shift between the temperature modulation of VCSEL #4 and VCSEL #5, f is the frequency of modulation, and d is the distance between the two VCSELs (125 μ m). This equation is used in the literature to calculate the thermal diffusivity of bulk materials and thin film structures [28].

To determine the thermal diffusivity, a plot of the phase shift ($\Delta\varphi$) versus square root of frequency (\sqrt{f}) including error bars is shown in Figure 5.5.6.

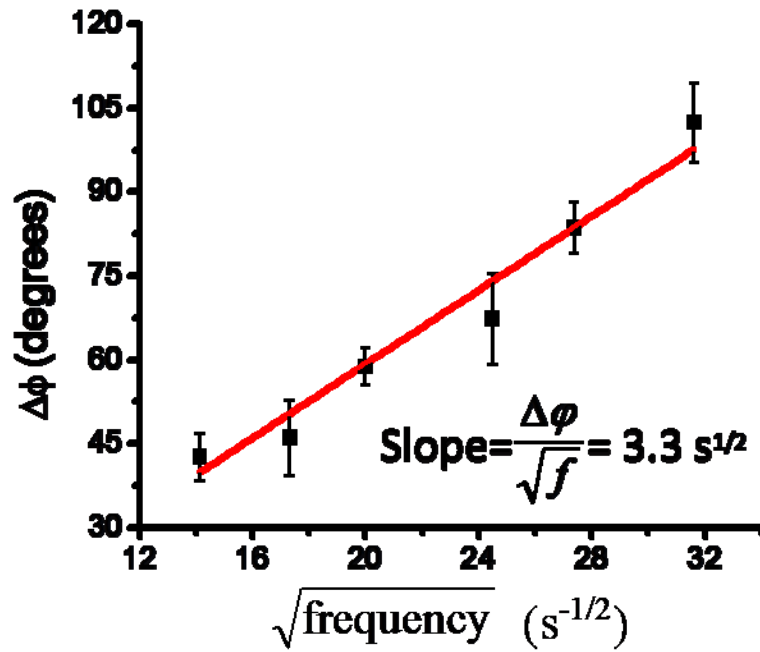


Figure 5.5.6: Plot of phase shift at a range of frequencies.

Using the slope of the linear fit ($3.3\text{s}^{1/2}$), the thermal diffusivity for the VCSEL array was calculated to be $\alpha = 1.47 \times 10^{-5} \text{ m}^2\text{s}^{-1}$. This value shows relatively good agreement with literature values for the thermal diffusivity of bulk GaAs, ($\alpha = 3.1 \times 10^{-5} \text{ m}^2\text{s}^{-1}$) and for thin film GaAs (in plane: $\alpha = 2.3 \times 10^{-5} \text{ m}^2\text{s}^{-1}$; cross plane: $\alpha = 1.3 \times 10^{-5} \text{ m}^2\text{s}^{-1}$) [27,28]. However, with this relatively simple and novel time gated experiment, we have been able to determine the thermal diffusivity for the VCSEL array structure as a whole.

Overall, this work on VCSEL arrays has shown significant thermal coupling between individual VCSELs in the array, measured using both the

wavelength shift and thermoreflectance microscopy techniques. Similar to the measurement of ΔT in the single VCSEL case, the wavelength shift technique showed greater heating than thermoreflectance microscopy. This discrepancy in the temperatures was investigated further by determining the thermal impedance in the array and determining the thermal conductivity using data collected from both techniques. In addition, further investigation was done utilizing the high resolution of thermoreflectance microscopy to investigate the temperature distribution across the apertures of numerous VCSELS in the array. A parabolic temperature distribution, indicating thermal lensing, was seen in the modulated VCSEL while temperature gradients were apparent across neighboring VCSEL's apertures.

Lastly, the thermal diffusivity of the VCSEL array was determined using a time gated experiment. Results obtained show fairly good agreement with values reported for bulk and thin film structures of similar materials. We would expect our value of the thermal diffusivity for the VCSEL array to vary slightly from that for the bulk material and thin films since we are measuring the thermal diffusivity of the entire VCSEL array structure. For heat to propagate from one VCSEL to the next, it must propagate cross-plane through the bottom layer stack in the first VCSEL, then laterally in plane across to the next VCSEL. Hence, our measured VCSEL array diffusivity is difficult to extract from typical in-plane and cross-plane diffusivity values in the literature, illustrating the value of our direct measurement technique.

6. CONCLUSIONS

In summary, a variety of temperature measurement techniques were used to investigate the thermal behavior of individual VCSELs and VCSEL arrays under standard operating conditions. In the case of single VCSELs, high spatial and thermal resolution thermoreflectance microscopy was performed on three different types of VCSELs: oxide confined single-mode, oxide confined multi-mode, and proton implanted multi-mode. The results indicate that greater heating occurs in the oxide confined single-mode VCSEL than in either of the multi-mode lasers. We believe that this higher temperature in the oxide confined single mode VCSEL can be attributed to a greater current density in the device due to its smaller aperture. In addition, we also see a strong parabolic temperature distribution across the surface of the single-mode VCSEL; this effect is much less severe in multi-mode VCSELs.

To verify our thermoreflectance microscopy measurements, lower resolution temperature measurements using lasing wavelength shift and emitted electroluminescence wavelength shift were conducted on the oxide confined single mode VCSEL. Our experimental results show a greater change in temperature measured monitoring a shift in the lasing wavelength than monitoring a shift in the emitted electroluminescence wavelength. The lasing wavelength shift provides the average cavity temperature of the VCSEL, while a wavelength shift in the emitted electroluminescence allows us to measure the temperature of the top mirror of the device. By comparing these results to those obtained using

thermoreflectance microscopy, we conclude that the average cavity temperature of an operating VCSEL is greater than the top mirror and surface temperatures of the laser.

The second half of this thesis focused on investigating the thermal coupling and temperature distribution in VCSEL arrays. Thermoreflectance microscopy is an ideal temperature measurement technique for VCSEL arrays because it provides the ability to simultaneously measure the temperature of the VCSEL array at very different length scales (5-20 μm for the VCSEL aperture and $\sim 1\text{mm}$ for the entire array). Thermoreflectance measurements showed radial heat spreading away from the modulated VCSEL, thermal lensing in the modulated VCSEL, significant thermal coupling between neighboring VCSELs, and temperature gradients across the apertures of neighboring VCSELs in the array. In addition, higher magnification thermoreflectance measurements on the operating VCSEL showed a large temperature distribution across the surface of the laser aperture, with the temperature at the center of the VCSEL greater than the temperature near the edges of the aperture. Comparing the thermoreflectance images obtained for a single VCSEL in the array to a beam shape image revealed that the hotspot of the laser was offset from the center of the aperture. We believe that this offset may be due to a possible misalignment between the current and optical apertures of the VCSEL.

In another set of experiments, the thermal coupling in the VCSEL array was measured using the traditional wavelength shift technique. Similar to the single VCSELs, the shift in the lasing wavelength measured a greater change in

temperature than the thermoreflectance technique. The impedance between the surface and the cavity may explain the measured temperature discrepancy between the two techniques. A thermal conductivity σ of 0.41 W/(cmK) was calculated for the VCSEL array and matches well with the known value of the thermal conductivity of gallium arsenide ($\sigma = 0.45$ W/(cmK)).

Lastly, a time gated experiment was performed to better understand how fast the temperature from the modulated VCSEL spreads out across the surface of the array. To do this, we experimentally determined a value for the thermal diffusivity α of the VCSEL array equal to $1.47 \times 10^{-5} \text{ m}^2\text{s}^{-1}$. This value is consistent with known values for the thermal diffusivity of bulk GaAs ($\alpha = 3.1 \times 10^{-5} \text{ m}^2\text{s}^{-1}$) and thin film GaAs ($\alpha = 2.3 \times 10^{-5} \text{ m}^2\text{s}^{-1}$). Using our novel time gated technique we are able to measure the thermal diffusivity of a complex VCSEL structure.

Overall, several temperature measurement techniques, including high resolution thermoreflectance microscopy, were performed to investigate the thermal characteristics of operating vertical cavity surface emitting lasers. Thermoreflectance microscopy provides several advantages over traditional techniques including two dimensional imaging of thermal distribution with greatly improved spatial resolution, which allow us to further explore many of the thermal effects in these small lasers and laser arrays. The results presented in this thesis lead to a better understanding of the thermal behavior of operating VCSELs, including effects such as thermal lensing and coupling as well as

improved understanding of the role various VCSEL design parameters play in their thermal behavior.

REFERENCES

- [1] G. Chen, "A Comparative Study on the Thermal Characteristics of Vertical-Cavity Surface-Emitting Lasers." *Journal of Applied Physics*. Vol.77 (9), pp. 4251-4258, 1995.
- [2] K. Luo, R.W. Herrick, A. Majumdar, P. Petroff, "Scanning Thermal Microscopy of a Vertical-Cavity Surface-Emitting Laser." *Applied Physics Letters*. Vol. 71 (12), pp. 1604-1606, 1997.
- [3] S. M. Zakharov and Eduard A. Manykin, "Thermal Cross-talk Analysis of Vertical-Cavity Surface-Emitting Laser Arrays." *Proc. SPIE 4750*, 238, 2002.
- [4] T. Wipiejewski, J. Ko, B. J. Thibeault, D. B. Young, L. A. Coldren, "2D Vertical-Cavity Laser Arrays for Free-Space and Multimode Fiber Transmission Systems." *Electronic Components and Technology Conference Proceedings*. pp.1130-1135, 1996.
- [5] M. Dabbicco, V. Spagnolo, M. Ferrara, G. Scamarcio, "Experimental Determination of the Temperature Distribution in Trench-Confined Oxide Vertical-Cavity Surface-Emitting Lasers." *IEEE Journal of Quantum Electronics*, Vol. 39 (6), pp. 701-707, June 2003.
- [6] M. Dabbicco, V. Spagnolo, M. Ferrara, G. Scamarcio, "Non-Destructive Technique for the Direct Measurement of the Local Temperature Distribution in VCSELs." *Proc. SPIE 4648*, 22-29 (2002).
- [7] K. D. Choquette, D. A. Richie, and R. E. Leibenguth, "Temperature Dependence of Gain-Guided VCSEL Polarization." *Applied Physics Letters*, Vol. 64, pp. 2062-2064, April 1994.
- [8] C. Degan, I. Fischer, and W. Elsäßer, "Thermally Induced Local Gain Suppression in VCSELs." *Applied Physics Letters*, Vol. 76, pp. 3352-3354, June 2000.
- [9] M. Brunner, K. Gulden, R. Hovel, M. Moser, and M. Ilegems, "Thermal Lensing Effects in Small Oxide Confined Vertical-Cavity Surface-Emitting Lasers." *Applied Physics Letters*, Vol. 76, pp. 7-9, 2000.
- [10] M. Osinski and W. Nakwaski, "Thermal Effects in Vertical Cavity Surface Emitting Lasers." *International Journal of High Speed Electronics and Systems*, Vol. 5, (4), pp. 667-730, 1994.

- [11] R. Amatya, "Thermal Measurements of Vertical Cavity Surface Emitting Lasers and Other Optoelectronic Devices." Thesis, Smith College, 2005.
- [12] T. Wipiejewski, D. B. Young, B. J. Thibeault, and L. A. Coldren, "Thermal Crosstalk in 4 x 4 Vertical-Cavity Surface-Emitting Laser Arrays." *IEEE Photonics Technology Letters*, Vol. 8 (8), pp. 980-982, 1996.
- [13] Y. Uchiyama, T. Kondo, K. Takeda, A. Matsutani, T. Uchida, T. Miyamoto, and F. Koyama, "Thermal Cross-Talk Evaluation of Density Integrated Vertical Cavity Surface Emitting Laser Array." *IEICE Electronics Express*, Vol. 1 (17), pp. 545-550, 2004.
- [14] M. Farzaneh, R. Amatya, D. Luerszen, K.J. Greenberg, W.E. Rockwell, J.A. Hudgings, "Temperature profiling of VCSELs by Thermoreflectance Microscopy." *IEEE Photonics Technology Letters*, Vol. 1, pp. 601-603, April 2007.
- [15] Sale, T. E. Vertical Cavity Surface Emitting Lasers. Taunton: Research Studies Press Ltd., 1995.
- [16] C.S. Wang, R. Koda, A.S. Huntington, A.C. Gossard, and L.A. Coldren, ">100% Output Differential Efficiency 1.55 μ m VCSELs Using Submonolayer Superlattices Digital-Alloy Multiple-Active-Regions Grown by MBE on InP." *Journal of Crystal Growth*, Vol. 277, pp. 13-20, 2005.
- [17] "Reliability Data: 850nm Proton VCSEL Reliability Study." Finisar: Global Technology Leader of Fiber and Optic Subsystems and Network Test Systems. 2009. Finisar Corporation. 15 Jan. 2009 <http://www.finisar.com/library1_21_4>.
- [18] Optical Society of America. Handbook of Optics: Fiber Optics and Nonlinear Optics. 2nd ed. Volume IV. Blacklick, OH: McGraw-Hill Professional, 2000. 147.
- [19] Saleh, Bahaa E. A., Malvin Carl Teich. Fundamentals of Photonics. New York: John Wiley & Sons Inc., 1991. 551-552.
- [20] Yu, Siu Fung. Analysis and Design of Vertical Cavity Surface Emitting Lasers. Hoboken, NJ: John Wiley & Sons Inc., 2003.
- [21] P.M. Mayer, D. Luerben, R.J. Ram, and J.A. Hudgings, "Theoretical and Experimental Investigation of the Thermal Resolution and Dynamic Range of CCD-Based Thermoreflectance Imaging." *Journal of the Optical Society of America*, Vol. 24, pp. 1156-1163, 2007.
- [22] S. Dilhaire, S. Grauby, and W. Claeys, "Thermoreflectance Calibration Procedure on a Laser Diode: Application to Catastrophic Optical Facet

Damage Analysis,” *IEEE Electronic Devices Letters*, Vol. 26 (7) pp. 461-463, 2005.

- [23] K. J. Greenberg, J. A. Summers, M. Farzaneh, and J. A. Hudgings, “Spatially-Resolved Thermal Coupling in VCSEL Arrays Using Thermoreflectance Microscopy,” *CLEO Conference*, 2008.
- [24] Svelto, Orazio, *Principles of Lasers*. 4th ed. New York: Plenum Press, 1998.
- [25] J. M. Catchmark, *et al.*, “Extended Temperature and Wavelength Performance of Vertical Cavity Top Surface Emitting Lasers,” *Applied Physics Letters*, Vol. 63, pp. 3122-3124, Dec. 1993.
- [26] T. Yao, “Thermal Properties of AlAs/GaAs Superlattices,” *Applied Physics Letters*, Vol. 51, pp. 1798-1800, 1987.
- [27] S. Aloulou, M. Fathallah, M. Oueslati, and A. Sfaxi, “Determination of Absorption Coefficients and Thermal Diffusivity of Modulated Doped GaAlAs/GaAs Heterostructure by Photothermal Deflection Spectroscopy,” *American Journal of the Applied Sciences*, Vol. 2 (10), pp. 1412-1417 2005.
- [28] G. Chen, C. L. Tien, X. Wu, and J. S. Smith, “Thermal Diffusivity Measurement of GaAs/AlGaAs Thin-Film Structure,” *Journal of Heat Transfer*, Vol. 116, pp. 325-331, 1994.